Synthesis and Selective Patterning of Large Area Graphene-Oxide by Langmuir-Blodgett Technique for Bio-Nano Electronics Applications

Neha Chauhan

4R10111001

Doctor Course

Bio-Nano Science Fusion Course

Graduate School of Interdisciplinary New Science

Toyo University, Japan

July 2014

Dedicated
to
My Parents, Teachers and
Friends

Creative Bonds that can be Patterned...

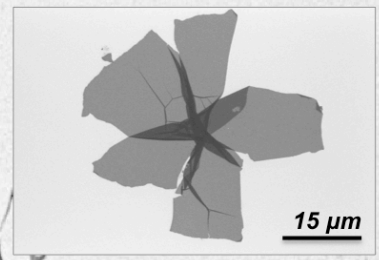

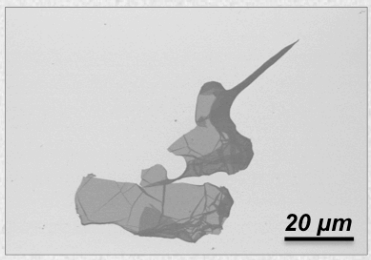

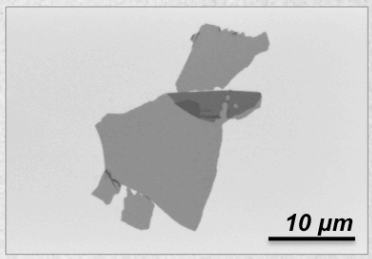

Preface

An important aspect of nanotechnology is the formation of monolayer patterned thin films of nanomaterials that can be realized either by assembling the nanoparticles or synthesizing them in 2D confined space. Graphene, a monolayer of sp^2-bonded carbon atoms arranged in a honeycomb crystal lattice is a basic building block for all graphitic materials. It has stimulated extensive interest in both academia and industry owing to its unique fascinating electrical, mechanical, optical and biocompatible features. Currently, graphene-based Bio-Nano Electronics applications, in particular, are the subject of intense research worldwide. Assembly of GO via the LB technique has proven to be a straightforward and highly reproducible method for the production of uniform 2D film at the air-water interface for a variety of applications. It is also recognized that the size of GO plays an important role for modulating its electronic and chemical properties that makes it an ideal building block for the next generation micro as well as nanoscale electronics devices. A significant progress has been made in the area of its synthesis and applications. However, from an industrial point of view, a major challenge still exists to synthesize it as a large area monolayer, its self-assembly, selective placement and patterning for application in areas such as electronics, photonics, optoelectronic devices, biological and chemical sensing, energy conversation etc.

Progress in this direction has been made by many researchers using various techniques including electron beam lithography (EBL), photolithography (UVL), scanning probe lithography (SPL), block copolymer lithography, soft transfer printing, masked laser patterning, direct laser patterning, combination of wettability modulation and spin coating, ink-jet printing, etc. The complex patterned structures can be formed using the current lithography and metal evaporation deposition techniques. However, this technique involves photoresists, which are undesirable due to the presence of residual polymers that may contaminate the graphene surface and interfere with subsequent metallization steps. Apart from that, these processes are time consuming, involve highly expensive, sophisticated instruments and suffer from low throughput. However, surprisingly the use of air-water interface for selective placement and patterning of large area 2D graphene and related derivatives with controllable dimensions

remains largely unexplored.

An important aspect of this work is that a new protocol has been developed for the selective placement of GO over large area, which involve monolayer assembly through partial hydrophilization of SiO_2/Si substrate by N_2-plasma via LB technique. This protocol is different from existing methodologies in a way that it involves one-step selective placement and pattering of monolayer GO with controlled dimensions that doesn't need any special equipment and has high throughput with a short fabrication time.

The work presented in this thesis comprises of *eight chapters,* which deals with potential applications of large area patterned GO monolayer film for Bio-Nano Electronics applications. An ecofriendly approach has been adopted for the reduction of GO for green electronics and bioscience applications. Thereafter, large area GO was synthesized to fabricate patterned monolayer films using the LB technique. The effect of N_2-plasma treatment was harnessed to partially hydrophilize SiO_2/Si for the pattern formation. Various parameters have been optimized to create closely packed GO films without using any surfactant at the air-water interface. The mechanism behind film formation only at the specified area has been studied using various characterization techniques. Finally, this protocol has been utilized to selectively place GO between the electrodes for device fabrication and to enhance cellular growth at a particular area for Bio-Nano applications.

Chapter 1 is an introduction to this thesis and gives an overview of the fascinating features of graphene and GO, its synthesis and 2D ordered assembly using various strategies. It also discusses the theoretical understanding and processing routes available for patterning GO and highlights its potential applications. Finally, it concludes with the motivation behind this thesis.

Chapter 2 elucidates the physical principles of different instrumentation and characterization techniques that are extensively adapted for the interpretation of this work. It includes Langmuir-Blodgett (LB) Technique, UV-vis Spectroscopy, Fourier Transform Infrared Spectroscopy (FTIR), Raman Spectroscopy, Zeta Potential Measurement, Optical Microscopy, Scanning Electron Microscopy (SEM), Atomic Force Microscopy (AFM), Transmission Electron Microscopy (TEM), X-ray

Photoelectron Spectroscopy (XPS), Plasma System, Optical Emission Spectroscopy (OES), Contact Angle Measurements, Electron Beam Lithography (EBL), Photolithography (UVL), Electron Beam Evaporator System, Thermal Resistive Evaporator System, and Electrical Conductivity Measurement.

Chapter 3 discusses a facile ecofriendly route for the green reduction of GO. Halophilic bacteria (*Halomonas* species), salt loving extremophiles that can withstand harsh environmental conditions, were demonstrated to be an appropriate candidate to effectively replace the utilization of various toxic chemicals and organic compounds to reduce GO. Aerobic and anaerobic mode of GO reduction was demonstrated using bacterial culturing and the graphene obtained was evaluated for its conductivity and biocompatibility. Bacterially reduced GO (BRGO) was found to be highly conductive and supports mammalian cell growth under *in vitro* conditions. Electrical measurements by 3-probe method revealed that the conductivity increased by 10^4-10^5 fold from GO to BRGO. Biocompatibility assay using mouse fibroblast cell line showed that BRGO is non-cytotoxic and has a tendency to support as well as enhance cell growth under laboratory conditions. GO reduction with large area and high conductivity would greatly contribute to the biomedical and electronic applications of graphene.

Chapter 4 focuses on the synthesis of large area monolayer GO in aqueous medium, its assembly at air-water interface and LB film formation. Large area monolayer GO was made using modified Hummer's method with minor modification. Several parameters like GO solution concentration, volume and LB parameters were optimized to assemble monolayer GO at the air-water interface, leading to closely packed 2D atomic assembly that could considerably simplify the patterning process. Various characterization techniques have been performed to elucidate the effectiveness of the assembled monolayer GO sheets.

Chapter 5 deals with the influence of different plasma systems on SiO_2/Si for its specific area hydrophilization under various chamber pressure conditions. It is worthwhile to note that the gas selection and substrate type determines the functional groups that will be formed on the plasma-exposed substrate. Thus, a comparative study has been performed between air and N_2 -plasma systems to elucidate the effectiveness of specific area monolayer GO deposition via LB

technique. This study reveals that the hydrophilization and surface modification process occurs when SiO_2/Si surface was treated with air or N_2-plasma. The N_2-plasma was found to be more efficient for the specific placement of GO and to promote its adhesion to the substrate. It is well known that the surface modification is often sensitive to time and environmental exposures, thus aging study was also carried out to preserve the plasma-induced physical and chemical properties of the substrate prior to GO deposition.

Chapter 6 describes one-step facile technique using N_2-plasma that stimulates surface modification and enhances surface wettability of the substrate. This technique was employed to create partially hydrophilic surface with the aid of various templates, which enables selective deposition, alignment and formation of desired monolayer GO-sheets patterns via LB deposition technique over large area without the need of any sophisticated equipment. Various characterization techniques were carried out in order to understand the mechanism behind it. It is relatively an easy and swift process that can accomplish reliable specific surface modification with high bonding strength between GO and the substrate. This technique will allow us to create patterns with controlled dimensions including the thickness of GO-sheets, which is one of the important factors in creating arrays and devices at wafer-scale. Being simple yet effective and inexpensive, this technique holds tremendous potential that can be exploited for various fascinating applications in the field of Bio-Nano-Electronics.

Chapter 7 describes how specific area placement and patterning of GO via N_2-plasma-assisted surface modification of SiO_2/Si can contribute towards applications in electronics and bioengineering field. Cytotoxicity assay reveals that the as-synthesized large area monolayer GO sheets are non-toxic to L929 and HCN cells and are highly biocompatible. A proof of concept experiment was performed in which a patterned GO substrate was used for specific area cellular growth of L929 cells. Moreover, a straightforward way to make graphene-based device using UVL and electron beam evaporation technique has been followed to define Au/Ti electrodes for the electrical contacts. The plasma enhanced surface modification of SiO_2/Si approach was adapted to selectively place GO on the pre-patterned electrodes via LB technique. The results reveal a successful specific area cellular growth on the patterned substrate and placement of GO on the pre-

fabricated electrodes. This facile and quick approach can precisely assemble GO sheets directly from dispersion to the desired area, thus significantly reducing the processing steps required for device fabrication and cell patterning.

Chapter 8 synopsizes the work presented in this thesis and emphasizes on the future prospects of this work in field of material science.

Contents

Chapter 1: Introduction

Chapter 2: Instrumentation and Characterization Techniques

1

Introduction

"Necessity is the mother of all inventions"
- anonymous

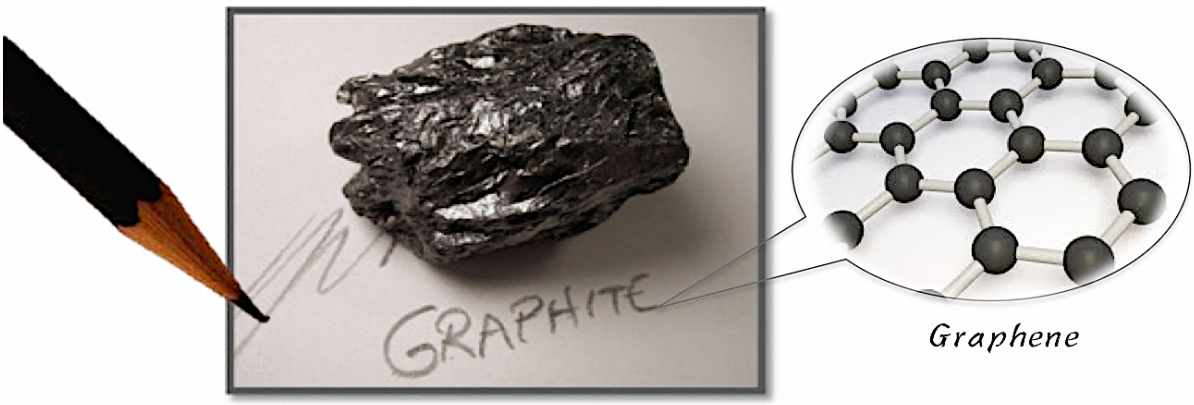

Size Matters! Thickness Matters too..!

This chapter provides an introduction to the thesis with a brief review of graphene and graphene oxide (GO) regarding its unique features, synthesis, assembly and applications for various Bio-Nano Electronics applications. It also discusses present strategies used to pattern GO for creating arrays and devices. Finally, it concludes with the motivation behind this thesis.

As rightly quoted, "*Necessity is the mother of invention*", a large number of inventions and discoveries owe their successful existence to necessity. Unless there is a need we are not sufficiently motivated to attain the goal. People have been passionate enough to explore science and transform it into an effective technology, not only to boost the competitiveness in our industry but also to create new products that fulfill their needs. Nanotechnology is one such innovation that has opened up new avenues of research, which has led to many useful and serendipitous applications. Let's have a glimpse of what Nanotechnology is…

1.1 Nanoscience

The Next 'Big Thing' is very very very Small…! 10^{-9}

The term "*Nano*" has originated from a Greek prefix, meaning *dwarf*. *Nanoscale* is the imaginative world of '*the small'*, where one nanometer refers to one billionth of a meter, or 1/20000 times the smallest cell -a naked eye can see. So now the obvious question is up to what length scale shall we speak of nanometer, 10 nm, 100 nm or 1000 nm? The answer to this is very debatable, but most scientists believe that the nanoscale objects should have at least one dimension that is less than 100 nm and that is where the physical, chemical, optical and electrical properties changes drastically as compared to the bulk regime.

Nanotechnology, the art of building machines one atom at a time was first conceptualized by Nobel laureate physicist *Richard Feynman* in 1959, when he described the future in a ground breaking talk about the physical possibilities for "making, manipulating, visualizing and controlling things on a small scale," and imagining that in decades to come, it might be possible to assemble atoms "the way we want". He was the one to suggest that the laws of physics would allow people to make much smaller machines eventually reaching the atomic level [1].

Size-dependent properties are the reason that nanoscale materials have the potential to significantly impact both science and industry. **Examples of size dependent properties include:**

- *Catalytic Properties* – how the material enhances chemical reactions.
- *Electrochemical Properties* – how the material transfers electrons to other chemical constituents.

- *Melting Properties* – how the material transit from solid to liquid.
- *Magnetic Properties* – how the electrons interact to induce magnetic poles.
- *Optical Properties* – how the material interacts with light (e.g., its color).

Reduction in size of a material leads to the change in properties such as colour, electrical conductivity, mechanical strength and melting point, those that are considered intensive in nature [2]. The concept of making materials to nanometre size is fundamentally interesting for the following reason:

As the size approaches atomic dimensions, energy level bands gradually transform into quantized discrete energy levels. Since the changes in the electronic structure occur on the nanometre scale, it gives us an insight as to how the properties evolve from the molecular or atomic level to the bulk. Also the reduction in size would confine the electronic motion, which will affect the physical and chemical properties of the material. Besides that, decreasing the particle size increases surface area and thus provides more reactive sites for the same volume (**Figure 1**).

With material properties being characterized by the length scale of a material, fabricating materials with at least one dimension on the nanometre scale confines the electronic wavefunction in that dimension. Consequently, the confinement of electronic wavefunction becomes a function of the size and shape of the material. Hence, any variation in size and shape of the material may manifest itself as a property change.

1. Small Size Effect

- Contains very small number of particles.
- Electronic states are quite different from those of bulky particles.

2. Large Surface Effect

- Contain large portion of surface particles.
- High surface activity.

3. Change the Dimensional Properties

- 3D → 2D

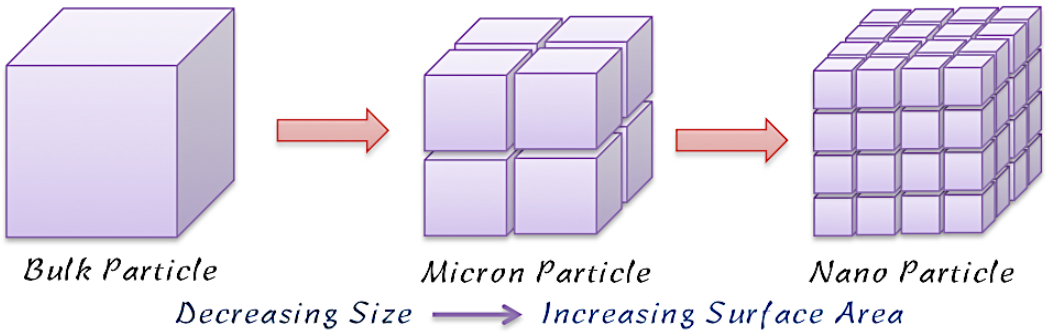

Figure 1. Increase in surface area with size reduction.

Top-down and Bottom-up are the two approaches that have been used for the synthesis of nanomaterials [3].

Top-down approach involves mainly physical methods where a bulk material is sliced into pieces till the desired size is achieved **(Figure 2(a))**. Lithography technique, laser induced chemical etching and ball milling fall into this category. However, these methods are effective only down to the micrometre level and reaching nanometre scale makes these methods more expensive and technically difficult.

Bottom-up or self-assembly, approaches mainly involve chemical and biological methods to make nanostructures and nanoparticles **(Figure 2(b))**. The smaller components of atomic or molecular dimensions self-assemble together, according to a natural physical principle or an externally applied driving force, to give rise to larger and more organized systems. This comprises controlled condensation of solute molecules that are formed during a chemical reaction. The restriction of the condensation or the growth leads to the formation of desired

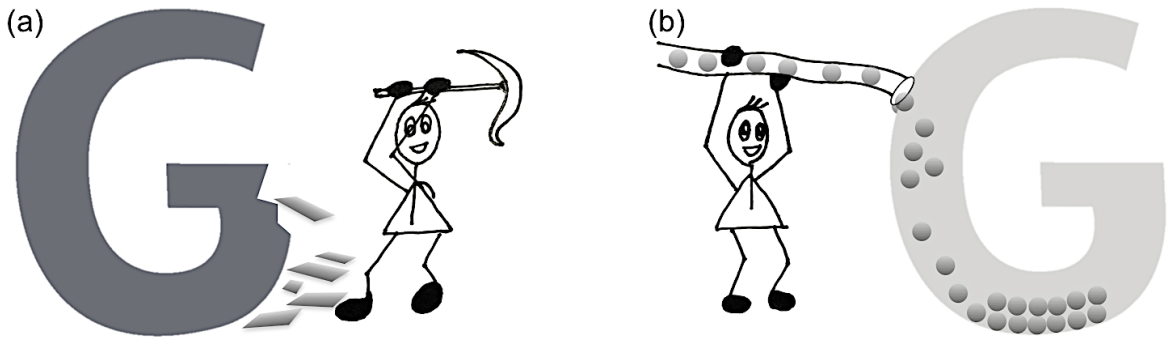

Figure 2. **(a)** Top to Down Approach: Start with the Bulk Material & "cut away material" to make what we want, **(b)** Bottom to Up Approach: Building what we want by assembling it from building blocks (such as atoms & molecules). Atom-by-atom, molecule-by-molecule, or cluster-by-cluster.

size and shape [4, 5]. However, unlike the chemical synthesis of molecules of a desired structure the synthesis of nanomaterials with uniform size and shape is difficult. Thus, the large-scale synthesis of nanomaterials remains a challenge.

While the perceived applications of nanomaterials based on their electrical, optical and magnetic properties are too many to list here, for many of them the physico-chemical environment that they are prepared/present in becomes very crucial. For biological related applications, it is imperative that the nanomaterials are present in aqueous environment while those looking for electronic applications prefer to have nanoparticles dispersed in water or organic solvents.

Classification of Nanomaterials

Nanomaterials can be classified at as 0D, 1D, 2D, or 3D materials based on the scheme proposed Pokropivny and Skorokhod [6, 7]. They can exist in single, fused, aggregated or agglomerated forms with spherical, tubular, and irregular shapes. Common types of nanomaterials include nanotubes, dendrimers, quantum dots and fullerenes. Nanomaterials have applications in the field of nano technology, and exhibits different physical-chemical characteristics from normal chemicals (i.e., silver nano, CNT, fullerene, photocatalyst, carbon nano, silica). They can be created with various modulation dimensionalities as defined by: 0D (such as uniform particles arrays like quantum dots, heterogeneous particle arrays, core-shell quantum dots, onions, hollow spheres and nanolenses), 1D (nanowires, nanorods, CNTs, nanobelts, nanoribbons, and hierarchical nanostructures), 2D (junctions (continuous islands), branched structures, nanoprisms, nanoplates, nanosheets (graphene), nanowalls, and nanodisks), and 3D (nanoballs (dendritic structures), nanocoils, nanocones, nanopillers and nanoflowers) as shown in **Figure 3.**

It is difficult to predict at what size a particular material will transition from having bulk properties to size-dependent properties. This threshold is different for each material and each property. For example, graphene, a single layer of carbon atoms, arranged hexagonally, in a chicken wire structure has unique properties. However, many layers of it make up the much more familiar graphite – *Pencil Lead*. So, why is a pencil not worth thousands of yens? Why is graphene so startlingly different from graphite? What does a 2D thing actually imply? Is it like to have a sheet of atoms we can hold in our hands?

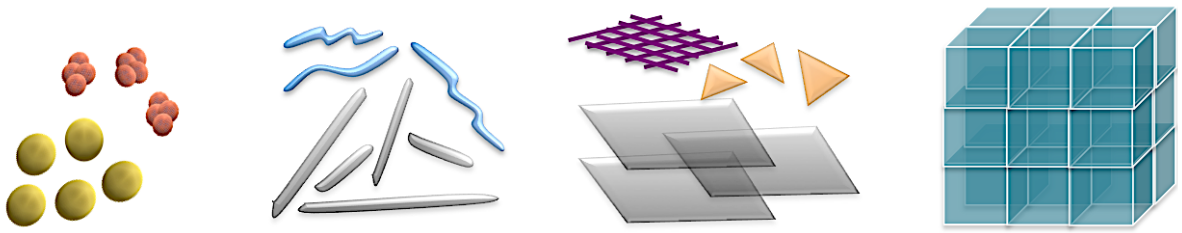

Figure 3. Classification of Nanomaterials (a) 0D Spheres and Clusters, (b) 1D Nanofibers, Wires, Rods and Carbon Nanotubes, (c) 2D films, plates and graphene (d) 3D nanomaterials.

In graphite, the electrons associated with the carbon atoms interact with each other between the layers to stick the sheets together in a mass. Without these interactions, such as in graphene, the electrons would behave rather differently as though they are massless particles, moving freely through empty space around them, at close to the speed of light. At this point, things start to get interesting with some amazing properties: it is really very hard to pick one feature when the material is so astonishing. So let's consider them in more detail in the upcoming section.

1.2 What is Graphene?

Graphene is the 2D lattice of carbon atoms having one atom thick layer. A millimeter sized graphite flake contains a stack of three million layers of graphene held weakly together.

Andre Geim and Konstantin Novoselov are the two scientists from *University of Manchester* who won the Novel Prize in Physics in *2010* "*for their groundbreaking experiments regarding the 2D material graphene in 2004"* [8]. The exceptional physical properties including immense strength, excellent thermal and electrical conductivity, along with transparency and flexibility of the sheet, has inspired many of the envisaged future applications such as roll-up and wearable electronics, in addition to the plethora of other real-world applications where graphene may find a use, such as in many Bio-Nano Electronics related applications.

It has many dimensions including 3D in graphite crystal, 2D in a single layer, 1D in nanotubes and 0D in fullerenes (**Figure 4**) [9].

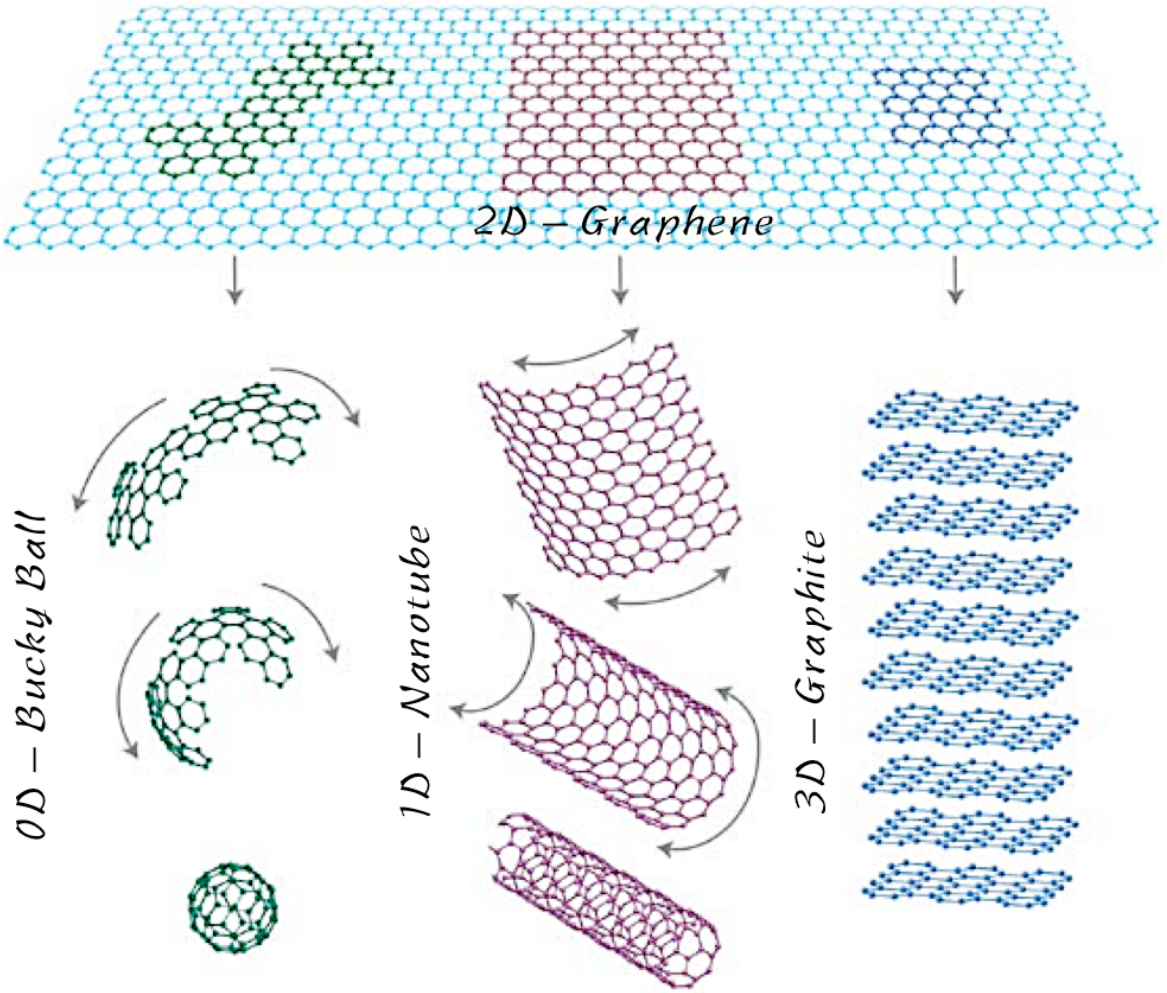

Figure 4. Graphene can be envisaged as a 2D material for carbon materials among all other dimensionalities (*Reproduced by permission of Nature Publishing Group, Ref. 9).*

Structure of Graphene

The term 'graphene' refers to a single layer of graphite with sp^2 hybridized carbon atoms arranged in a hexagonal lattice and partially filled π-orbitals above and below the plane of the sheet with high surface to volume ratio. The edges of graphene can be described as having armchair or zigzag motifs (**Figure 5)** with the two edge types leading to different electronic and magnetic properties [10].

The study of the electronic band structure of graphene requires the understanding of its crystal lattice structure. Each carbon atom with its one s and two in-plane p orbitals forms a strong sp^2 covalent bond with three neighboring carbon atoms providing strength to the graphene honeycomb structure. The electron in the z-direction of the p-orbital remains unpaired and is responsible for the high charge carrier conduction of graphene. The three in-plane σ-orbitals

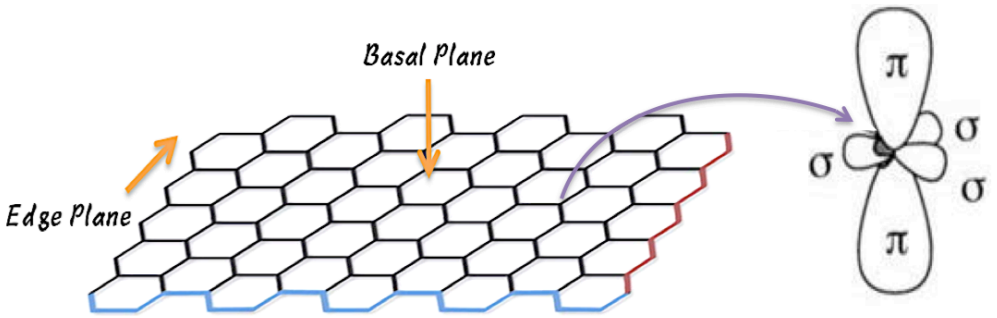

Figure 5. Armchair (blue) and zigzag (red) edges in monolayer graphene.

and one out of plane (perpendicular to graphene sheet) π-orbital formed by P_z electrons of carbon atoms are shown in **Figure 5**.

1.3 Why Graphene?

What is so special about graphene that makes this material so remarkable? Here are few strangest facts about graphene [8, 9]

1. Strength

"The most amazing thing about graphene is its strength. It is the strongest material ever measured, with its freestanding monolayer exhibiting salient non-linear elastic behavior and a Young's Modulus of ~ 1.0 TPa [11-13]. The intrinsic strength of a defect-free graphene nanosheet corresponds to 130 GPa at a strain of 0.25. This strength is 200 times greater than that of steel and higher than the fracture strengths of many conventional materials [11].

2. No Band Gap

The most intriguing features of graphene are its exceptional electronic quality and the transport properties of individual graphene crystallites. Due to its 2D nature, graphene is theoretically a zero-bandgap semiconductor with excellent room temperature electrical conductivity [14,15].

Graphene has a remarkable band structure thanks to its crystal structure. Carbon atoms form a hexagonal lattice on a 2D plane. Each carbon atom is about a = 1.42 Å from its three neighbors, with each of which it shares one σ-bond. The fourth bond is a π-bond, which is oriented in the z-direction (out of the plane). One can visualize the π-orbital as a pair of symmetric lobes oriented along the z-axis and centered on the nucleus. Each atom has one of these π-bonds, which

are then hybridized together to form what are referred to as the π-band and π^*-bands. These bands are responsible for most of the peculiar electronic properties of graphene.

The hexagonal lattice of graphene can be regarded as two interleaving triangular lattices, which is illustrated in **Figure 6 (a).** This perspective was successfully used as far back as 1947 when Wallace calculated the band structure for a single graphite layer using a tight-binding approximation [15].

Many (but not all) of the extraordinary features of graphene derive from the combination of its dimensionality and its very peculiar electronic band structure where the electrons mimic relativistic particles [9]. This is why electrons in graphene are usually called massless Dirac Fermions [16] and can be seen as electrons that have lost their rest mass (of course, the electrons as fundamental particles preserve their characteristic mass). This curious behavior of the electrons makes graphene ideally suitable for studying relativistic effects in condensed matter experiments. To date, the most remarkable consequences of this behavior are the appearance of an a typical quantum Hall effect [16, 17], first observations of Klein paradox [18, 19] and the study of relativistic phenomena as the Zitterbewegung, or jittery motion of the wave function in the presence of confining potentials. This peculiar band structure is modified to a more common one when more than three layers of graphene are stacked.

In addition, the valence and conduction band in graphene touch each other at a single point [20] (**Figure. 6**), offering very few electronic states near the Fermi level. For this reason graphene is usually called a semimetal or a zero gap semiconductor. The fragility of a single point contact makes the band structure of graphene highly sensitive to any change, such as external electric fields, mechanical deformations, doping and adsorbates, which is very desirable for sensing applications. This also confers an ambipolar character onto graphene, i.e. charge carrier can be either holes or electrons depending on doping [8]. However, chemical doping is not always needed to change the charge carrier sign (it can be changed by local electric fields). This property opens the door to electrical engineering by creating p-n junctions with high mobility, the basis of current CMOS technology. Microscopic studies have proved that graphene also exhibits outstanding crystal quality on scales as large as a few microns [21]. The absence of defects or imperfections makes electrons free to travel distances as long as a few micrometers without scattering, even in samples placed on rough substrates. The

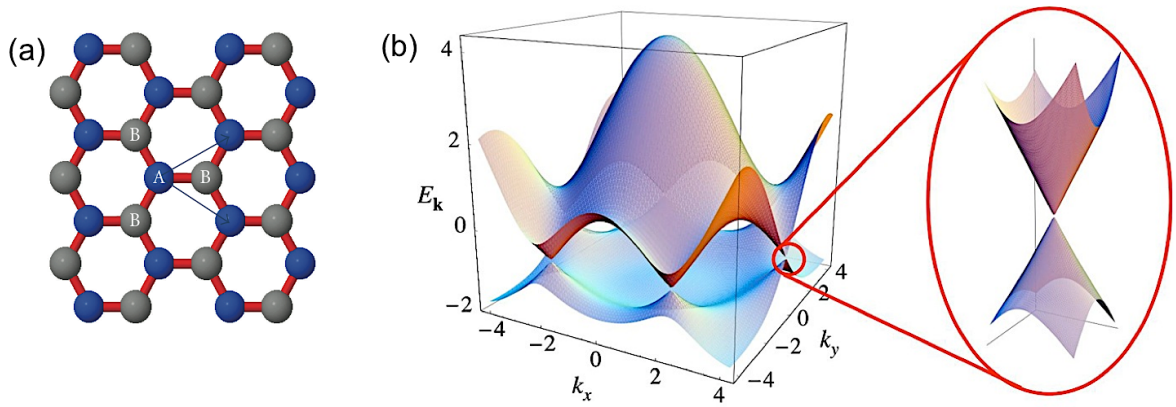

Figure 6. (a) Triangular sublattices of graphene. Each atom in one sublattice has 3 neighbors in sublattice (B) and vice-versa (*Reproduced by the permission of International Scholarly Research Notices, Ref 15(b)),* **(b)** Electronic dispersion of graphene. The conduction band and the valence band touch each other at six discrete points. These points are called *K* points. The six points can be divided into two in-equivalent sets of three points each. The points within each set are all equivalent because they can reach each other by reciprocal lattice vectors. The two in-equivalent points are called *K* and *K'* and form the valley isospin degree of freedom in graphene. The name valley isospin stems from the similarity of the vicinity of these points with a valley. The zoom shows that the dispersion relation close to the *K* points looks like the energy spectrum of massless Dirac particles (*Reproduced by the permission of American Physical Society, Ref. 15(c)).*

lack of scattering results in high mobility [22] of the charge carriers and gives access to the observation of quantum phenomena, such as the quantum Hall effect, even at room temperature [23]. In addition, high mobility observed in graphene (about 1000 times higher than silicon) is important for making electronic circuits that have fast switching rates.

The absence of a band gap makes the absorption of light in a large range of the electromagnetic spectrum possible, spanning from the infrared to the ultraviolet [24], and giving rise to a vast number of possibilities of electronic transition which open a huge potential both for applications in electronic-photonic devices and fundamental studies [25].

This makes graphene a wonderful candidate for use in photovoltaic (PV) cells, for instance, because it can absorb photons with energy at every frequency — photons of different frequencies of light are converted to electrons with matching

energy levels. A material with a band gap can't convert wavelengths of light that correspond to the forbidden energy states of the electrons. *No band gap* means everything is accepted.

This opens up the tantalizing possibility of highly efficient PV cells, but it's a problem if we want to use graphene in transistors, where we need the band gap to provide the isolation necessary if we want it to act it as a switch that can be turned off.

It is possible to induce a small band gap in graphene by doping it. This is good enough for very fast amplifiers for radio work, but for transistors that make efficient logic circuitry we need a bigger gap.

Electrical Conductivity.

For metals, conductivity is based on their band structure. If the conduction band is only partially occupied by electrons, electrons can move in all directions without resistance (provided there is a perfect metallic crystal lattice). They are not scattered by the regular building blocks, due to the wave character of the electrons.

$$\mu = \frac{e\lambda}{4\pi\varepsilon_o m_e v}$$

where λ is the mean free path of the electron two successive collision, m_e being effective mass of electron in the lattice, v the speed of electron (Fermi speed), ε_0 is the dielectric constant of the medium, τ the mean time between collisions which is λ/v

- For Cu, v = 1.6 x 10^6 m/s at room temp.; λ = 43 nm, τ = 2.7 x 10^{-14} s

Scattering Mechanisms.

(1) By *lattice defects* (foreign atoms, vacancies, interstitial positions, grain boundaries, dislocations, stacking disorders). It is more or less independent of temperature while

(2) *Scattering* at thermal vibration of the lattice (phonons) is independent of lattice defects, but dependent on temperature.

- The collective motion of electrons in the bulk phase obeys Ohm's law (V = IR). However, when the size of the metal approaches the nanometer scale, band structure begins to change and discrete energy levels begin to dominate that

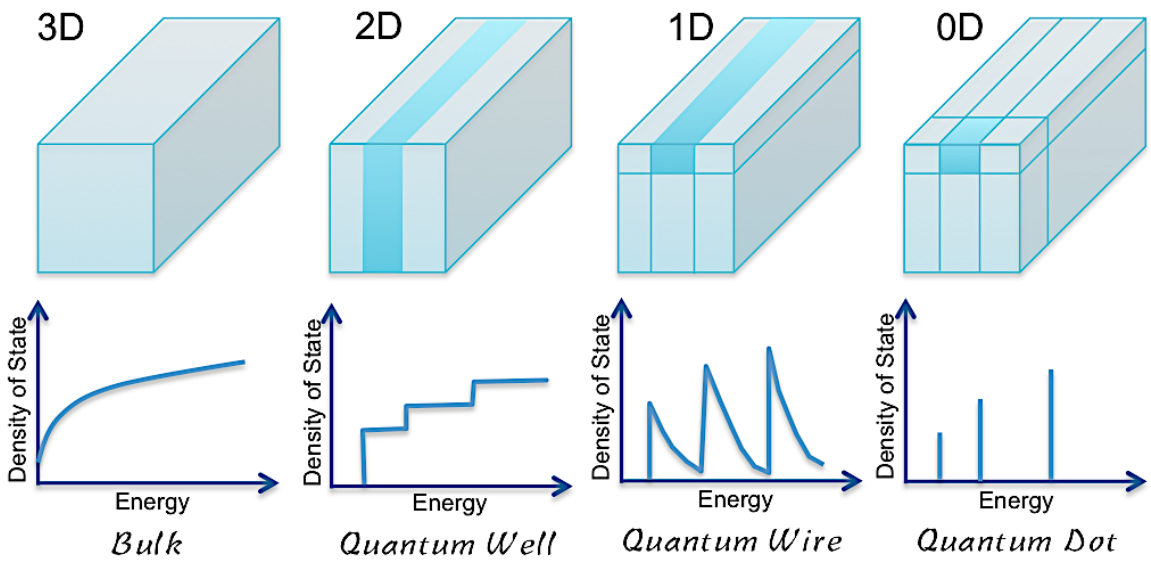

leads to unique electronic properties and ohm's law is no longer obeyed.

- If a bulk metal is made thinner and thinner, until the electrons can move only in 2D (instead of 3), then it is "2D quantum confinement."
- Next level is 'quantum wire'
- Ultimately 'quantum dot'

In general, it can be concluded that the electrical conduction within the 3D nanoparticle assemblies depends on the particles size, the interparticle spacing as well as the nature of the capping agent and its electronic structure.

3. Ballistic Conduction

The hexagonal lattice has the longest "*mean free path*" of any known material — on the order of microns. This is the distance an electron can travel freely without bumping into anything, or having its path disrupted by scattering: the things that induce resistance. When the mean free path is longer than the dimensions of the material, we get ballistic transport (in term of high mobility of the charge carriers).

In graphene, the mean free path is of the order of 65 microns — long enough that electronic components could be made that would operate at ambient temperatures with virtually no resistance. This is similar to superconductivity, but at room temperature.

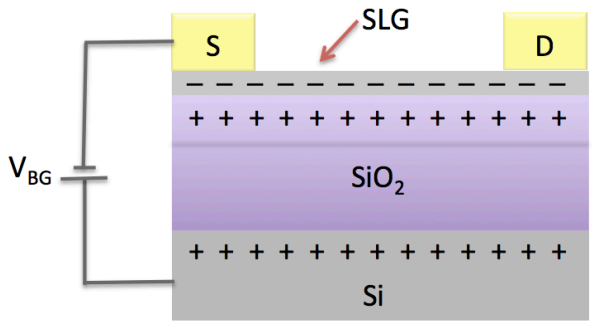

Figure 7. Schematic of a SiO_2 back-gating. Courtesy: *Graphene and Its Fascinating Attributes*, eds. S. Pati, T. Enoki and C. N. R. Rao.

Probing Single and Bilayer Graphene Field Effect Transistors (FETs).

It has been shown experimentally by Novoselov et al. [26] that in single layer graphene (SLG) back gated FET, conductivity of the graphene increases linearly with gate voltage (V_G) except very close to the neutrality point (Dirac point (V_D)). It was seen that conductivity does not disappear in the limit of vanishing carrier concentration (n) but instead exhibits a minimum conductivity whose value varies from sample to sample. Another observation is that near the Dirac Point, conductivity does not increase sharply and indeed it remains constant for a range of gate voltages, $V_D \pm \Delta V_G$ (**Figure 7**). It is known that due to pseudospin conservation there are no intra-valley and inter-valley back scattering [27]. As a result, the current flow in graphene is expected to be ballistic.

Since the length of the samples in most of the experiments is more than few microns (5-10 μm), much larger than the ballistic transport length (~100 nm) at room temperature, diffusive transport [9, 28, 29] is sufficient to explain most of the conductivity results in graphene.

Mobility of graphene is nearly independent of temperature between 10 K and 100 K

- Mobility: 200,000 $cm^2V^{-1}s^{-1}$ at a carrier density of 10^{12} cm^{-2} [28]
- Resistivity: 10^{-6} Ω.cm

4, 5 & 6. Density, Mobility and Electricity

Graphene also has "the highest current density (a million times than that of copper) at room temperature; the highest intrinsic mobility (100 times more than in silicon); high intrinsic mobility (200 000 cm^2 v^{-1} s^{-1}) and conducts electricity in the limit of no electrons".

Which means it can carry more electricity more efficiently, faster and with more precision than any other material.

7. Transparency

Being atomically thin, graphene exhibits remarkable optical properties, absorbing just 2.3 % of white light with a hardly-noticeable opacity arising from coupling of incident photons to relativistic electrons. That means we can still see a single layer of atoms with our naked eye. It has optical transmittance (~ 97.7%) and good electrical conductivity merit attention for applications such as for transparent conductive electrodes [30, 31]. As well as making graphene even more useful as a potential solar cell component, its transparency makes it ideal for use in touchscreens.

8 & 9. Stretch and Stiff

Graphene stretches up to 20 percent of its length. And yet it is also the stiffest known material — even stiffer than diamond.

10. Thermal Conductivity

Electrons move through graphene with almost no resistance, generating little heat. What's more, graphene is itself a good thermal conductor, allowing heat to dissipate quickly.

Graphene also beats diamond in thermal conductivity. In fact, graphene now holds the record for conducting heat — it's better than any other known material. Materials such as graphene have a higher thermal conductivity and so can remove this waste heat more efficiently than materials such as silicon with a lower thermal conductivity.

The thermal conductivity of graphene strongly depends on the material's isotopic composition. Researchers have shown that graphene made from pure carbon-12 has a much higher thermal conductivity than normal graphene – which contains about 1% carbon-13 (two stable isotopes of carbon occur in nature – carbon-12 comprising about 99 % of naturally occurring carbon and carbon-13 about 1 %.). As well as helping to develop an accurate theory of heat conduction in 2D materials, the result means that isotopically pure graphene could be ideal for cooling tiny components in electronic circuits [32].

Heat travels through crystalline materials such as graphene by way of lattice vibrations called phonons. Atoms with different masses scatter phonons differently, and therefore thermal-conductivity studies of graphene with varying isotopic compositions should help physicists gain a better understanding of how atomic mass affects the transport of heat.

Twice the Conductivity.

Using an opto-thermal laser Raman technique, originally developed in Balandin's lab and subsequently modified by Ruoff's group, the researchers found that the thermal conductivity of isotopically pure carbon-12 graphene (containing just 0.01 % carbon-13) is higher than 4000 $Wm^{-1} K^{-1}$ at a temperature of 320 K, while graphene with 1% carbon-13 has a conductivity of 2500 $Wm^{-1} K^{-1}$. The thermal conductivity drops to about 2000 $Wm^{-1} K^{-1}$ in graphene sheets made up of half carbon-12 and half carbon-13. In comparison, bulk copper, which is widely used to cool computer chips, has a thermal conductivity of about 400 $Wm^{-1} K^{-1}$.

11. Impermeable

Graphene is also the most impermeable material ever discovered. "Even helium atoms cannot squeeze through" [33]. This makes it a great material for building highly sensitive gas detectors, for example, since even the smallest quantity of a gas will get caught in its lattice, changing its electrical behavior.

12. Piezoelectricity

Piezoelectricity is the property of a material's ability to produce an electric charge when bent, squeezed, or twisted. It is reversible, which means when an electric field is applied the piezoelectric material changes its shape. This provides the user with a remarkably high level of control because the way the electrical field strains or deforms can be predicted. Some of the more common applications where piezoelectricity is used include watches, radios, and ultrasound equipments.

According to the researchers, lithium-atoms adhered to a graphene lattice can produce electricity when bent, squeezed or twisted. Conversely, the graphene material will deform when an electric field is applied, opening new possibilities in

nanotechnology [34].

13. Biocompatibility

Is graphene toxic? The answer to this question is 'no'. Graphene has enormous potential beyond electronic and chemical applications towards biomedical areas like, precise bio-sensing through graphene fluorescence, graphene-enhanced cell differentiation and growth, drug/gene delivery for cancer treatment, and graphene-assisted laser desorption/ionization for mass spectroscopy and DNA sequencing [35]. Imagine a sheet of graphene with a small gap, big enough to allow a strand of DNA to pass through, like thread through cloth. As the DNA passes through the sheet, the electrical properties of graphene change on exposure to each base pair. Because it is 2D, it can "read" one base at a time, making it much more accurate than anything used today [36].

Finally, graphene has a role to play as a component, and as a constituent. All the chemical derivatives of graphene are useful including fluorographene,

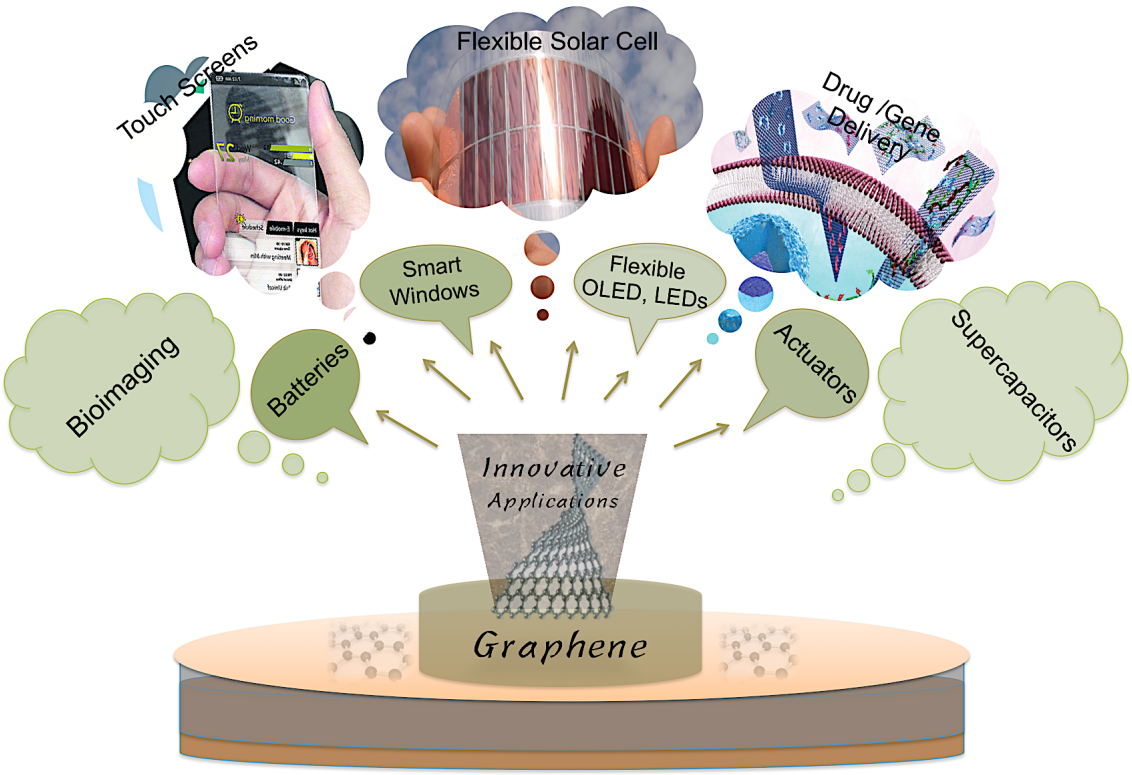

Figure 8. Schematic representation of the application opportunities of graphene in various fields.

graphene oxide (GO) and hydrogenated graphene. The scheme in **Figure 8** shows the fast growing pool of innovative applications based on graphene and its derivatives.

These salient features of graphene make it a good contender for yet another record, the material with the most records. For a substance that's only been closely studied since 2004, this makes it a shining star of material science, and one well worth the intense interest it continues to generate.

Why Graphene Oxide?

The successful preparation and verification of a mechanically exfoliated graphene monolayer by Novoselov *et al.* in 2004 has fueled the exponential growth of research on graphene-related materials [8]. GO has attracted magnificent attention, owing to the escalating demands for seeking scaled-up production of graphene and exploring their potential applications in various technological fields. Different from graphene that is a single-layer sheet composed purely by carbon atoms, the individual GO sheet is enriched with oxygen-containing groups such as epoxide (a cyclic ether with three ring atoms), hydroxyl (-OH) on the basal plane and carboxylic acid (-COOH) groups at the peripheral [37], and is highly soluble in water (**Figure 9**). As a consequence, a proposed three-step approach mentioned below, opens up a promising routeto achieve large-scale production of graphene. i.e.,

1. Synthesis of graphite oxide from pristine graphite power;
2. Exfoliation of graphite oxide in water to generate a dispersion of single-layer GO; and followed by
3. A chemical or thermal reduction of GO to graphene;

On the other hand, these reactive terminal functionalities can serve as the initial binding sites to direct well-controlled surface interactions, thus to achieve either a designed functionalization of GO or constructions of hierarchically structured graphene materials.

The existing approaches to yield graphene include mechanical exfoliation, chemical vapor deposition (CVD), and chemical or thermal reduction of GO. Among them, the last one is considered to be the most economical way to produce a large quantity of graphene.

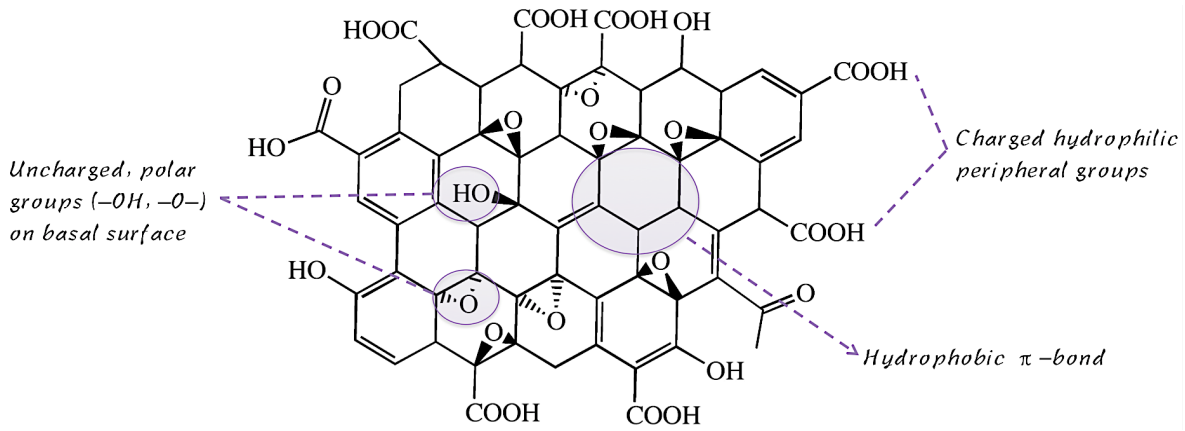

Figure 9. Idealized structure proposed for GO. Courtesy: *Hamilton, C.* (2009) Rice University, Houston, TX.

Due to the hydrophilicity and ionizability of its oxygen-containing functional group, graphite oxide can be readily exfoliated in water to yield stable dispersions of GO layers. Such behavior potentially allows the large-scale preparation of single-layer graphene. GO can be defined as a special nanomaterial with,

1. Incredibly large surface area owing to the two accessible sides; and
2. Rich interfacial chemistry due to the surface functionalities such as epoxide, hydroxyl and carboxylic groups, which could potentially facilitate or direct the deposition of metal nanoparticles, organic macromolecules and even some biological species.

For example, GO as a matrix for enzyme immobilization has been reported. Without using any cross-linking reagents and additional surface modification, those abundant surface terminal groups make the adsorption of the protein molecules quickly through electrostatic interactions and those proteins maintain their specific bioactivity afterwards [36].

Regarding the fabrication of GO with metal nanostructures, various approaches ranging from *ex-situ* hybridization to *in-situ* crystallization have been developed. Particularly, the chemical reduction method is the most popular strategy. Precursors of noble metals such as $HAuCl_4$, $AgNO_3$, K_2PtCl_4 and H_2PdCl_6 can be simply reduced by agents like amines, $NaBH_4$, and ascorbic acid [38].

From an assembly point of view, these atomically thin carbon sheets of either SLG or few-layer graphene (FLG) are well compatible with existing planar

device architectures. On the other hand, one significant advantage of graphene-related nanomaterials is their highly tunable electrical properties such as carrier type or density, and rich electronic band structures. For instance, while SLG has a zero band gap, few-layer graphene differ from the intrinsic SLG in that they have various band gaps as a function of number of layers. Consequently, a delicate control of graphene films with well-defined band gaps allows us to regulate their electronic properties.

Potential applications of graphene sheets as ultrathin transistors, sensors and other nanoelectronic devices require them to be supported on an insulating substrate. Therefore, a quantitative understanding of charge exchange at the interface and spatial distribution of the charge carriers is critical for the device design.

Properties of GO

GO, is often described as an electrical insulator, due to the disruption of its sp^2 bonding networks. By reduction process we can reduce the number of sp^3 bonding sites, simultaneously increase the sp^2 bonding and thus increase conductivity. The ability for GO to conduct electrons actually depends on the amount of oxidization in the compound, as well as the method of synthesis. Alternatively, the electronic structure of graphene can be modified chemically [39], as shown in **Figure 10.**

There are many ways available in which GO can be functionalized, depending on the desired application. Both small molecules and polymers can be covalently attached to the reactive oxygen functionalities, or non-covalently attached to the graphitic surfaces. The functional groups bonded to the basal surface and laminar edges act as artificial lattice defects to limit electron/hole mobilities and introduce a significant bandgap into graphene crystals. As a result, the ballistic transport of charge carriers will be effectively scattered or spatially confined [40-55].

The intrinsic structure and outstanding electrical conductivity of graphene can be restored to a large extent upon reduction of the functionalized GO, effectively accelerating the switching and accessing of the graphene-based devices [41-52].

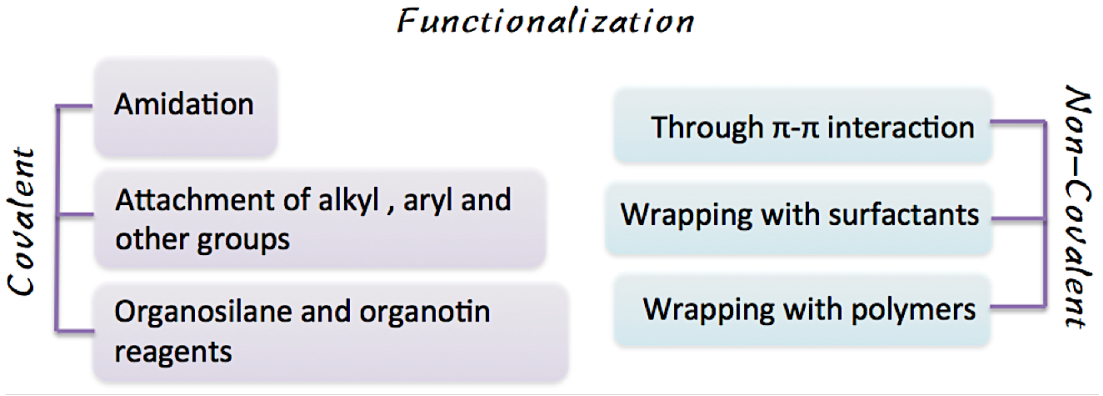

1.4 Strategies for the Synthesis of Graphene and GO

There are two approaches that can be adapted for the synthesis of graphene i.e., top-to-down and bottom-to-up (**Figure 11**). *Top-down* approaches involve breaking apart the stacked layers of graphite to yield single graphene sheets, whereas *bottom-up* methods involve synthesizing graphene from carbon containing sources [56].

For top-down methods separating the stacked sheets means that the van der Waals forces that hold the layers together must be overcome, which is not a trivial task despite the relatively low interlayer bonding energy [57-59]. Key challenges in this area include effectively separating the layers without damaging the sheets, and preventing re-agglomeration of the sheets once the layers have been exfoliated.

For bottom-up methods high levels of graphitization must be promoted to produce good quality material, so these methods generally require high temperatures. The processes involved are usually simple, although the material produced can contain higher levels of defects than observed for top-down methods. In addition to forming graphene nanosheets, bottom-up methods can also be used to form large area graphene films via growth on certain substrates.

Top to Down Methods.

1.4.1 Micromechanical Cleavage

A sticky 'tape' is placed on to a block of graphite and then peeled back, stripping a thin layer off the top, this method is called as the 'scotch tape' or 'peel-off' method and was the first method used to experimentally isolate graphene [8, 60]. Repeated cleavage yields mono-, bi- and few-layer graphene,

Figure 11. Bottom to up and top to bottom approaches for the synthesis of graphene.

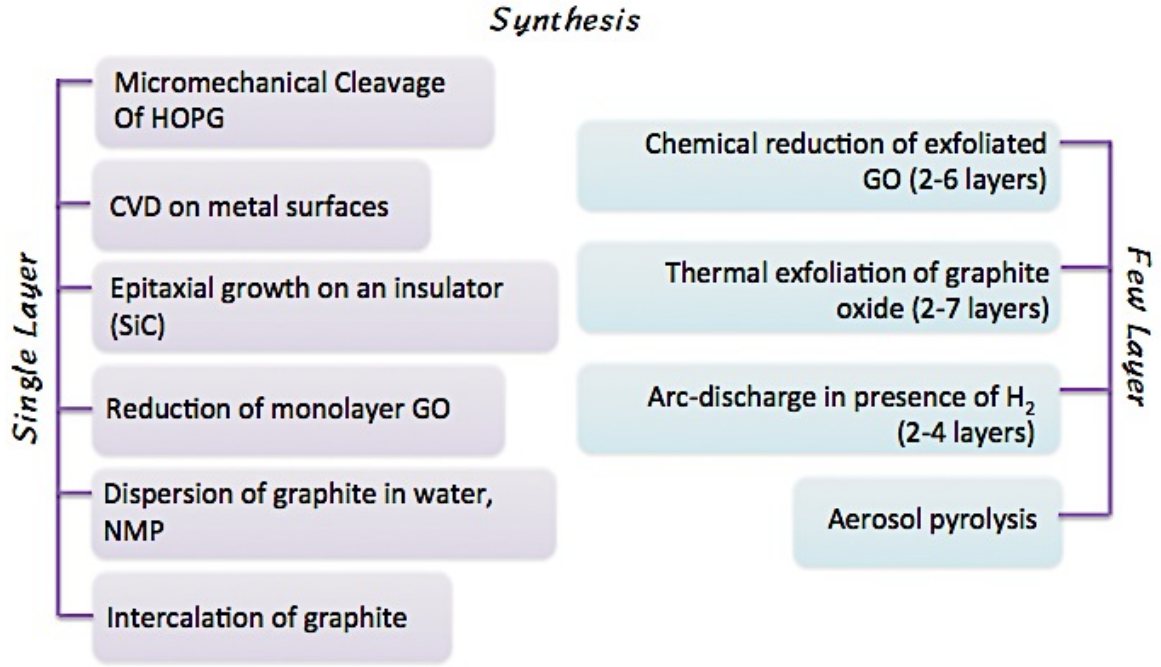

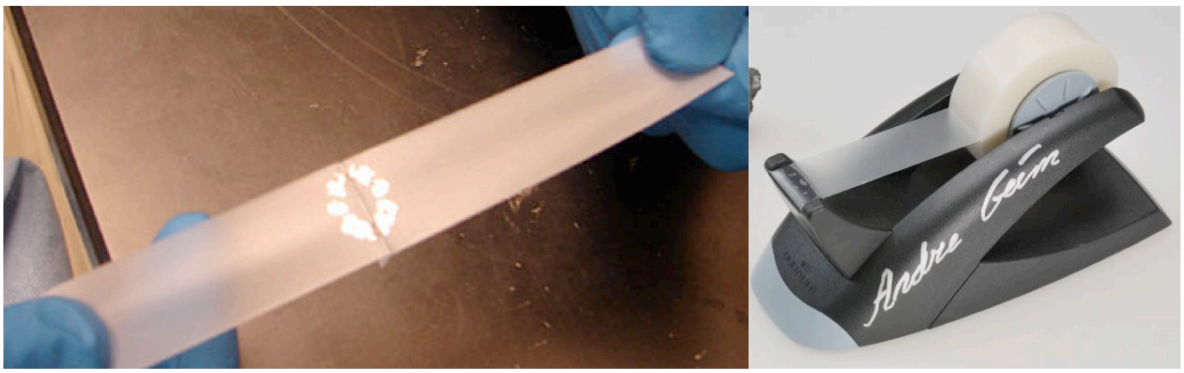

Figure 12. Micromechanical exfoliation of graphite flake. Adhesive scotch tape is pressed against a 2D crystal so that the top few layers are attached to the tape. The tape with crystals of layered material is pressed against a surface of choice. Upon peeling off, the bottom layer is left on the substrate.

which are identified by optical microscopy over specially prepared SiO_2(300 nm)/Si substrates, taking advantage of the change in refractive index between graphene and 300 nm thick SiO_2.

The sheets are of high quality as a result of the limited graphite processing required, but the method is slow and labor intensive so the material produced is often reserved for study of the fundamental properties of graphene rather than using for commercial applications.

1.4.2 Electrochemical Exfoliation

In previous reports, the set-up for electrochemical exfoliation of graphite involved using graphite as a sacrificial electrode, and collecting the exfoliated material from the electrolyte solution (**Figure 12**). Electrolytes used to-date includes surfactant [61] and H_2SO_4-KOH solutions [62], which serve different functions in the process. Surfactants prevent re-agglomeration of the graphene; with the hydrophobic groups interacting with the p-orbitals of graphene, and the hydrophilic groups stabilizing the sheets in water [63]. However, surfactants can be difficult to remove [61], and their presence has been shown to affect the electrical and electrochemical properties of graphene [64]. H_2SO_4 was found to be a good electrolyte for graphite exfoliation, which is thought to be due to intercalation of $[SO_4]^{2-}$ ions, often detected after processing, between the graphite layers [62]. Here it is necessary to add KOH to the electrolyte to reduce the high levels of oxidation observed when using only H_2SO_4. In both cases the electrochemical exfoliation produces a mixture of different thicknesses of graphite flakes, with few-layer graphene being isolated by centrifugation.

More recently electrochemical strategies have included expanding the graphite electrode in situ, followed by exfoliation of the electrode using sonication [65, 66]. This expansion has been achieved by intercalation of lithium salts to form graphite intercalation compounds (GICs). Sonication acts to separate the layers by injecting thermal shock into the material through ultrasonic cavitation [67]. Sonication of lithium salt intercalated graphite in a mixed solvent of dimethylformamide (DMF) and propylene carbonate has been reported to give > 70 % few-layer graphene [65], while > 80 % few-layer graphene has been reported for sonication in water [66], where lithium and water react to form hydrogen gas which is thought to further aid exfoliation.

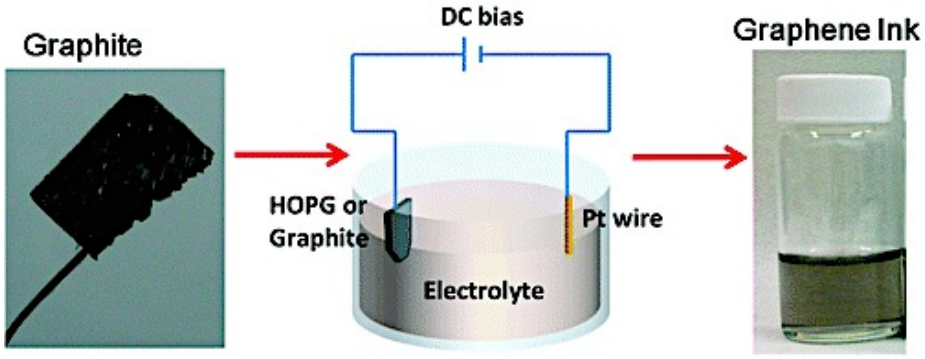

Figure 13. Schematic illustration of electrochemical exfoliation of graphite to produce thin graphene sheets (dispersed in DMF). *Reproduced by the permission of American Chemical Society, Ref. 62.*

1.4.3 Exfoliation of GICs

Numerous strategies have been utilized for the production of graphene from GICs, including solvent-assisted and thermal exfoliation. For solvent assisted exfoliation GICs are generally sonicated in solution to aid exfoliation, although spontaneous exfoliation of alkali metal GICs in N-methyl-pyrrolidone (NMP) has been reported [68]. In addition to the intercalation of solvent molecules expanding the layers [69], interaction with the solvent may cause gas to be expelled that aids exfoliation and for sonication of alkali metal GICs in ethanol [70], where alkali metal ethoxide and hydrogen gas are formed.

The effect of thermal expansion of GICs was reported as early as 1916 for heating graphite-bromine intercalation compounds [71], but marked interest in the field did not begin until the late 1960s, when foils of exfoliated graphite were designed as gasket and sealant materials [72]. Heating of GICs generally causes thermal decomposition of intercalates into gaseous species that push the layers apart. 'Expanded graphite (EG)', also known as 'exfoliated graphite', has many industrial applications such as thermal insulators and composite filler materials, and more recently has been considered as a precursor for graphene [72].

The most common method for EG formation is via the exposure of graphite to strong acids to yield a GIC (often graphite bisulfate), which is then exfoliated by rapid thermal heating or, more recently, by microwave radiation [73]. Mono- to few-layer graphene has been reported for EG ground in ethanol [74], or sonicated in NMP [75], while repeated cycles of intercalation-exfoliation followed by sonication in DMF has been shown to yield over 50 % mono- and bi-layer

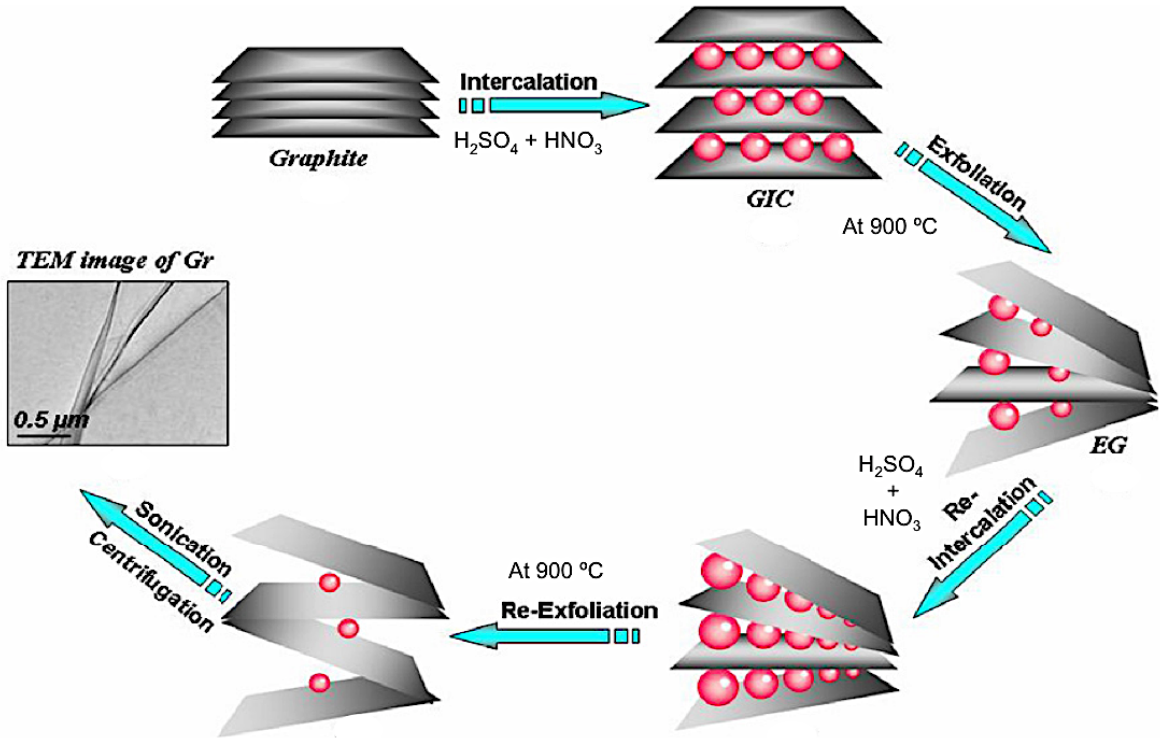

Figure 14. Schematic representation of an approach to produce single and double layer graphene from re-exfoliation of EG. *Reproduced by the permission of Elsevier, Ref. 76.*

graphene (**Figure 14**) [76].

Other examples of GICs designed for thermal exfoliation include graphite co-intercalated with iron chloride ($FeCl_3$) and nitromethane (CH_3NO_2) [77], and graphite intercalated with ionic liquid crystals (ILC) [78]. In the former iron chloride is used to promote the intercalation of nitromethane, which decomposes at relatively low temperatures (~ 100 °C) under microwave radiation, while in the latter mild heating is used to promote ILC intercalation due to their reduced viscosity at higher temperatures, and stronger heating (to 700 °C) is used to induce thermal decomposition. Based on a similar principle supercritical carbon dioxide (CO_2) has been used to exfoliate graphite based on intercalation of the CO_2 in the supercritical phase followed by rapid expansion upon depressurization to form gaseous CO_2 which forces the graphitic layers apart.

1.4.4 Solvent-Based Exfoliation

The exfoliation of unmodified, natural flake graphite via sonication in solvents was reported in 2008 by two separate groups [79, 80]. Since then

numerous articles have been published on what makes a suitable solvent for graphite exfoliation, and what processing conditions are required to achieve stable, highly concentrated dispersions of graphene sheets. A study of graphene dispersibility in 40 different solvents concluded that the best solvents have a Hildebrand solubility parameter of $\delta_T \sim 23$ MPa$^{1/2}$, Hansen solubility parameters of $\delta_D \sim 18$ MPa$^{1/2}$, $\delta_P \sim 9.3$ MPa$^{1/2}$ and $\delta_H \sim 23$ MPa$^{1/2}$, and surface tension close to 40 mJ m^{-2} [81]. The best solvent with regard to the percentage of monolayer graphene dispersed was found to be NMP, while the solvent that gave the highest absolute concentration (mono- and few-layer graphene) was found to be cyclopentanone, with a solubility of 0.0085 ± 0.0012 mg mL^{-1}.

Dispersions with high concentrations of graphene are advantageous, as they require smaller volumes of potentially expensive and hazardous solvents, so several approaches have been tried to increase graphene concentration. Simply increasing sonication time or sonicating with a sonic probe rather than a sonic bath has been shown to increase the concentration of graphene in solution (**Figure 15**) [82–84]. Many of the best solvents for graphene have high boiling points, for example NMP has a boiling point ~ 200 °C, which makes removal difficult when forming films or coatings from solution. Extended sonication (48 hours) in 'poor' but low boiling point solvents has achieved graphite concentrations up to 0.5 mg mL^{-1} [85], which is approximately half the value reported for NMP after 460 hours of sonication [82]. It should be noted that while prolonged sonication time improves the dispersibility of graphene the increase in concentration has shown to be accompanied by a decrease in flake size and an increase in defect concentration [82].

Another strategy for exfoliation of unmodified graphite flakes involves sonication in aqueous surfactant solutions [86, 87], which has the advantage of avoiding expensive and often harmful solvents. In addition the surfactants can prevent re-aggregation of the graphene due to the repulsive potential barrier between surfactant-coated sheets, the importance of which has been studied with regard to graphene dispersion for both ionic and non-ionic surfactants [88]. Concentrations up to 0.3 mg mL^{-1} have been reported for graphene sonicated in sodium cholate solutions for ~ 400 hours [87], but as with electrochemical exfoliation in surfactant solutions, this method has the disadvantage that surfactants are difficult to remove and can affect properties.

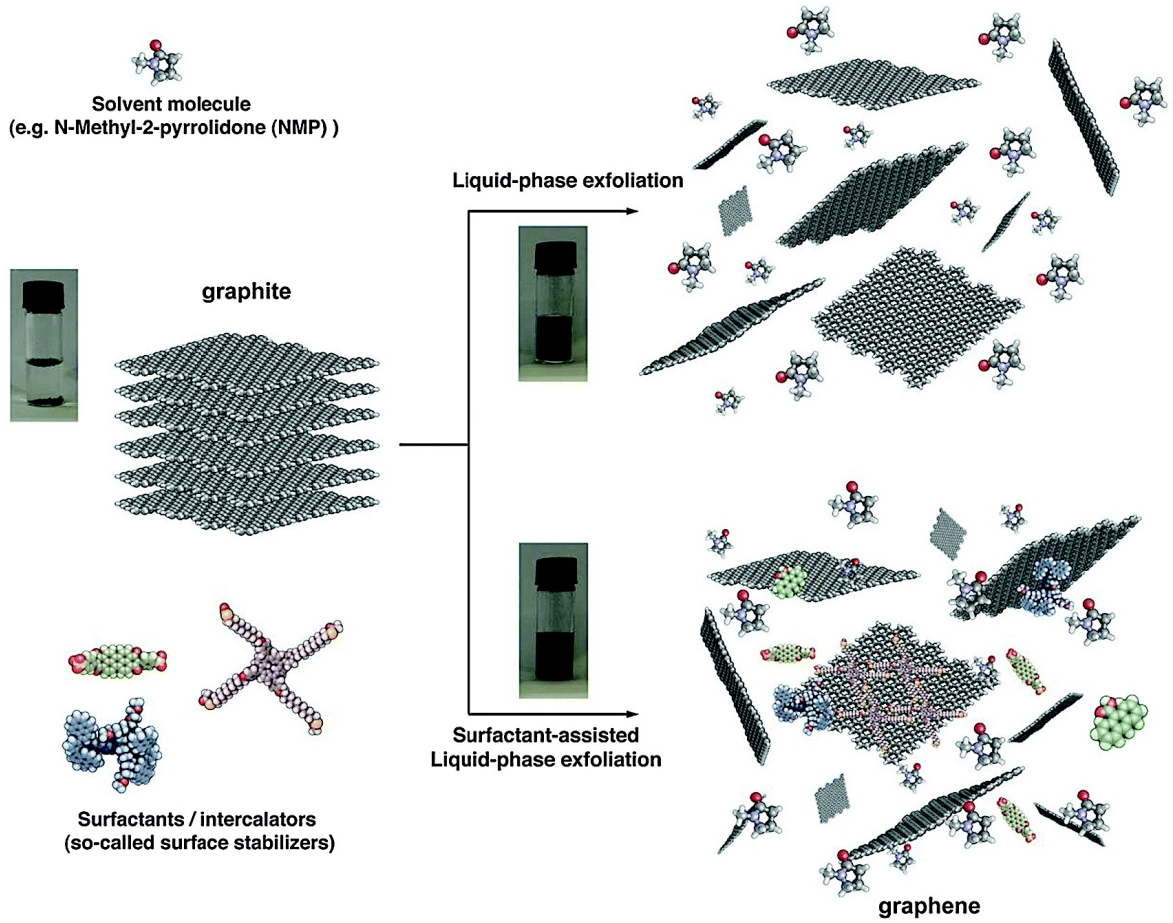

Figure 15. Schematic representation of the liquid-phase exfoliation process of graphite in the absence (top-right) and presence (bottom-right) of surfactant molecules. *Reproduced by the permission of RSC Publishing, Ref 84.*

1.4.5 Exfoliation of Graphite Oxide

The method of obtaining graphene, which has received most attention, is exfoliation and reduction of graphite oxide. Historically graphite oxide has been synthesized via oxidation of graphite using concentrated acids and strong oxidants, in the Straudenmaier, Brodie or Hummer's methods [89], and while adaptations to these methodologies have been proposed since [90-93], the Hummer's method remains the most widely used process. The structure of graphite oxide has been described by a number of different models, as discussed by Dreyer et al. [94] One widely accepted model is the Lerf-Klinowski model, [95, 96] which describes graphite oxide as having a layered structure with hydroxyl and epoxy groups on the basal planes and carboxylic and carbonyl groups at the sheet edges **Figure 9**. These oxygen-containing groups make graphite oxide hydrophilic, and the presence of functional groups between layers also results in graphite oxide

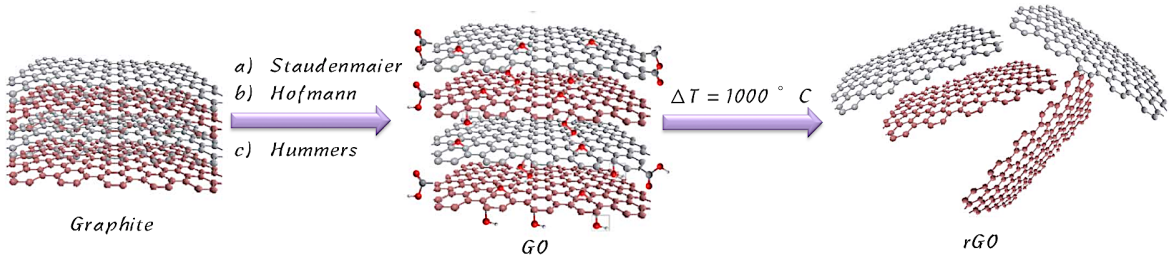

Figure 16. Schematic diagram of the procedure for the production of thermally reduced graphene. An oxidative treatment of graphite using **(a)** fuming nitric acid and H_2SO_4 in the presence of $KClO_3$ (Staudenmaier method) or **(b)** 68% nitric acid and H_2SO_4 in the presence of $KClO_3$ (Hofmann method) or **(c)** H_2SO_4 in the presence of $KMnO_4$ and $NaNO_3$ (Hummers method) was performed to generate graphite oxides which were consequently thermally exfoliated to thermally reduced graphene, *Ref. 88.*

having a larger interlayer spacing (6–12Å depending on the amount of intercalated water) than graphite (3.4 Å) [97].

Graphene is obtained by exfoliation of graphite oxide into GO, followed by reduction of GO to produce graphene (**Figure 16**). The resulting material is generally termed 'reduced graphene oxide' (rGO) or 'functionalized graphene' rather than 'graphene' as complete reduction has not yet been achieved. Graphite oxide is exfoliated more readily than graphite, using thermal treatments or via sonication in water [94], and the graphene oxide produced can then be reduced using either thermal or chemical methods. The different methods of reduction have been reviewed recently [98, 99].

1.4.6 Arc Discharge

Arc discharge, where a direct current is passed between high purity graphite electrodes, has been widely used in the synthesis of carbon nanomaterials including fullerenes and carbon nanotubes [100]. More recently arc discharge has been used to synthesize few-layer graphene in a number of different buffer gases (**Figure 17**) [101–103]. The presence of hydrogen gas in the buffer is thought to be important to terminate dangling carbon bonds and hence inhibit the rolling-up and closing of graphitic sheets [101, 102] and a mixture of helium and hydrogen gas was found to produce the highest crystallinity material from a number of different buffer gases studied [103].

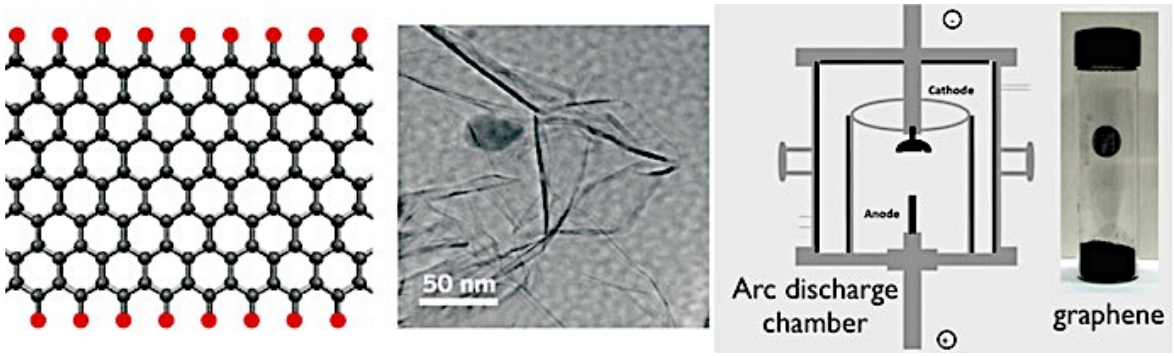

Figure 17. Flakes In the presence of hydrogen (red, left image), an arc-discharge method produces graphene flakes two to four layers thick. Fitted with graphite electrodes, arc-discharge instruments, which previously have been used to make nanotubes and other helical carbon structures, can be operated in a way that yields graphene (right image). *Reproduced by the permission of American Chemical Society, Ref. 101*.

1.4.7 Unzipping CNTs

Nanotubes are single sheets of graphite rolled up into a cylinder. But no one thought that nanotubes could be cut along their axis and flattened out to make such sheets (**Figure 18**) [104]. Graphene or few-layer graphene can be

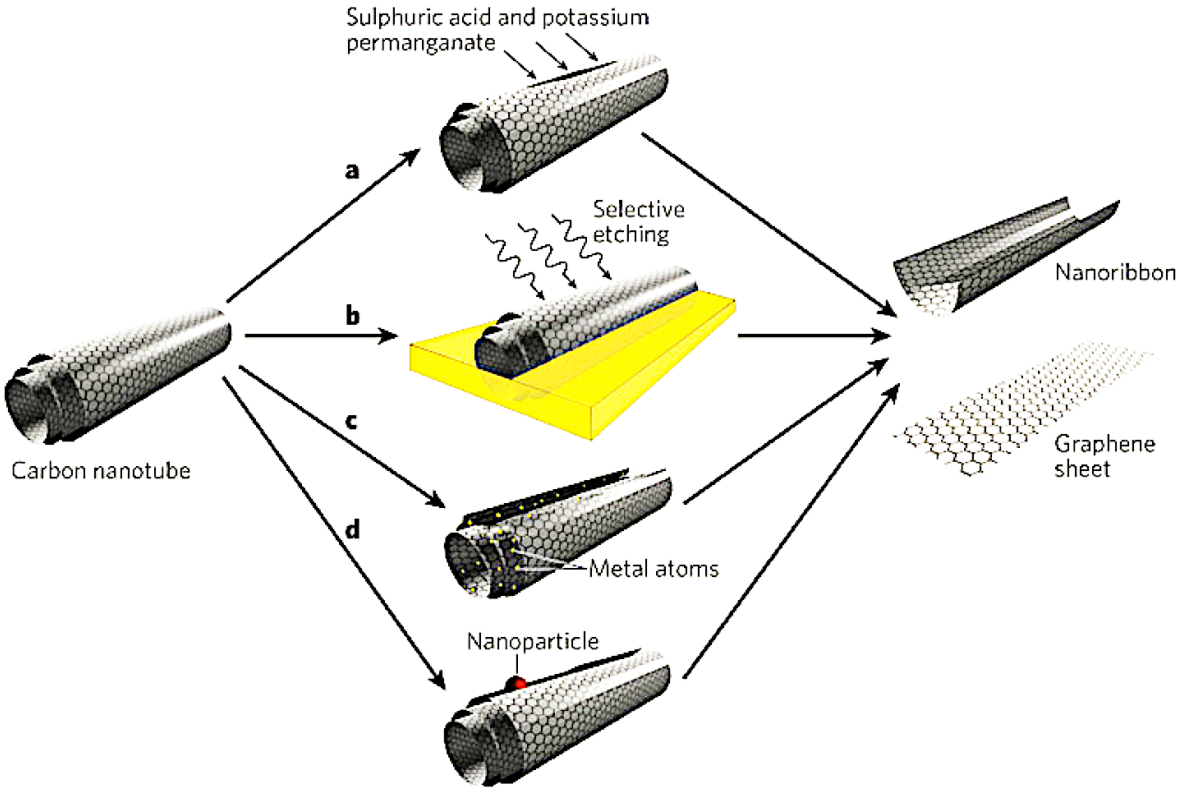

Figure 18. Methods of unzipping CNT. *Reproduced by the permission of Macmillan Publishers Limited, Ref. 104.*

synthesized by unzipping single or multi-walled CNT respectively using wet chemistry methods such as strong oxidizing agents [105], or by physical methods such as laser irradiation [106] and plasma etching [107, 108]. This unzipping results in graphene 'nanoribbons', with ribbon widths dictated by the diameter of the tubes. Graphene nanoribbons are considered as quasi 1D materials, and have different properties depending on their width and edge type (armchair/zigzag), as discussed elsewhere [109, 110]. CNT unzipping occurs via C-C bond fission which is often initiated at defect sites, leading to irregular cutting [111].

Recently the synthesis of well-regulated nanoribbons has been demonstrated via unzipping of flattened CNTs, where attack occurs preferentially along the bent edges [112]. Producing graphene from CNTs is set to raise interesting questions as graphene is often seen as a replacement or alternative to nanotubes.

Bottom to Up Methods

1.4.8 Epitaxial Growth on Silicon carbide (SiC)

Briefly, a small amount of SiC (about 10 mm 10mm) is placed in a box with a small hole in it. The box is sealed in a vacuum or argon and heated to about 1500 °C. Silicon molecules 'evaporate' from the surface, leaving layer of graphene.

The formation of graphene on SiC proceeds via the preferential sublimation of silicon from the SiC surface and subsequent graphitization of the excess carbon atoms left behind [113]. This process occurs at high temperatures generally

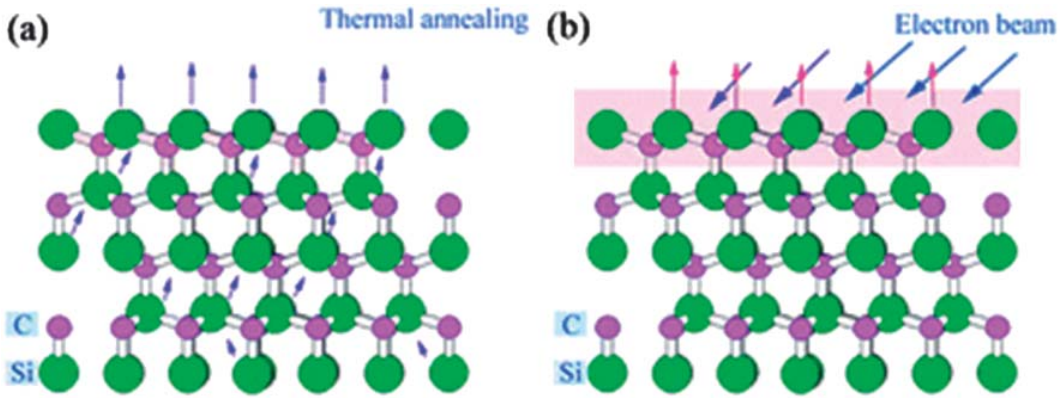

Figure 19. Schematic description of Si atom sublimation in Si-terminated 4H-SiC under thermal annealing process **(a)** and pulsed electron beam irradiation process **(b).** *Reproduced by the permission of The American Physical Society, Ref. 118.*

(> 1000 °C) and is generally performed in ultra-high vacuum (UHV) conditions, although growth in argon atmospheres [114-116] or in the presence of small quantities of disilane [117] has been shown to reduce the rate of silicon sublimation, allowing higher temperatures to be used which results in higher quality graphene. Preferential Si sublimation can also be induced by pulsed electron irradiation (**Figure 19**) [118].

The demanding growth conditions are one of the key challenges of growing graphene on SiC. One solution that allows lower temperature conditions (700-800 °C) is nickel-catalyzed growth, where a thin layer of nickel is deposited on the surface of the SiC prior to annealing, and graphene forms on the upper nickel surface [119-122]. While this method uses lower temperatures, it has the additional cost of using a transition metal and requires transfer to insulating substrates for use in electronic applications.

Graphene growth on SiC is generally for wafer-based applications, such as electronic devices or components, and as such it is not generally necessary to remove the graphene from the underlying substrate. However the transfer of graphene directly from SiC has been demonstrated [123, 124], although is hindered by the strong interactions between the two materials [125]. SiC is commercially available but expensive, particularly for large area films, so a hurdle for their use in commercial applications will be reducing this cost. Cubic SiC is cheaper to produce [126] and could be a viable alternative but graphene growth on this phase is still in its infancy.

1.4.9 CVD

Growth on Metals.

The CVD processes generally utilize transition metal surfaces for growth of graphene using hydrocarbon gases as graphene precursors at the deposition temperature of about 1000 °C, represents a very active area of graphene research. CVD graphene growth can be categorized as proceeding through either surface-catalyzed or segregation methods depending on the metal. For surface catalyzed reactions, the decomposition of the carbon containing species and graphene formation occur at the metal surface, and growth can be described as "self-limiting" to monolayer graphene as the surface is pacified once covered. The number of graphene layers produced by segregation depends on various factors including the amount of carbon dissolved and the rate of cooling [127, 128].

Graphene growth has been demonstrated on a wide range of metals, including group 8–10 transition metals (Fe, Ru, Co, Rh, Ir, Ni, Pd, Pt, Cu, Au and a number of alloys (Co–Ni, Au–Ni, Ni–Mo, stainless steel [129]). The optimum conditions for CVD growth vary depending on the metal, with different factors (pressure, temperature and carbon exposure) influencing the graphene quality and thickness. In addition, the strength of graphene–metal inter- action differs, which can impact the degree of graphene rippling, the sensitivity of graphene to defects in the metal surface, and the ease of graphene transfer to arbitrary substrates. While there are a number of fundamental properties that affect the potential of a metal for use in large-scale CVD growth, ultimately cost and availability are likely to be some of the most important factors, particularly as the metal is generally etched during graphene transfer (**Figure. 20**). CVD growth over metals has the disadvantage that harsh growth conditions are required, especially for the metals that utilize UHV conditions. Improving these conditions can be complicated, for example while growth over copper has been demonstrated under atmospheric pressure conditions, patches of multi-layer graphene were observed on the surface suggesting that unlike in UHV conditions, the growth is not self limiting to monolayer graphene [130]. Attempts have also been made to reduce the temperatures required for growth, for example using carbon sources with lower decompositions temperatures [131, 132]. The different conditions for graphene growth over poly-crystalline metals have been recently reviewed elsewhere [133].

Metal films are electrically conducting so to enable the use of CVD grown graphene films in a number of electronic applications, transfer of graphene films onto insulating substrates is required. The transfer of graphene from different metals has been demonstrated using a variety of chemical etchants to release the graphene from the metal [133]. This process can be damaging for the films, so often a polymer support is used to prevent the films cracking [134, 135]. The general method for this is to spin coat the polymer onto the graphene surface,

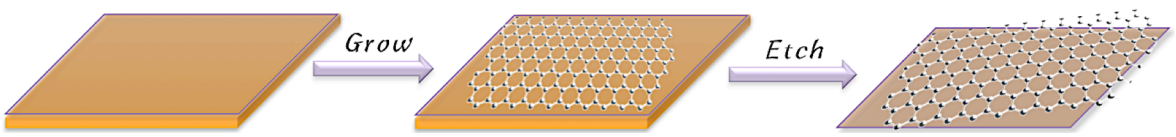

Figure 20. A schematic of graphene growth and removal from metal surfaces.

etch the underlying metal, place the graphene on the new substrate, and dissolve the polymer to yield naked graphene. Furthermore, graphene transfer onto flexible substrates has been demonstrated using industrially compatible techniques such as hot press lamination [136] and roll-to-roll transfer [137], allowing the transfer of large area films. As for transfer using a polymer stamp these processes also require etching of the metal, which is both costly and wasteful. Recently transfer via electro- chemical delamination has been presented where only a small amount of the metal is etched, allowing the copper substrate to be reused in subsequent growth reactions [138].

It should be noted that in addition to CVD growth via vapors introduced into the furnace during the reaction, graphene has been grown from solid carbon sources positioned on-top of the substrate, for example the transition metal mediated graphitization of amorphous carbon films [139, 140], nanodiamonds [141], polymers [142, 143] and self-assembled mono- layers (SAMs) [144].

Substrate Free.

Besides growing graphene films, CVD has been also used to synthesize graphene nanosheets. Substrate free synthesis has the advantage that specific substrates do not need to be purchased or prepared and that the removal of graphene from the substrate is not required. Furthermore as the material is collected outside the furnace, graphene can be produced via continuous rather than batch processing. An early example of substrate free growth is the work by Dato et al. [145, 146], where the growth of single and bilayer graphene has been reported via atmospheric pressure, microwave-enhanced CVD of ethanol. More recently a route to produce few-layer graphene via substrate free CVD has been demonstrated using thermal decomposition of sodium ethoxide in ethanol [147]. Both methods yield large quantities of graphene.

Apart from this, graphene nanosheets have been synthesized by a number of other methods, resulting in material with different thicknesses and morphologies. One of the best known of these is graphene synthesis via the ash pyrolysis of the solvothermal product of sodium and ethanol [148]. The synthesized graphene product is reported as having a ‘foam like structure’ consisting of individual graphene sheets held into a porous structure, which can be separated into individual sheets by several minutes sonication in ethanol. There are also a number of methods that produce few-layer graphene via the reduction of carbon

containing species, using methods such as igniting magnesium in dry ice [149], calcining calcium carbonate with magnesium powder [150], and calcining aluminum sulphide (Al_2S_3) in carbon monoxide [151].

1.5 Techniques for the Placement and Assembly of GO

Assembly of nanomaterials is one of the most fundamental issues in nanoscience. Rational assembly strategies are needed not only to build complex structures with novel collective properties but also to pattern nanoscale building blocks for device fabrication at a practical scale. Although *top-down* approaches such as nanoimprint lithography, near-field lithography, and scanning probe techniques have demonstrated high spatial resolution, *bottom-up* methods are still highly desirable for their simplicity and compatibility with large-scale, heterogeneous integration processes.

Significant progress has been made in the chemical synthesis of GO with good control over its size, thickness and crystallinity. However, major advances in the field of assembly must be made in order to fully utilize the functionality offered by monolayer sheets and to realize its full potential for optical, electronic, and magnetic devices. There are several different techniques available for preparing GO

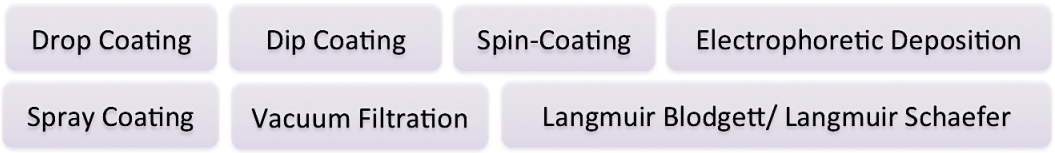

There are plethora of reports regarding the placement and organization of GO using various approaches including dip coating [152], drop coating [153], spin-coating [154-156], electrophoretic deposition [156], spray coating, vacuum filtration [157, 158], Langmuir-Blodgett (LB) [159, 160] and Langmuir-Schaefer (LS) deposition [161] and they have shown promising results in preparing graphene layers with high degree of control. The challenge now is how to transfer the monolayer GO in dispersion onto a substrate in a controlled manner.

1.5.1 Drop casting

It is a very simple, solution based deposition method. A drop of the dissolved material is cast on the substrate and the solvent is allowed to evaporate. This technique usually gives films of low optical quality and very small area (typically 1-

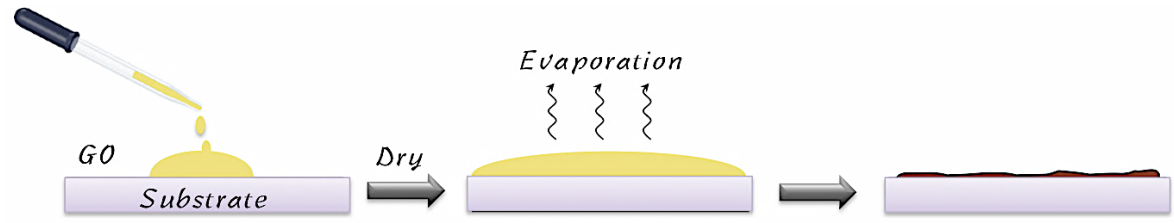

Drop Coating Process

3 mm^2), however due to its simplicity it is quite commonly used.

Positives:

- Very simple technique
- No wastage of the processed sample

Negatives:

- Limitation in large area coverage
- Film thickness is hard to control
- Poor uniformity

1.5.2 Dip Coating

Another approach by Wang et al [153] demonstrated the use of dip coating technique for the formation of a transparent, conducting and ultrathin graphene film to be employed as an electrode for solid-state dye-sensitized solar cells. Although the assembly and density of GO layers can be optimized through this technique but monolayers with controlled spacing cannot be obtained.

Positives:

- Good Uniformity

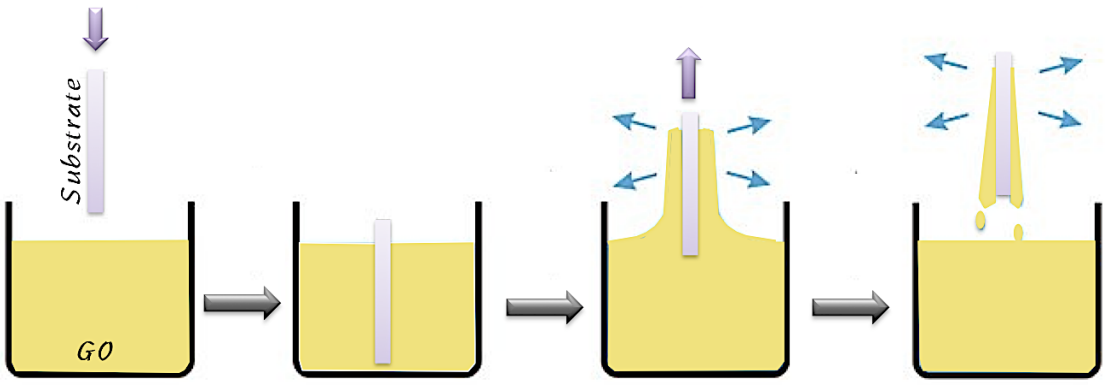

Dip Coating Process

- Thin layers can be achieved
- Large area coverage

Negatives:

- Wastage of the sample
- Time consuming
- Both side film formation

1.5.3 Spin Coating

Many researchers have employed spin coating technique for the evaluation of solution processed reduced GO film as transparent conductor [154]. As the spinning of the sample begins, the centrifugal force removes most of the solution from the surface of the substrate leaving behind only a thin film, an appropriate concentration of the solution and solvent is important in the spin casting process.

Most of the solution is wasted during this process as the applied solution is spun off the edges of the substrate while spinning until the desired thickness of the film is achieved. Repeating the spin coating process one or several times, we can create a ~ 1–100 nm thick GO film on the substrate. The resulting films were sufficiently thin to be transparent over the relevant range of wavelengths however the close-assembly of GO is still a big challenging task yet to be performed.

By functionalization of GO [155], it is possible to assemble GO sheets and bring them closer to each other within a specific range of area. However, rotational forces and surface tensions that are present on the surface complicate the non-uniformity created by this process.

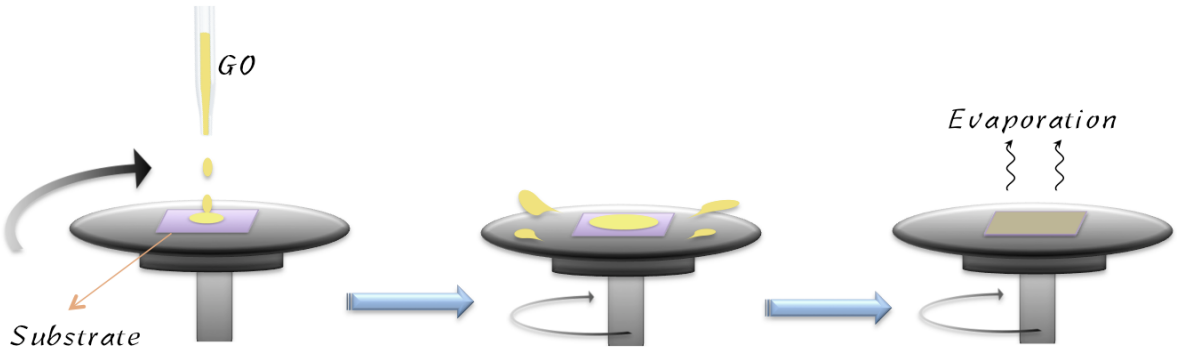

Spin Coating Process

Positives:

- Good Uniformity/reproducibility
- Thickness of the film can be controlled

Negatives:

- Wastage of the sample
- No large area coverage
- Film dries very fast, less time for molecular ordering

1.5.4 & 1.5.5 Vacuum Filtration and Spray Coating Technique

Dikin et al have reported the preparation and characterization of GO paper, a freestanding carbon-based membrane material made by flow-directed assembly of individual GO sheets [158]. This new material outperforms many other paper-like materials in stiffness and strength. Its combination of macroscopic flexibility and stiffness is a result of a unique interlocking-tile arrangement of the nanoscale GO sheets.

However, spraying method can be used to obtain graphene sheets of any desired coverage density with great uniformity and nearly 100% yield means no wastage of the sample as in the case spin coating process. Since the graphene-like sheets are sprayed at 150 °C, this process can be scaled to deposit sheets onto a number of substrates, of any size, and even onto pre-patterned electrodes, thus minimizing the need for characterization while improving throughput [157]. Unlike current synthesis that uses SiC as a starting material, high temperatures (i.e., 1100 °C or greater) are not required. Additionally, spray-coating method is quick, takes only a few hours to yield sheets. This marks a significant advantage over current mechanical methods that have a very low yield of randomly distributed individual graphene sheets, requiring a period of at least a week to search for a suitable graphene specimen.

Although, *spray coating* and *vacuum filtration* techniques may sound good if we are concerned with the simplicity of process, high yield etc., however, it is almost impossible to achieve monolayer thick GO film, which is the foremost concern in nanoelectronics as well as biomedical science. Nonetheless, these techniques could be highly useful for making GO based composite materials where the thickness of GO is not an issue.

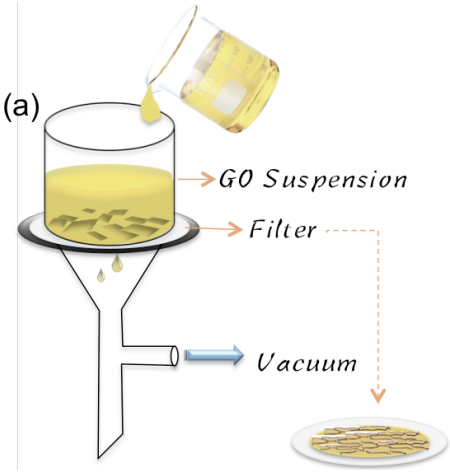

(a) Vacuum Filtration Process

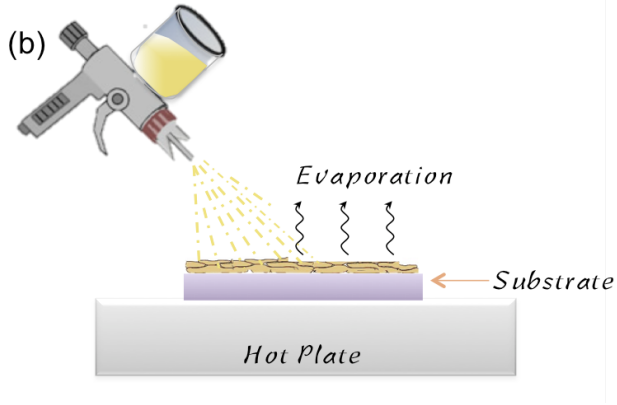

(b) Spray Coating

Positives:

- Large area coverage
- Independent of substrate topology

Negatives:

- Film roughness is high
- Reliable for micrometer thick films

1.5.6 Electrophoretic Deposition Technique.

One very promising technique being developed for the deposition of charged nanomaterials is electrophoretic deposition (EPD). The technique allows the application of coatings, thin and thick films, the shaping of bulk objects, and the

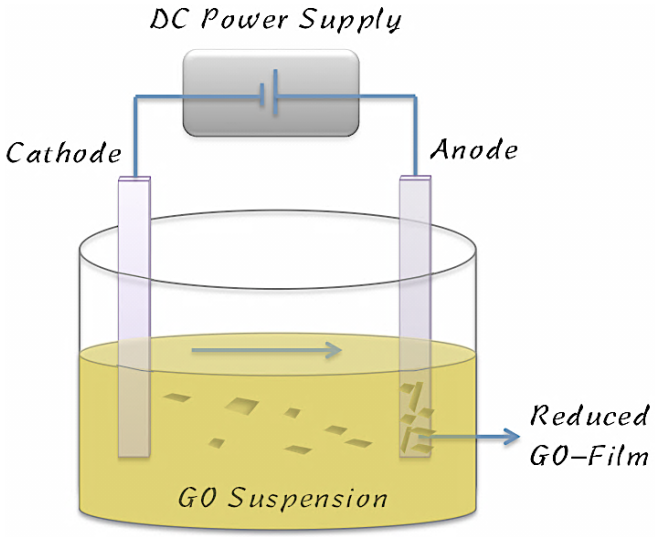

Electrophoretic Deposition Technique

infiltration of porous substrates, fibrous bodies and textile structures with metallic, polymeric or ceramic particles. Generally, EPD is achieved via the motion of charged particles, dispersed in a suitable solvent, towards an electrode under an applied electric field. Deposition on the electrode occurs via particle coagulation. Electrophoretic motion of charged particles during EPD results in the accumulation of particles and the formation of a homogeneous and rigid deposit at the relevant (deposition) electrode. Compared with other processing methods, EPD offers advantages of low cost, process simplicity, microstructural homogeneity, and deposition on complex shaped substrates, including the potential to infiltrate porous substrates. All these advantages can be also exploited for forming films and coatings of carbon nanomaterials. An et al have demonstrated a thin film fabrication and simultaneous anodic reduction of deposited GO platelets by EDP [156].

The films composed of overlapped and stacked platelets of GO reduced by an EPD process. The EPD process significantly removed the oxygen functional groups of GO, and the as-deposited GO film showed improved electrical conductivity (1.43×10^{4} S·m^{-1}) over GO papers made by the filtration method (0.53×10^{-3} S·m^{-1}).

Positives:

- Simple technique
- Large area coverage
- High-Yield

Negatives:

- Multilayer film formation
- Non-uniformity

1.5.7 Langmuir-Blodgett Technique.

LB assembly can make ultrathin films with highly ordered microstructures and applicable to a wide range of building blocks from molecules to nanoparticles [162]. For realizing the important applications of graphene in nanoelectronics, LB assembly is a highly reliable technique for fabricating large-area, flat and monolayer thin films.

Cote et al. have demonstrated that the LB technique could be used to prepare a monolayer film of amphiphilic GO sheets with a precisely controlled nanosheet

density [163]. The strong electrostatic repulsion prevented GO sheets from overlapping when compressed at a liquid-air interface, which resulted in an ordered monolayer structure on hydrophilic substrates. The density of a GO sheet can be continuously tuned from dilute, close-packed to over-packed monolayer during compression at different regions of isotherm. LB assembly has also been applied by Li et al. to deposit monolayer films of hydrophobic rGO sheets on various transparent substrates [164]. Repeating this process can achieve uniform multilayer rGO films.

A highly ordered monolayer film of GO modified with a cationic amphiphilic dye (octadecyl ester of rhodamine B) also has been assembled on hydrophilic substrates by the LB technique [165]. The film architecture can be controlled by the pH value and the concentration of GO in the water sub-phase. At pH 10, LB films made from a 50 mg L^{-1} aqueous GO dispersion consisted of well-defined, closely-packed single- or bi-layer GO sheets with few imperfections such as folding back and face-to- face aggregates of GO.

Positives:

- Excellent control over film thickness
- An ideal monolayer can be grown easily
- Homogeneous and highly ordered monolayers can be obtained
- Multilayer structures with varying layer composition can be achieved
- Less amount of sample is required

Negatives:

- Only amphiphilic molecules can be used

Amongst various techniques, spin coating and LB assembly can provide uniform and continuous conductive films on arbitrary substrates. Spin coating of GO requires high concentrations (0.5 – 3 mm/ml) to produce a uniform and continuous film where the density of the GO and the number of spin-coating processes can determine the thickness of the GO [166]. In LB method, GO sheets are floated at air/water interface and methanol or isopropanol is slowly added to the GO solution. When the electro-repulsive force between the carboxyl functional groups on the edges of the GO sheets overcomes the electro-attractive force between the functional groups on the GO surface, the monolayer is floated at the air-water interface. These sheets can then be deposited on substrates by lifting them from solution. The number of monolayers can easily be controlled by the

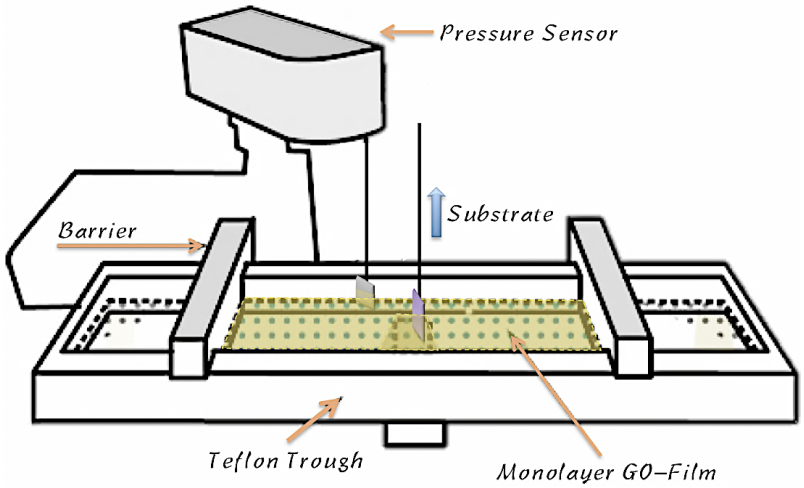

Langmuir-Blodgett Technique

number of repeated deposition cycles.

1.6 General Routes Towards Patterning of GO

Graphene-based nanostructures are considered as promising alternatives to silicon-based electronic devices. The 2D patterned nanostructures, such as 2D ordered nanostructure arrays, surface-patterned nanostructures, and free-standing 2D patterned films, have attracted intensive interest because they exhibit unique pattern-dependent properties and show promising applications in a variety of technologically important areas including photonics, electronics, optoelectronic devices, biological and chemical sensing, surface wetting, and energy conversion. Despite the exciting developments in the controllable fabrication, assembly, and applications of 2D patterned films, many challenges still remain ahead such as facile and reproducible fabrication of defect-free patterns over a large area. It is highly desirable to develop effective patterning techniques for the high-throughput and low-cost fabrication of large-area 2D patterned nanostructures with adjustable structural parameters. Up to now, many processing routes for self-assembly and patterning graphene at micro- and nanoscale have been developed which will be briefly discussed in the upcoming subsections, including,

- Electron Beam Lithography
- Photolithography
- Soft Transfer Printing
- Spin Coating
- Direct Laser Pattering
- Masked Laser Patterning
- Ink-jet Printing

1.6.1 Electron Beam Lithography and Photolithography

There are number of research reports available based on lithographical methods to create graphene nanostructures with pre-designed patterns. Lithographical methods can be used to create graphene nanoribbons (GNRs), with width down to ~ 20 nm, a roughness on the order of a few nanometers [167, 168]. The method employs conventional EBL negative resist to form a protective pattern on graphene, which is subsequently exposed to O_2-plasma. The unprotected portion of graphene is then chemically removed upon the exposure of reactive plasma and carried into the vapor phase. The pattern on the mask (and the e-beam resist) then is ''printed'' onto graphene [167, 168]. Liu et al [169] have employed lithographic patterned graphene as transparent electrodes for single crystalline nanoribbon organic field effect transistors (OFETs) (**Figure 21**). The resolution of EBL depends mainly on the electron beam size and on the scattering and propagation of electrons in the resist material. However, considerable challenges exist in the lithographical patterning of graphene because of its thinness and the sensitivity of its electrical properties to contamination by residual photoresists.

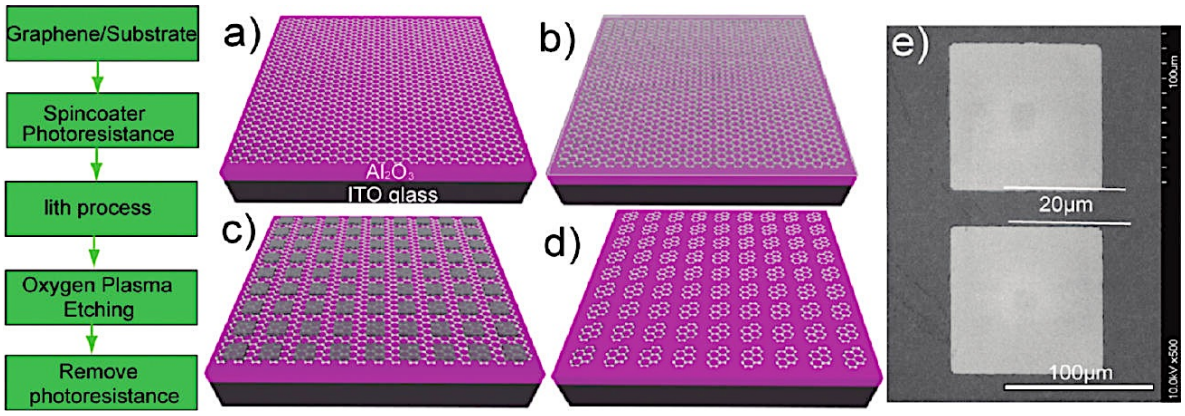

Figure 21. Schematic of the patterned graphene electrode preparation process: (a) graphene is transferred on the Al_2O_3/ITO substrate; (b) spin-coater photoresist on the substrate; (c) UV exposes to form the pattern; (d) after the oxygen plasma etching, the photoresist was removed and the graphene electrode pattern was preserved on the substrate; (e) SEM image of the graphene electrodes. *Reproduced by the permission of The American Physical Society, Ref. 169.*

1.6.2 Soft Transfer Printing

Although mask lithography is suitable for large-scale fabrication of a variety of patterns; it is limited by under-etching and contamination from the contacting masks. The edges generated by etching through shadow or resist masks can produce disordered edges that affect the properties of graphene ribbons.

Matthew et al have demonstrated a soft contact transfer printing method well-suited for the generation of graphene pattern. Graphene-coated glass substrates was contacted with a patterned poly(dimethylsiloxane) (PDMS) stamp, i.e. "inking" the stamp (**Figure 22(a) and 22(b)**) [170]. The inked stamp is contacted with a Si/SiO_2 substrate. As the binding energy of PDMS for graphene is weaker than the substrate interface, graphene is readily transferred from the PDMS to Si/SiO_2 substrates at room temperature (**Figure 22 (c)**). The stamp is finally peeled rom the substrate, leaving behind the rectangular pattern of graphene (**Figure 22 (d)**).

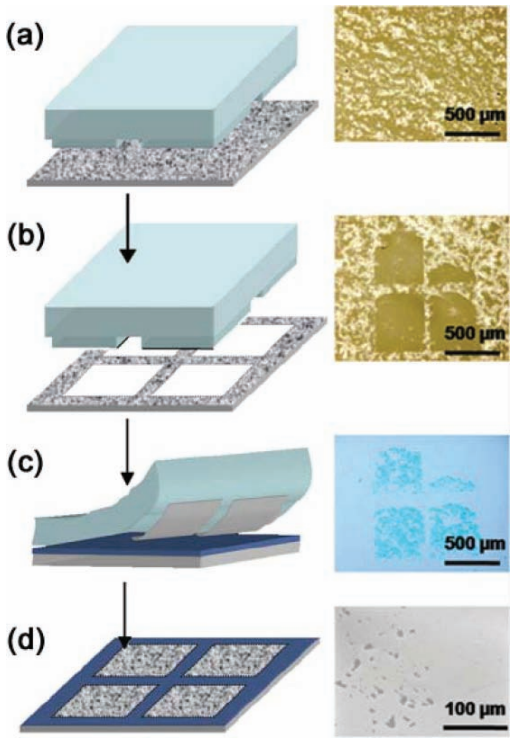

Figure 22. Diagram (left) and optical microscope images (right) depicting the PDMS transfer process. It begins by (a) depositing materials on a glass substrate and (b) carefully "inking" the pre-patterned PDMS stamp. c) The inked stamp contacts with a heated Si/SiO_2 substrate and (d) peeled away to reveal deposited materials. *Reproduced by the permission of WILEY-VCH Verlag GmbH & Co. KGaA, Weinheim, Ref. 170.*

Further, Liang et al. exploited PDMS stamp- based cutting and exfoliation to transfer-print graphene features precisely onto a substrate [171]. The transfer mechanism is based on the different strengths of non-covalent adhesion at the pre-patterned stamp-graphene and graphene-substrate inter- faces. A stamp with protrusions was pressed onto the graphite substrate. Since the bonding between the stamp and graphene is stronger than between the graphene layers, the stamp cuts and attaches to a layer of graphene, the separation of the stamp from the graphite exfoliates the graphene sheet. The isolated graphene can be transferred from the stamp onto the channel region of the device with potential nanoscale accuracy.

1.6.3 Molecular Template and Spin Coating Method

Reduction of GO through various means such as local thermal reduction [172, 173], photochemical reduction [174] and electrochemical reduction [175] has also been shown to be a viable approach to produce patterned graphene with great tunability. Wei et al has demonstrated the placement of single layer GO as well as graphene and using molecular template to transfer and immobilize single-layer graphene onto predefined areas of substrate surfaces (**Figure 23**) [176]. The distribution of the GO sheets depended on the surface functionalization, background passivation, pH, and deposition time. Electrostatic attraction guides the templating of the GO sheets and, consequently, templating could be modulated by adjusting the pH of the deposition solution.

Guo et al have achieved effective patterning of rGO by using a wettability modulation and low cost spin-coating technique [177]. For the dewetting surfaces, the solution is easily spun out of the substrate during the spin-coating process, while a solution film was formed on the wetting surface at the start-up spin-coating speed. In the following fast spin-coating process, the GOs in fastened solution are inclined to the wetting surface due to the tangential force and are deposited on the wetting region with the solvent drying resulting in patterning of GO on the predefined wetting surfaces. Since the solution wettability as well as the GO concentration affects the solution fastened on the substrate and GOs' number per volume, respectively, they influence the GOs' number on the substrates.

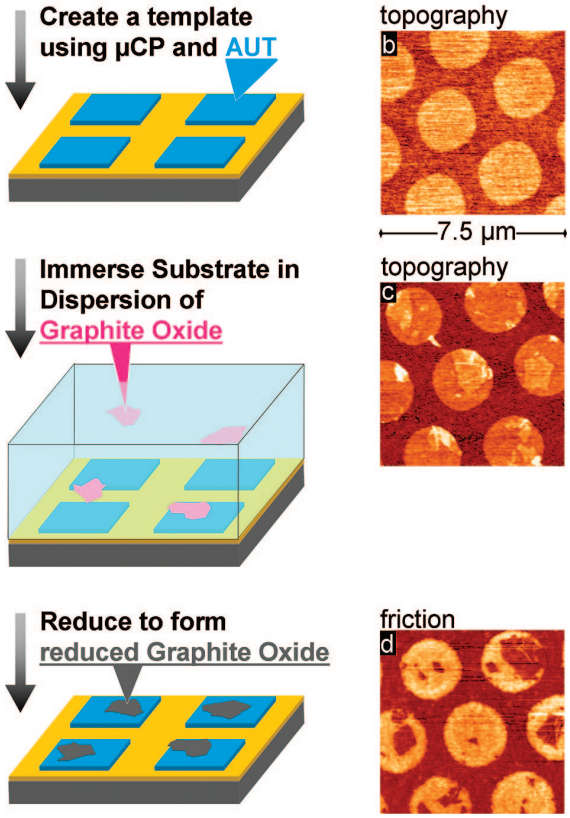

Figure 23. (a) A scheme of the templating process that shows the formation of the amino-terminated template on mica-peeled gold, followed by immersion in a dispersion of graphite oxide to the reduction of the captured GO to form reduced graphite oxide. **(b)** AFM topograph of the AUT template before exposure. **(c)** AFM topograph of an AUT template exposed to the GO dispersion for 5s. The corresponding friction image may be found in the center of Figure 2a. Note that sheets that span an edge appear to be folded back onto the template. **(d)** Friction image of the templated GO sheets reduced by hydrazine for 17 h. Note that unreduced GO also has friction lower than the AUT template. *Reproduced by the permission of American Chemical Society, Ref. 176.*

1.6.4 Direct and Masked Laser Patterning

Resist-based lithography is a convenient way to define graphene features and patterns for devices but suffers from multiple issues for the high throughput processing of graphene devices due to surface contamination issues. The maskless, contact-free, direct "writing" of patterns of graphene using laser or heium ion beam allows simultaneous lateral and vertical scaling. Laser scribing was recently applied by Strong et al. [178], which can directly pattern circuits and complex design in a single step process without masks, templates, and post-

processing. It was shown to be an efficient way to deoxygenate the graphite oxide film and produce highly reduced laser scribed graphene with significantly enhanced conductivity with sub-20 nm feature sizes. Zhang et al. directly imprinted graphene microcircuits on GO through direct femtosecond laser reduction with a designed complex pattern in high resolution (**Figure 24**) [179].

Zhou et al have employed a focused laser beam technique to construct an extended area of micropatterned GO and reduced GO multilayers on quartz substrates in a fast and controlled manner where no pre-patterned substrate is required [180]. The multilayer GO film was placed in the focused laser-beam system. When the focused laser beam was incident on the film, the irradiated area absorbed the laser energy, and the energy was rapidly converted into local heat. The intense heating raised the temperature of the irradiated area above 500 °C in air and resulted in localized oxidative burning of GO to volatile gases such as CO or CO_2. By moving the computer-controlled sample stage in a programmable step with respect to the focused laser beam, patterns with tunable width and length could be directly written.

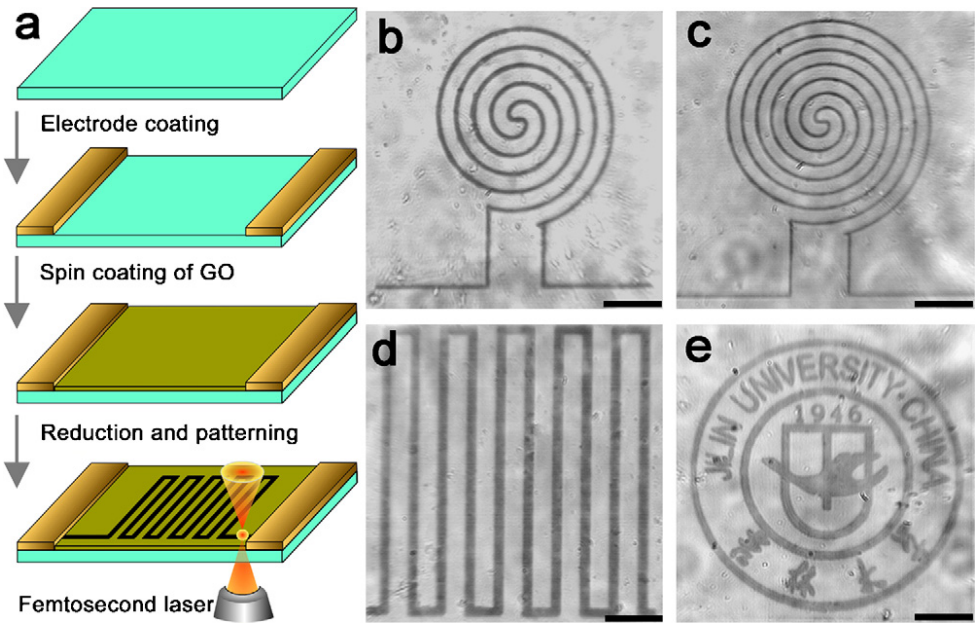

Figure 24. Preparative scheme and optical microscopy images of reduced and patterned GO films. (a) Illustration of preparative procedure of GO microcircuit; optical microscopy images of a curvilinear microcircuit (MC) (b) MC-1, (c) MC-2, comb-like microcircuit (d) MC-3, and (e) the badge of Jilin University. Scale bars, 10 μm. *Reproduced by the permission of American Chemical Society, Ref. 179.*

1.6.5 Ink-jet Printing

Zhang et al have addressed an ink-jet printing high resolution, large area graphene patterns by coffee ring lithography technique by inkjet etching a polymer mask and then delaminating the mask layer in water. This method is quite similar to the traditional lift-off process, except that the mask is patterned by direct inkjet printing of a pure solvent. The researchers have achieved electrode pairs of 1-2 micrometer channel length by taking an advantage of the coffee-ring effect (**Figure 25**) [181]. A uniform polyacrylonitrile (PAN) film was spin-coated onto the silica substrate as a mask layer; 2) pure *N*,*N*-dimethylformamide (DMF) was inkjet printed onto the substrate to dissolve the PAN film; 3) a silica-PAN pattern was formed by inkjet etching; 4) GO was spin-coated onto the silica-PAN pattern; 5) a polystyrene (PS) film was spin-coated to serve as a strengthening layer; and 6) the PS layer was lifted off in water. A PAN film was readily peeled off a silica substrate in water and was removed along with the PS strengthening layer, whereas GO remained on the substrate because of its large adhesion to silica. Thus, PAN masks can successfully produce a GO pattern on the substrate through a lift-off process.

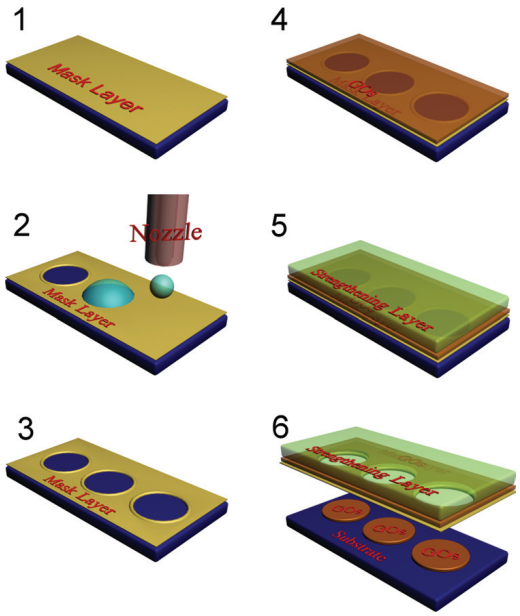

Figure 25. Fabrication of the PAN mask layer by spin coating (1). Inkjet printing of pure solvent to dissolve the mask layer drop-on-demand (2). The substrate with patterned mask layer on top (3). Deposition of graphene oxide layer (4). Fabrication of the PS strengthening layer (5). Peeling off the mask layer and the strengthening layer (6). *Reproduced by the permission of Elsevier, Ref. 181.*

1.7 Motivation Behind this Thesis Work

The realization of nanoscale electronics and bioengineering are a subject of great priority for industrial technology. In the above section, it has been discussed that one of the important aspects of nanotechnology is the formation of monolayer patterned thin films of nanomaterials that can be realized either by assembling the nanoparticles or synthesizing them in 2D confined space. Graphene, a monolayerof sp^2-bonded carbon atoms is the basic building block for all graphitic materials, is particularly an attractive candidate for such applications. Intensive study has been devoted to assemble GO in a 2D manner. Among all the techniques available for its thin film formation, assembly of GO via LB technique has proven to be a straightforward and highly reproducible method for production of uniform 2D films at air-water interface for a wide range of applications [182].

From the reviewed literature, it was also recognized that the size of GO plays an important role in modulating its electronic and chemical properties that makes it an ideal building block for the next generation of microscale as well as nanoscale electronic devices. A significant progress has been made in the area of its synthesis and applications [183]. However, from the industrial point of view, a grand challenge still exists for its large area synthesis, its self-assembly, selective placement and patterning for diverse deployment of green technology, for applications in electronics, photonics, optoelectronic devices, biological and chemical sensing, energy conversation etc.

Progress in this direction has been made by many researchers using various techniques including EBL, UVL, SPL, block copolymer lithography, soft transfer printing, masked laser patterning, direct laser patterning, combination of wettability modulation and spin coating, ink-jet printing, etc. [184]. The complex patterned structures can be formed using the current lithography and metal evaporation deposition techniques. However, this technique involves photoresists, which is undesirable due to the presence of residual polymers that may contaminate the graphene surface and interfere with subsequent metallization steps or even may denature or deactivate the biomolecules. Apart from that, these processes are time consuming; involve highly complicated processes, expensive equipment and low throughput. However, surprisingly, the use of air-water interface for achieving successful selective placement and patterning of large area 2D patterned graphene and related derivatives with controllable dimensions remain

largely unexplored.

Besides the active role played by the air-water interface in the assembly of monolayer GO sheets, an exciting prospect will be to design experiments wherein the air-water interface can directly be employed for the formation of desired geometric patterns on suitable substrates. The key motivation behind this study is to apply this technique for site-specific disposition of GO to fabricate electronic device array and to enhance the cellular growth in a specific area for tissue engineering and neural generation applications.

References

1. R.P. Feynman. *Eng. Sci.* 23, 22-36 (**1960**). http://www.zyvex.com/nanotech/feynman.html
2. J. M. Thomas. *Pure Appl. Chem.*, **1988**, *60*, 1517.
3. P. Iqbal, J. A. Preece, and P. M. Mendes. Supramolecular Chemistry: From Molecules to Nanomaterials. **2012**.
4. (a) G. M. Whitesides, Small, **2005**, *1*, 172; (b) J. H. Fendler, F. C. Meldrum. *Adv. Mater.* **1995**, *7*, 607; (c) G. Schmid. *Chem. Rev*. **1992**, *92*, 1709.
5. A. Henglein. *J. Phys. Chem.* **1993**, *97*, 5457.
6. J. N. Tiwari, R. N. Tiwari, K. S. Kim. Progress in Materials Science **2012**, *57,* 724.
7. V. V. Pokropivny, V. V. Skorokhod. *Mater Sci Eng C* **2007**, *27*, 990.
8. K. S. Novoselov, A. K. Geim, S. V. Morozov, D. Jiang, Y. Zhang, S. V. Dubonos, I. V. Grigorieva and A. A. Firsov. *Science*, **2004**, *306*, 666.
9. A. K. Geim and K. S. Novoselov. Nat. Mater., **2007**, *6*, 183.
10. a) X. Jia, J. Campos-Delgado, M. Terrones, V. Meunier and M. S. Dresselhaus, *Nanoscale*, **2011**, *3*, 86; b) C. N. R. Rao, A. K. Sood, K. S. Subrahmanyam and A. Govindaraj. *Angew. Chem., Int. Ed.*, **2009**, *48*, 7752.
11. C. Lee, X. Wei, J. W. Kysar and J. Hone. *Science*, **2008**, *321*, 385.
12. R. Khare, S. L. Mielke, J. T. Paci, S. Zhang, R. Ballarini, G. C. Schatz and T. Belytschko, *Phys. Rev. B: Condens. Matter Mater. Phys.,* **2007**, *75*, 075412.
13. F. Liu, P. M. Ming and J. Li. *Phys. Rev. B: Condens. Matter Mater. Phys.,* **2007**, *76*, 064120.
14. J. Q. Liu, Z. Y. Yin, X. H. Cao, A. Lin, L. Xie, Q. Fan, F. Boey, H. Zhang and W. Huang, *ACS Nano*, **2010**, *4*, 3987.

15. a) J. Q. Liu, Z. Y. Lin, T. J. Liu, Z. Y. Yin, X. Zhou, S. Chen, L. Xie, F. Boey, H. Zhang and W. Huang, *Small*, **2010**, *6*, 1536; b) D. R. Cooper, B. D'Anjou, N. Ghattamaneni, B. Harack, M. Hilke, A. Horth, N. Majlis, M. Massicotte, L. Vandsburger, E. Whiteway, V. Yu. *ISRN Condensed Matter Physics*, **2012**, *Article ID 501686*, 56 pages; c) P. Recher and B. Trauzettel. *Viewpoint: A defect controls transport in graphene*. DOI: 10.1103/Physics.4.25
16. K. S. Novoselov, A. K. Geim, S. V. Morozov, D. Jiang, M. I. Katsnelson, I. V. Grigorieva, S. V. Dubonos and A. A. Firsov. *Nature*, **2005**, *438*, 197.
17. Y. B. Zhang, Y. W. Tan, H. L. Stormer and P. Kim. *Nature*, **2005**, *438*, 201.
18. D. A. Abanin and L. S. Levitov, *Science*, **2007**, *317*, 641.
19. J. R. Williams, L. DiCarlo and C. M. Marcus. *Science*, **2007**, *317*, 638.
20. P. R. Wallace. *Phys. Rev.*, **1947**, *71*, 622.
21. J. C. Meyer, A. K. Geim, M. I. Katsnelson, K. S. Novoselov, T. J. Booth and S. Roth. *Nature*, **2007**, *446*, 60.
22. X. Du, I. Skachko, A. Barker and E. Y. Andrei. *Nat. Nanotechnol.*, **2008**, *3*, 491.
23. K. S. Novoselov, Z. Jiang, Y. Zhang, S. V. Morozov, H. L. Stormer, U. Zeitler, J. C. Maan, G. S. Boebinger, P. Kim and A. K. Geim, *Science*, **2007**, *315*, 1379.
24. F. Wang, Y. B. Zhang, C. S. Tian, C. Girit, A. Zettl, M. Crommie and Y. R. Shen. *Science*, **2008**, *320*, 206.
25. F. N. Xia, T. Mueller, Y. M. Lin, A. Valdes-Garcia and P. Avouris. *Nat. Nanotechnol.,* **2009**, *4*, 839.
26. K. S. Novoselov, A. K. Geim, S. V. Morozov, D. Jiang, M. I. Katsnelson, I. V. Grigorieva, S. V. Dubonos, and A. A. Firsov. *Nature*, **2005**, *438*, 197.
27. A. H. Castro Neto, F. Guinea, N. M. R. Peres, K. S. Novoselov, and A. K. Geim. *Rev. Mod. Physics*, **2009**, *81*, 109.
28. S. V. Morozov, K. S. Novoselov, M. I. Katsnelson, F. Schedin, D. C. Elias, J. A. Jaszczak, and A. K. Geim. *Phys. Rev. Lett.*, **2008**, *100*, 016602.
29. Y. -W. Tan, Y. Zhang, K. Bolotin, Y. Zhao, S. Adam, E. H. Hwang, S. Das Sarma, H. L. Stormer, and P. Kim. *Phys. Rev. Lett.,* **2007**, *99*, 246803.
30. W. Cai, Y. Zhu, X. Li, R. D. Piner, R. S. Ruoff, *Appl. Phys. Lett.* **2009**, *95*, 123115.
31. X. Li, Y. Zhu, W. Cai, M. Borysiak, B. Han, D. Chen, R. D. Piner, L. Colombo, R. S. Ruoff, *Nano Lett.* **2009**, *9*, 4359.

32. S. Chen, Q. Wu, C. Mishra, J. Kang, H. Zhang, K. Cho, Weiwei Cai, A. A. Balandin, R. S. Ruoff. *Nature Materials*, **2012**, *11*, 203.
33. J. S. Bunch, S. S. Verbridge, J. S. Alden, A. M. van der Zande, J. M. Parpia, H. G. Craighead, P. L. McEuen. *Nano Lett.*, 2008, *8 (8)*, 2458.
34. M. T. Ong, E. J. Reed. *ACS Nano*, 2012, *6 (2),* 1387.
35. C. Chung, Y-K Kim, D. Shin, S-R Ryoo, B. H. Hong, and Dal-Hee Min. *Acc. Chem. Res.*, 2013, *46 (10)*, 2211.
36. J. Zhang, F. Zhang, H. Yang, X. Huang, H. Liu, J. Zhang, and S. Guo. *Langmuir* **2010,** *26,* 6083.
37. a) D. R. Dreyer, R. S. Ruoff and C. W. Bielawski. *Angew. Chem., Int. Ed.*, **2010**, *49*, 9336; b) K. P. Loh, Q. Bao, P. K. Ang and J. Yang. *J. Mater. Chem.*, **2010**, *20*, 2277.
38. X. Huang, X. Qi, F. Boey and H. Zhang. *Chem. Soc. Rev.* **2012,** *41,* 666.
39. M. Terrones, O. Martín, M. González, , J.Pozuelo, B. Serrano, J. C. Cabanelas, S. M. Vega-Díaz, and J. Baselga. *Adv. Mater.* **2011**, *23*, 5302.
40. X. Y. Qi, K. Y. Pu, H. Li, X. Z. Zhou, S. X. Wu, Q. L. Fan, B. Liu, F. Boey, W. Huang and H. Zhang. *Angew. Chem., Int. Ed.,* **2010**, *49*, 9426.
41. H. G. Sudibya, Q. Y. He, H. Zhang and P. Chen. *ACS Nano*, **2011**, *5*, 1990.
42. Q. Y. He, H. G. Sudibya, Z. Y. Yin, S. X. Wu, H. Li, F. Boey, W. Huang, P. Chen and H. Zhang. *ACS Nano*, **2010**, *4*, 3201.
43. S. X. Wu, Z. Y. Yin, Q. Y. He, G. Lu, X. Z. Zhou and H. Zhang. *J. Mater. Chem.,* **2011**, *21*, 3467.
44. Y. Wang, Z. Shi, Y. Huang, Y. Ma, C. Wang, M. Chen and Y. Chen, *J. Phys. Chem. C,* **2009**, *113*, 13103.
45. Z. Y. Yin, S. X. Wu, X. Z. Zhou, X. Huang, Q. C. Zhang, F. Boey and H. Zhang, *Small*, **2010**, *6*, 307.
46. L. Zhang, X. Li, Y. Huang, Y. Ma, X. Wan and Y. Chen, *Carbon,* **2010**, *48*, 2367.
47. X. Z. Zhou, X. Huang, X. Y. Qi, S. X. Wu, C. Xue, F. Boey, Q. Y. Yan, P. Chen and H. Zhang, *J. Phys. Chem. C*, **2009**, *113*, 10842.
48. X. Y. Qi, K. Y. Pu, X. Z. Zhou, H. Li, B. Liu, F. Boey, W. Huang and H. Zhang. *Small*, **2010**, 6, 663.
49. Z. Y. Yin, S. Y. Sun, T. Salim, S. X. Wu, X. Huang, Q. Y. He, Y. M. Lam and H. Zhang. *ACS Nano*, **2010**, *4*, 5263.

50. S. X. Wu, Z. Y. Yin, Q. Y. He, X. Huang, X. Z. Zhouand, H. Zhang. *J. Phys. Chem. C*, **2010**, *114*, 11816.
51. J. B. Liu, S. H. Fu, B. Yuan, Y. L. Liand, Z. X. Deng, *J. Am. Chem. Soc.*, **2010**, *132*, 7279.
52. X. Fan, W. Peng, Y. Li, X. Li, S. Wang, G. Zhang and F. Zhang. *Adv. Mater.*, **2008**, *20*, 4490.
53. H. Bai, C. Li and G. Shi. *Adv. Mater.*, **2011**, *23*, 1089.
54. X. Huang, Z. Yin, S. Wu, X. Qi, Q. He, Q. Zhang, Q. Yan, F. Boey and H. Zhang, *Small*, **2011**, *7*, 1876.
55. J. R. Potts, D. R. Dreyer, C. W. Bielawshi and R. S. Ruoff. *Polymer,* **2011**, *52*, 5.
56. R. S. Edwards and K. S. Coleman. **Nanoscale**, **2013**, **5**, 38.
57. R. O. Brennan, *J. Chem. Phys.,* **1952**, 20, 40.
58. http://ec.europa.eu/enterprise/policies/raw materials/critical/index_en.htm.
59. M. Inagaki, *Elsevier Science, Oxford*, **2000**, 30.
60. K. S. Novoselov and A. H. C. Neto. *Phys. Scr. T146*, **2012**, 014006 (6pp)
61. G. Wang, B. Wang, J. Park, Y. Wang, B. Sun and J. Yao. *Carbon*, **2009**, *47*, 3242.
62. C.-Y. Su, A.-Y. Lu, Y. Xu, F.-R. Chen, A. N. Khlobystov and L.-J. Li. *ACS Nano*, **2011**, *5*, 2332.
63. J. M. Englert, J. R ohrl, C. D. Schmidt, R. Graupner, M. Hundhausen, F. Hauke and A. Hirsch. *Adv. Mater.*, **2009**, *21*, 4265.
64. D. A. C. Brownson, J. P. Metters, D. K. Kampouris and C. E. Banks, Electroanalysis, 2011, 23, 894–.
65. J. Wang, K. K. Manga, Q. Bao and K. P. Loh. *J. Am. Chem. Soc.,* **2011**, *133*, 8888.
66. H. Huang, Y. Xia, X. Tao, J. Du, J. Fang, Y. Gan and W. Zhang, *J. Mater. Chem.*, **2012**, *22*, 10452.
67. K. S. Suslick and G. J. Price. *Annu. Rev. Mater. Sci.*, **1999**, *29*, 295.
68. C. Vall es, C. Drummond, H. Saadaoui, C. A. Furtado, M. He, O. Roubeau, L. Ortolani, M. Monthioux and A. P enicaud, *J. Am. Chem. Soc.*, **2008**, *130*, 15802.
69. X. Li, G. Zhang, X. Bai, X. Sun, X. Wang, E. Wang and H. Dai. *Nat. Nanotechnol.,* **2008**, *3*, 538.

70. L. M. Viculis, J. J. Mack, O. M. Mayer, H. T. Hahn and R. B. Kaner. *J. Mater. Chem.*, **2005**, *15*, 974.
71. J. W. Aylesworth, US Pat., **1916**, *1191383*.
72. D. D. L. Chung. *J. Mater. Sci.,* **1987**, *22*, 4190.
73. T. Wei, Z. Fan, G. Luo, C. Zheng and D. Xie. *Carbon*, **2009**, *47*, 337.
74. S. Malik, A. Vijayaraghavan, R. Erni, K. Ariga, I. Khalakhan and J. P. Hill. *Nanoscale*, **2010**, *2*, 2139–2143.
75. W. Gu, W. Zhang, X. Li, H. Zhu, J. Wei, Z. Li, Q. Shu, C. Wang, K. Wang, W. Shen, F. Kang and D. Wu. *J. Mater. Chem.*, **2009**, *19*, 3367.
76. S. R. Dhakate, N. Chauhan, S. Sharma, J. Tawale, S. Singh, P. D. Sahare and R. B. Mathur. *Carbon*, **2011**, *49*, 1946.
77. W. Fu, J. Kiggans, S. H. Overbury, V. Schwartz and C. Liang. *Chem. Commun.*, **2011**, *47*, 5265.
78. A. Safavi, M. Tohidi, F. A. Mahyari and H. Shahbaazi. *J. Mater. Chem.,* **2012**, *22*, 3825.
79. P. Blake, P. D. Brimicombe, R. R. Nair, T. J. Booth, D. Jiang, F. Schedin, L. A. Ponomarenko, S. V. Morozov, H. F. Gleeson, E. W. Hill, A. K. Geim and K. S. Novoselov. *Nano Lett.*, **2008**, *8*, 1704.
80. Y. Hernandez, V. Nicolosi, M. Lotya, F. M. Blighe, Z. Sun, S. De, I. T. McGovern, B. Holland, M. Byrne, Y. K. Gun'ko, J. J. Boland, P. Niraj, G. Duesberg, S. Krishnamurthy, R. Goodhue, J. Hutchison, V. Scardaci, A. C. Ferrari and J. N. Coleman. *Nat. Nanotechnol.*, **2008**, 3, 563.
81. Y. Hernandez, M. Lotya, D. Rickard, S. D. Bergin and J. N. Coleman. *Langmuir*, **2009**, *26*, 3208.
82. U. Khan, A. O'Neill, M. Lotya, S. De and J. N. Coleman. *Small*, **2010**, *6*, 864.
83. U. Khan, H. Porwal, A. O'Neill, K. Nawaz, P. May and J. N. Coleman. **Langmuir, 2011**, *27*, 9077.
84. A. Ciesielski and P. Samor`ı. **Chem. Soc. Rev.**, **2014**, **43**, 381.
85. A. O'Neill, U. Khan, P. N. Nirmalraj, J. Boland and J. N. Coleman. *J. Phys. Chem. C*, **2011**, *115*, 5422.
86. M. Lotya, Y. Hernandez, P. J. King, R. J. Smith, V. Nicolosi, L. S. Karlsson, F. M. Blighe, S. De, Z. Wang, I. T. McGovern, G. S. Duesberg and J. N. Coleman, *J. Am. Chem. Soc.*, **2009**, *131*, 3611.
87. M. Lotya, P. J. King, U. Khan, S. De and J. N. Coleman. *ACS Nano*, **2010**, *4*, 3155.

88. J. S. Ronan, L. Mustafa and N. C. Jonathan. *New J. Phys.*, **2010**, *12*, 125008.
89. H. L. Poh, F. Sanek, A. Ambrosi, G. Zhao, Z.Sofer and M. Pumera. *Nanoscale*, **2012**, *4*, 3515.
90. D. C. Marcano, D. V. Kosynkin, J. M. Berlin, A. Sinitskii, Z. Sun, A. Slesarev, L. B. Alemany, W. Lu and J. M. Tour. *ACS Nano*, **2010**, *4*, 4806.
91. N. I. Kovtyukhova, P. J. Ollivier, B. R. Martin, T. E. Mallouk, S. A. Chizhik, E. V. Buzaneva and A. D. Gorchinskiy, *Chem. Mater.*, **1999**, *11*, 771.
92. G. Shao, Y. Lu, F. Wu, C. Yang, F. Zeng and Q. Wu. *J. Mater. Sci.*, **2012**, *47*, 4400.
93. S. Lee, J. Oh, R. S. Ruoff and S. Park. *Carbon*, **2012**, *50*, 1442.
94. D. R. Dreyer, S. Park, C. W. Bielawski and R. S. Ruoff. *Chem. Soc. Rev.*, **2010**, *39*, 228.
95. A. Lerf, H. He, M. Forster and J. Klinowski. *J. Phys. Chem. B*, **1998**, *102*, 4477.
96. H. He, J. Klinowski, M. Forster and A. Lerf. *Chem. Phys. Lett.,* **1998**, *287*, 53.
97. A. Buchsteiner, A. Lerf and J. Pieper. *J. Phys. Chem. B*, **2006**, *110*, 22328.
98. S. Pei and H.-M. Cheng. *Carbon*, **2012**, *50*, 3210.
99. Chun Kiang Chua and Martin Pumera. *Chem.Soc.Rev.,* **2014**, *43*, 291.
100. S. Farhat and C. D. Scott. *J. Nanosci. Nanotechnol.*, **2006**, *6*, 1189.
101. K. S. Subrahmanyam, L. S. Panchakarla, A. Govindaraj and C. N. R. Rao. *J. Phys. Chem. C*, **2009**, *113*, 4257.
102. Y. Chen, H. Zhao, L. Sheng, L. Yu, K. An, J. Xu, Y. Ando and X. Zhao. *Chem. Phys. Lett.,* **2012**, *538*, 72.
103. B. Shen, J. Ding, X. Yan, W. Feng, J. Li and Q. Xue. *Appl. Surf. Sci.*, **2012**, *258*, 4523.
104. M. Terrones. *Nature,* **2009**, *458*, 845-846.
105. D. V. Kosynkin, A. L. Higginbotham, A. Sinitskii,J. R. Lomeda, A. Dimiev, B. K. Price and J. M. Tour. *Nature*, **2009**, *458*, 872.
106. P. Kumar, L. S. Panchakarla and C. N. R. Rao, *Nanoscale*, **2011**, *3*, 2127.
107. L. Jiao, L. Zhang, X. Wang, G. Diankov and H. Dai. *Nature*, **2009**, *458*, 877.
108. L. Valentini. *Diamond Relat. Mater.,* **2011**, *20*, 445.
109. K. Nakada, M. Fujita, G. Dresselhaus and M. S. Dresselhaus. *Phys. Rev. B: Condens. Matter*, **1996**, *54*, 17954.
110. L. Xie, H. Wang, C. Jin, X. Wang, L. Jiao, K. Suenaga and H. Dai. *J. Am. Chem. Soc.*, **2011**, *133*, 10394.

111. S. Cho, K. Kikuchi and A. Kawasaki. *Carbon*, **2011**, *49*, 3865.
112. Y.-R. Kang, Y.-L. Li and M.-Y. Deng. *J. Mater. Chem.*, **2012**, *22*, 16283.
113. P. Sutter. *Nat. Mater.*, **2009**, *8*, 171.
114. K. V. Emtsev, A. Bostwick, K. Horn, J. Jobst, G. L. Kellogg, L. Ley, J. L. McChesney, T. Ohta, S. A. Reshanov, J. Rohrl, E. Rotenberg, A. K. Schmid, D. Waldmann, H. B. Weber and T. Seyller. *Nat. Mater.,* **2009**, *8*, 203.
115. C. Virojanadara, M. Syvaejarvi, R. Yakimova, L. I. Johansson, A. A. Zakharov and T. Balasubramanian. *Phys. Rev. B: Condens. Matter Mater. Phys.,* **2008**, *78*, 245403.
116. Luxmi, N. Srivastava, R. M. Feenstra and P. J. Fisher. *J. Vac.Sci. Technol.*, B: Microelectron. Nanometer Struct.-Process., S85. Meas., Phenom., **2010**, *28*, C5C1.
117. R. M. Tromp and J. B. Hannon, *Phys. Rev. Lett.*, **2009**, *102*,106104.
118. Q. Huang, X. Chen, J. Liu, W. Wang, G. Wang, W. Wang, R. Yang, Y. Liu and L. Guo, *Chem. Commun.,* **2010**, *46*, 4917.
119. Z.-Y. Juang, C.-Y. Wu, C.-W. Lo, W.-Y. Chen, C.-F. Huang, J.-C. Hwang, F.-R. Chen, K.-C. Leou and C.-H. Tsai. *Carbon*, **2009**, 47, 2026.
120. A. A. Woodworth and C. D. Stinespring. *Carbon*, **2010**, *48*,1999.
121. T. Yoneda, M. Shibuya, K. Mitsuhara, A. Visikovskiy, Y. Hoshino and Y. Kido, *Surf. Sci.*, **2010**, *604*, 1509.
122. C. Y. Kang, L. L. Fan, S. Chen, Z. L. Liu, P. S. Xuand C. W. Zou, *Appl. Phys. Lett.,* **2012**, *100*, 251604.
123. J. D. Caldwell, T. J. Anderson, J. C. Culbertson, G. G. Jernigan, K. D. Hobart, F. J. Kub, M. J. Tadjer, J. L. Tedesco, J. K. Hite, M. A. Mastro, R. L. Myers-Ward, C. R. Eddy, P. M. Campbell and D. K. Gaskill. *ACS Nano*, **2010**, *4*, 1108.
124. S. Unarunotai, Y. Murata, C. E. Chialvo, H.-s. Kim, S. MacLaren, N. Mason, I. Petrov and J. A. Rogers. *Appl. Phys. Lett.,* **2009**, *95*, 202101.
125. F. Varchon, R. Feng, J. Hass, X. Li, B. N. Nguyen, C. Naud, P. Mallet, J. Y. Veuillen, C. Berger, E. H. Conrad and L. Magaud. *Phys. Rev. Lett.*, **2007**, *99*, 126805.
126. V. Y. Aristov, G. Urbanik, K. Kummer, D. V. Vyalikh, O. V. Molodtsova, A. B. Preobrajenski, A. A. Zakharov, C. Hess, T. Haenke, B. Buechner, I. Vobornik, J. Fujii, G. Panaccione, Y. A. Ossipyan and M. Knupfer. *Nano Lett.*, **2010**, *10*, 992.

127. C. Xu, X. Wang and J. Zhu. *J. Phys. Chem. C*, **2008**, *112*,19841.
128. K. Jasuja and V. Berry. *ACS Nano,* **2009**, *3*, 2358.
129. Y. Zhang, L. Zhang and C. Zhou. *Accounts of chemical research,* **2013**, *46(10)*, 2329.
130. S. Liu, J. Wang, J. Zeng, J. Ou, Z. Li, X. Liu and S. Yang. *J. Power Sources*, **2010**, *195*, 4628.
131. Y.-G. Zhou, J.-J. Chen, F.-B. Wang, Z.-H. Sheng and X.-H. Xia. *Chem. Commun.*, **2010**, *46*, 5951.
132. S. Bong, Y.-R. Kim, I. Kim, S. Woo, S. Uhm, J. Lee and H. Kim. *Electrochem. Commun.,* **2010**, *12*, 129.
133. L. Dong, R. R. S. Gari, Z. Li, M. M. Craig and S. Hou. *Carbon*, **2010**, *48*, 781.
134. S. Guo, S. Dong and E. Wang. *ACS Nano*, **2010***, 4*, 547.
135. R. Kou, Y. Shao, D. Wang, M. H. Engelhard, J. H. Kwak, J. Wang, V. V. Viswanathan, C. Wang, Y. Lin, Y. Wang, I. A. Aksay and J. Liu, *Electrochem. Commun.,* **2009**, *11*, 954.
136. Y. Shao, S. Zhang, C. Wang, Z. Nie, J. Liu, Y. Wang and Y. Lin. *J. Power Sources*, **2010**, *195*, 4600.
137. L. Qu, Y. Liu, J.-B. Baek and L. Dai. *ACS Nano*, **2010**, *4*, 1321.
138. E. Katz and I. Willner. *J. Am. Chem. Soc.*, **2003**, *125*, 6803.
139. F. Davis and S. P. J. Higson, *Biosens. Bioelectron.*, **2007**, *22*, 1224.
140. C. Liu, S. Alwarappan, Z. Chen, X. Kong and C.-Z. Li, *Biosens. Bioelectron.,* **2010**, *25*, 1829.
141. W. Zheng, H. Y. Zhao, J. X. Zhang, H. M. Zhou, X. X. Xu, Y. F. Zheng, Y. B. Wang, Y. Cheng and B. Z. Jang, *Electrochem. Commun.*, **2010**, *12*, 869.
142. H. Wang, Q. Hao, X. Yang, L. Lu and X. Wang. *ACS Appl. Mater. Interfaces*, **2010**, *2*, 821.
143. S. R. C. Vivekchand, C. S. Rout, K. S. Subrahmanyam, A. Govindaraj and C. N. R. Rao. *J. Chem. Sci.*, **2008**, *120*, 9.
144. M. D. Stoller, S. Park, Y. Zhu, J. An and R. S. Ruoff. *Nano Lett.*, **2008**, *8*, 3498.
145. W. Lv, D.-M. Tang, Y.-B. He, C.-H. You, Z.-Q. Shi, X.-C. Chen, C.-M. Chen, P.-X. Hou, C. Liu and Q.-H. Yang*. ACS Nano*, **2009**, *3*, 3730.
146. H. Bai, Y. Xu, L. Zhao, C. Li and G. Shi, *Chem. Commun.,* **2009**, 1667.

147. A. V. Murugan, T. Muraliganth and A. Manthiram, *Chem. Mater.,* **2009**, *21*, 5004.
148. K. Zhang, L. L. Zhang, X. S. Zhao and J. Wu. *Chem. Mater.,* **2010**, *22*, 1392.
149. D.-W. Wang, F. Li, J. Zhao, W. Ren, Z.-G. Chen, J. Tan, Z.-S. Wu, I. Gentle, G. Q. Lu and H.-M. Cheng. *ACS Nano*, **2009**, *3*, 1745.
150. Q. Wu, Y. Xu, Z. Yao, A. Liu and G. Shi. *ACS Nano*, **2010**, *4*, 1963.
151. J. Yan, T. Wei, B. Shao, Z. Fan, W. Qian, M. Zhang and F. Wei.*Carbon*, **2010**, *48*, 487.
152. W. Xuan,.L. Zhi and K. Müllen. *Nano Lett*. **2008***, 8,* 323.
153. Y. Zhu, W. Cai, R. D. Piner, A. Velamakanni, and R. S. Ruoff. *App. Phys. Lett.,* **2009**, *95*, 103104.
154. a) H. A. Becerril, J. Mao, Z. Liu, R. M. Stoltenberg, Z. Bao, Y. Chen. *ACS Nano* **2008**, *2*, 463; b) X. Wang, L. Zhi, N. Tsao, Z. Tomovic, J. Li, K. Müllen. *Angew. Chem., Int. Ed.* **2008**, *47 (16),* 2990.
155. J. W. Kim, D. Kang, T. H. Kim, S. G. Lee, N. Byun, D. W. Lee, B. H. Seo, R. S. Ruoff, and H. S. Shin. *ACS Nano,* **2013**, *9*, 8082.
156. a) X. Luan, L. Chen, J. Zhang, G. Qu, J. C. Flake, Y. Wang. *Electrochimica Acta* , **2013**, *111*, 216; b) S. J. An, Y. Zhu, S. H. Lee, M. D. Stoller, T. Emilsson, S. Park, A. Velamakanni, J. An and R. S. Ruoff. *J. Phys. Chem. Lett.*, 2010, *1 (8),* 1259.
157. a) Y. Hernandez, V. Nicolosi, M. Lotya, F. M. Blighe, Z. Y. Sun, S. De, I. T. McGovern, B. Holland, M. Byrne, Y. K. Gun'ko, J. J. Boland, P. Niraj, G. Duesberg, S. Krishnamurthy, R. Goodhue, J. Hutchison, V. Scardaci, A. C. Ferrari, and J. N. Coleman, *Nat. Nanotechnol.* **2008** ,*3*, 563; b) S. Gilje, S. Han, M. Wang, K. L. Wang, R. B. Kaner. *Nano Lett.* **2007**, *7*, 3394.
158. a) S. Park, J. H. An, I. W. Jung, R. D. Piner, S. J. An, X. S. Li, A. Velama-kanni, and R. S. Ruoff. *Nano Lett.,* **2009**, *9*, 1593; b) D. A. Dikin, S. Stankovich, E. J. Zimney, R. D. Piner, G. H. B. Dommett, G. Evmenenko, S. B. T.Nguyen, R. S. Ruoff. *Nature,* **2007**, *448*, 457.
159. X. Li, G. Zhang, X. Bai, X. Sun, X. Wang, E. Wang and H. Dai. *Nature nanotechnology,* **2008***, 3*, 538.
160. L. J. Cote, F. Kim and J. Huang. *J. Am. Chem. Soc.,* **2009**, *131*, 1043.
161. R. Gengler, et al.*, Small* **2010***, 35.*
162. J. H. Fendler and F. C. Meldrum, *Adv. Mater.*, **1995**, *7,* 607.

163. L. J. Cote, F. Kim and J. X. Huang, *J. Am. Chem. Soc.,* **2009**, *131*, 1043.
164. X. L. Li, G. Y. Zhang, X. D. Bai, X. M. Sun, X. R. Wang, E. Wang and H. J. Dai, *Nat. Nanotechnol.,* **2008,** *3*, 538.
165. T. Szabo, V. Hornok, R. A. Schoonheydt and I. Dekany. *Carbon*, **2010**, *48*, 1676.
166. G. Eda, G. Fanchini and M. Chhawalla. *Nat. Nanotechnol.* **2008**, *3*, 270.
167. Z. Chen, Y.-M. Lin, M. J. Rooks and P. Avouris. *Phys. E*, **2007**, *40*, 228.
168. M. Y. Han, B. Ozyilmaz, Y. Zhang and P. Kim. *Phys. Rev. Lett.,* **2007**, *98*, 206805.
169. W. Liu, B. L. Jackson, J. Zhu, C.-Q. Miao, C.-H. Chung, Y.-Ju Park, K. Sun, J. Woo, and Y.-H. Xie. *ACS Nano*, **2010**, *4(7)*, 3927.
170. M. J. Allen, V. C. Tung, L. Gomez, Z. Xu, L. Chen, K. S. Nelson, C. Zhou, R. B. Kaner, Y. Yang. *Adv. Mater.* **2009**, *21*, 2098.
171. X. Liang, Z. Fu, S. Y. Chou. *Nano. Lett.* **2007**, *7*, 3840.
172. Z. Q. Wei, D. B. Wang, S. Kim, S. Y. Kim, Y. K. Hu, M. K. Yakes,A. R. Laracuente, Z. T. Dai, S. R. Marder, C. Berger, W. P. King, W. A. de Heer, P. E. Sheehan and E. Riedo. *Science*, **2010**, *328*, 1373.
173. Y. L. Guo, C. A. Di, H. T. Liu, J. A. Zheng, L. Zhang, G. Yuand Y. Q. Liu, *ACS Nano,* **2010**, *4*, 5749.
174. B. Li, X. T. Zhang, X. H. Li, L. Wang, R. Y. Han, B. B. Liu, W. T. Zheng, X. L. Li and Y. C. Liu. *Chem. Commun.,* **2010**, *46*, 3499.
175. J. M. Mativetsky, E. Treossi, E. Orgiu, M. Melucci, G. P. Veronese, P. Samori and V. Palermo. *J. Am. Chem. Soc.,* **2010**, *132*, 14130.
176. Z. Wei, D. E. Barlow, and P. E. Sheehan. *Nano Lett.*, **2008**, *8(10),* 3141.
177. Y. Guo, C. Di, H. Liu, J. Zheng, L. Zhang, G. Yu, and Y.Liu. *ACS Nano*, **2010**, *4(10)*, 5749.
178. V. Strong, S. Dubin, M. F. El-Kady, A. Lech, Y. Wang, B. H. Weiller and R. B. Kaner. *ACS Nano*, **2012**, *6*, 1395.
179. Y. Zhang, L. Guo, S. Wei, Y. He, H. Xia, Q. Chen, H.-B Sun, F.-S. Xiao. *Nano Today*, **2010**, *5*, 15.
180. Y. Zhou, Q. Bao, B. Varghese, L. A. L. Tang, C. K. Tan, C.-H. Sow, and K. P. Loh. *Adv. Mater.* **2009**, *21*, 1.
181. L. Zhang, H. Liu, Y. Zhao, X. Sun, Y. Wen, Y. Guo, X. Gao, C. Di, G. Yu, and Y. Liu. *Adv. Mater.*, **2012**, *24*, 436.

182. a) X. Li, G. Zhang, X. Bai, X. Sun, X. Wang, E. Wang, H. Dai, *Nat. Nanotechnol.* **2008**, *3*, 538; b) L. J. Cote, J. Kim, Z. Zhang, C. Sun, J. Huang. *Soft Matter* **2010**, *6*, 6096; c) Q. Zheng, B. Zhang, X. Lin, X. Shen, N. Yousefi, Z-D Huang, Z. Li, J-K Kim. **J. Mater. Chem. 2012**, **22**, 25072.

183. a) R. S. Edwards, K. S. Coleman. *Nanoscale,* **2013,** *5*, 38; b) J. Liu, Z. Yin, X. Cao, F. Zhao, L. Wang, W. Huang, H Zhang. *Adv. Mater.* **2013** *25*, 233; c) L. Liao, J. Bai, R. Cheng, H. Zhou, L. Liu, Y. Liu, Y. Huang, X. Duan. *Nano Lett.*, 2012, *12 (6)*, 2653.

184. a) Y. Guo, C. Di, H. Liu, J. Zheng, L. Zhang, G. Yu, Y. Liu. *ACS Nano* **2010**, *4(10)*, 5749; b) B. Y. Zhou, K. P. Loh. *Adv. Mater.* **2010**, *22*, 3615; c) J. Feng, W. Li, X. Qian, J, Qi, L, Qi, J. Li. *Nanoscale* **2012**, *4*, 4883; d) L-H Liu, G. Zorn, D. G. Castner, R. Solanki, M. M. Lerner, M. Yan. J. Mater. Chem. **2010**, *20*, 5041; e) W. Liu, B. L. Jackson, J. Zhu, C-Q Miao, C-Heui, Chung, Y-J Park, K. Sun, J. Woo, Y-H Xie. *ACS Nano.* **2010**, *4(7),* 3927; f) Y. Zhang, L. Guo, S. Wei, Y. He, H. Xia, Q. Chen, H-B Sun, F-S Xiao. *Nano Today* **2010**, *5*, 15; g) B. Y. Zhou, Q. Bao, B. Varghese, L. A. L. Tang, C. K. Tan, C-H Sow, K. P. Loh. *Adv. Mater.* **2009**, *21*, 1275; h) T. Kim, H. Kim, S. W. Kwon, Y. Kim, W. K. Park, D. H. Yoon, A-R Jang, H. S. Shin, K. S. Suh, W. S. Yang. *Nano Lett.* **2012**, *12*, 743.

2

Instrumentation and Characterization Techniques

"Chance favors the prepared mind"
- Louis Pasteur

The observation of materials at micro and nanoscale can be done using electrons, photons, scanning probes, ions, atoms, etc. A wide range of techniques is available and a systematic application of several tools leads to a complete understanding of the system. This chapter discusses the basic working principle of various characterization techniques that were used during the course of presented work.

Observation is the key to make new discoveries, and this is especially true for the nanoscale regime. In fact, as far as nano objects are concerned, one cannot proceed further without observing these objects. Observation is done with a probe, which may comprise of photons, electrons, neutrons, atoms, ions or even an atomically sharp pin. This chapter is devoted to explaining the basic principles on which different techniques are based and their application to understand various aspects of the formation of LB films.

2.1 LB Technique

LB technique is one of the most promising techniques for the preparation of organic thin films [1] as it enables,

1. A precise control over the monolayer thickness,
2. Homogenous deposition of monolayers over large areas on almost any kind of rigid as well as flexible substrate and
3. The possibility to make multilayer structures with varying layer composition.

For the work discussed in this thesis, LB technique has been extensively used for the assembly of 2D GO-sheets at the air-water interface.

Langmuir films.

Langmuir films consist of surface-active materials or 'surfactants' trapped at the interface between two dissimilar phases, either liquid-liquid or liquid-gas. Surfactants are molecules, which are amphiphilic in nature (**Figure 1**) and consist of a hydrophilic (water soluble) and hydrophobic (water insoluble) part. The hydrophobic part usually consists of hydrocarbon or fluorocarbon chains and the

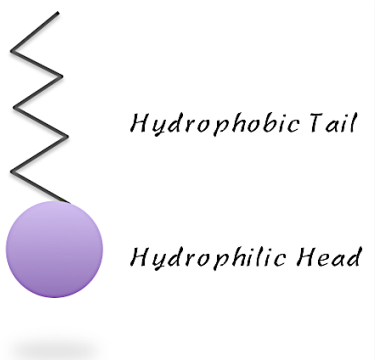

Figure 1. A schematic representation of an amphiphilic molecule showing hydrophobic (long hydrocarbon chain) and hydrophilic (polar group) parts.

forces acting upon them are predominantly van der Waal's type ($1/r^{12}$ and $1/r^{6}$). While the hydrophilic part consists of a polar group (–OH, –COOH, $-NH_3^+$, $-PO_4^-(CH_2)_2NH_2^+$ etc.) and the forces acting upon them are predominantly coulomb type ($1/r^2$).

Amphiphilic molecules are trapped at the air/water interface because they possess two very different types of bonding within one molecular structure. The driving force behind the association is the reduction of the free energy of the system. Therefore, when a surfactant comes in contact with water it accumulates at the air–water interface causing a decrease in the surface tension of water. Many of these amphiphilic molecules insoluble in water can (with the help of a volatile and water insoluble solvent) easily spread on a water surface with hydrophilic 'head' groups pulling the molecule into the bulk of the water and the hydrophobic 'tail' groups pointing towards the air. One molecule thick surface monolayer will only be achieved if the amphipathic balance (that is balance between hydrophilic and hydrophobic parts) of the molecule is correct. Sweeping a barrier over the water surface causes the molecules to come closer together and eventually form a compressed, ordered monolayer. The film produced by such a method is known as a *Langmuir–Film.*

Pressure–Area Isotherm (π–A isotherm).

The most important indicator of the monolayer properties of an amphiphilic molecule is given by measuring the changes in surface tension upon compressing the monolayer. The reduction of surface tension is known as the surface pressure (SP) i.e. SP is the lateral pressure that must be applied to prevent the film from spreading. Pressure readings are made by means of Wilhelmy plate attached to a microbalance. The plot of SP versus area occupied per molecule is known as a 'pressure–area isotherm' (π–*A* – isotherm) because compression takes place at constant temperature (**Figure 2**). The shape of isotherm is a characteristic of the molecules, building up of the film and hence provides a 2D 'fingerprint'. The π–*A* isotherm gives information about the stability of the molecules in the 2D system, phase transitions and conformational transitions. It also gives some idea about the amount of pressure that has to be applied to the film on the subphase, to enable deposition of the LB film in the solid– like phase. Thus at appropriate pressure, the film can be transferred to the substrate.

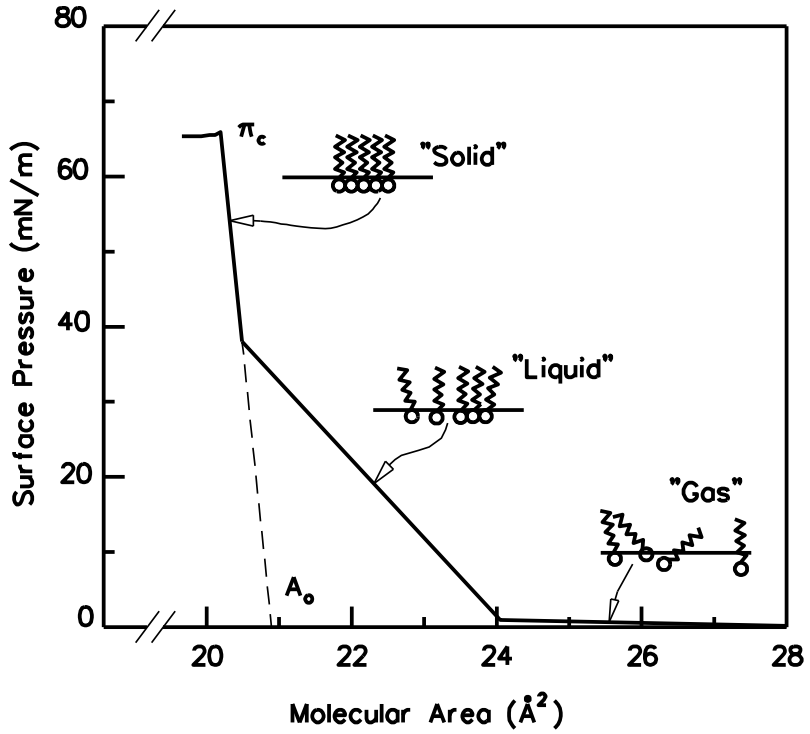

Figure 2. A typical pressure-area (π-A) isotherm showing the various phase transitions of the floating monolayer.

Deposition of LB films.

Langmuir film balance can also be used for building up highly organized multilayers of the amphiphiles. This is accomplished by successively dipping a solid substrate up and down through the monolayer while simultaneously keeping the SP constant by a computer controlled feedback system between the electro-balance measuring the SP and the barrier movement. Consequently the floating monolayer is adsorbed to the solid substrate. In this way, multilayer structures of hundreds of layers can be produced. These multilayer structures are commonly called Langmuir-Blodgett or simply LB films. The LB deposition is traditionally carried out in the 'solid' phase. The SP is then high enough to ensure sufficient cohesion in the monolayer so that the monolayer does not fall apart during transfer to the solid substrate. This also ensures the build up of homogeneous multilayers. The SP value that gives the best results depends on the nature of the monolayer. When the solid substrate is hydrophilic (glass, SiO_2 etc.) the first layer is deposited by raising the solid substrate from the subphase through the monolayer, whereas if the substrate is hydrophobic (HOPG, silanized SiO_2 etc.) the first layer is deposited by lowering the substrate into the subphase through the monolayer.

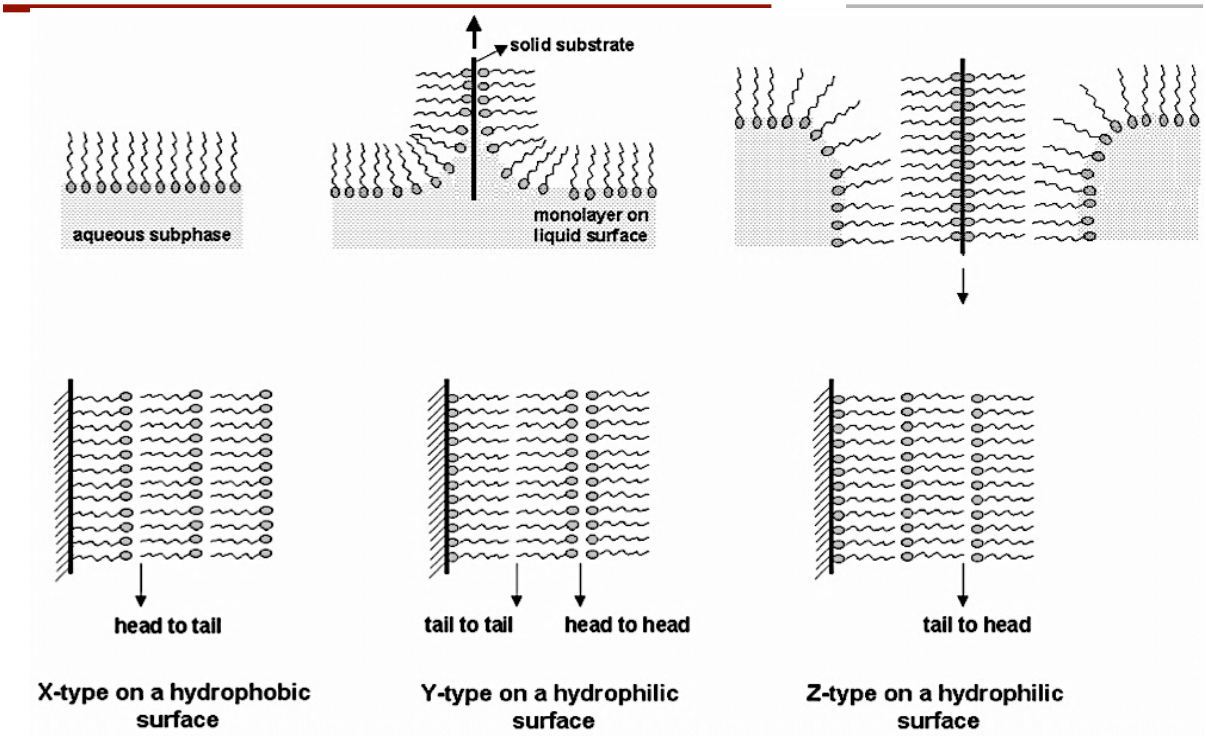

Figure 3. A schematic showing different types of deposition of LB films.

The parameters affecting the type of LB film produced are – the nature of the spread film, the subphase composition and temperature, SP during the deposition and the deposition speed, the type and nature of the solid substrate and the time the solid substrate is stored in air or in the subphase between the deposition cycles.

The quantity and the quality of the deposited monolayer on a solid support is measured by a transfer ratio (TR), given by:

$$TR = \frac{Trough\ area\ reduced\ by\ barriers}{Substrate\ area\ deposited}$$

For ideal transfer, the TR is 1. Different kind of LB multilayers can be produced and/or obtained by successive deposition of monolayers on the same substrate. The most common type is Y-type multilayer, which is produced when the monolayer deposits to the solid substrate in both upward and downward movement of the substrate. When the monolayer deposits only during upward or downward movement, the multilayer structure is called either Z-type or X-type (**Figure 3**). An alternative way to deposit the monolayer is the Langmuir-Schaeffer (LS) technique. This technique differs from the vertical deposition technique This technique differs from the vertical deposition technique x horizontally lowered in

Figure 4. KVS-NIMA LB Trough was used for the present work. Monolayer assemble and SP-area isotherm of GO were measured using this setup, the trough top inner dimensions of medium size LB were measured as 364 mm × 75 mm × 4 mm, SP was monitored using tensiometer attached to a wilhelmy plate.

contact with the monolayer (called horizontal dipping). KVS-NIMA of medium size LB trough was used for conducting all the experiments (**Figure 4**).

2.2 UV-Visible Spectroscopy

Absorption spectroscopy in different regions of electromagnetic spectrum (**Figure 5**) has been an important tool to the analyst since a long time [2]. Any molecular system possesses three types of energy namely electronic (E_{ele}), vibrational (E_{vib}) and rotational (E_{rot}) with decreasing magnitude in same order for a system. Absorption of energy leads to transition of electrons from ground state to excited state. The absorption peak thus obtained is broad, smooth and never very sharp due to the fact that the electronic absorption is accompanied with a corresponding change in the vibrational and rotational energies as well. The relationship between the energy absorbed in an electronic transition and the frequency (ν) in seconds, wavelength (λ) in nm and wavenumber ($\bar{\nu}$) in cm^{-1} of the radiation producing the transition is,

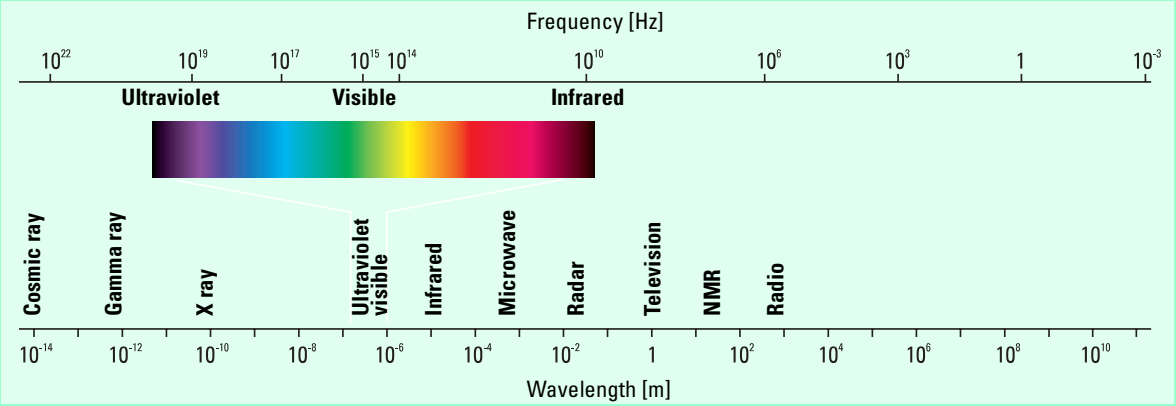

Figure 5. The Electromagnetic Spectrum.

$$E = h\nu = h\frac{c}{\lambda} = h\bar{\nu}c$$

where, h is Planck's constant, c is the velocity of light and ΔE is the energy absorbed in an electronic transition in a molecule from a low-energy state (ground state) to a high energy state (excited state). The position of absorption maxima for a molecule depends on the difference in the energy of the ground state level to that of excited state; larger the difference between the energies, higher is the frequency of absorption and thus smaller will be the wavelength. Absorption band shows two important characteristics; the position of the band which depends on the energy difference between electronic levels and the intensity which depends on the interaction between the radiation and electronic system as well as on the energy difference between the ground and excited state.

A convenient expression, which relates the absorbance with the path length that the radiation travels within the system and the concentration of the species, can be derived from the Lambert-Beer Law and is given as,

$$A = e.c.l$$

where, A is the measured absorbance = $\log_{10}(I_0/I)$ having no units, I_0 is the incident light intensity and I is the light intensity after it passes through the sample, e is the molecular absorbance or absorption coefficient absorptivity (in $dm^3\ mol^{-1}\ cm^{-1}$ units), c is the concentration (molarity) of the compound in the solution (in mol dm^{-3} units) and l is the path length of light in the sample (in cm units). In the presented work, Beckman UV-vis spectrophotometer, DU730, Beckman Coulter was used to study the optical properties of GO in solution (**Figure 5**).

Figure 5. Beckman UV-vis spectrophotometer, DU730, Beckman Coulter.

2.3 Fourier Transform Infrared Spectroscopy (FTIR)

Basic Principle.

The atoms in a molecule do not remain in a fixed relative position and vibrate about some mean position. If there is a periodic alternation in the dipole moment due to this vibrational motion, then such mode of vibration is infrared (IR) active. The IR region of the electromagnetic spectrum is around 100 μm – 1 μm wavelengths. The vibrating molecule absorbs energy only from the radiation with which it can coherently interact, i.e. the radiation of its own oscillation frequency. The appearance or non-appearance of certain vibrational frequencies gives valuable information about the structure of a particular molecule. The frequency of vibration is given by the relation:

$$\nu = \frac{1}{2\pi}\sqrt{\frac{k}{\mu}}$$

where, k is force constant; μ is reduced mass.

The number of absorption peaks is related to the number of vibrational freedom of the molecule. The intensity of absorption peaks is related to the change of dipole moment and the possibility of the transition of energy levels. Therefore, by analyzing the infrared spectrum, one can readily obtain abundant structure information of a molecule. Most molecules are infrared active except for several homonuclear diatomic molecules such as O_2, N_2 and Cl_2 due to the zero dipole change in the vibration and rotation of these molecules. What makes infrared absorption spectroscopy even more useful is the fact that it is capable to analyze

all gas, liquid and solid samples. The commonly used region for infrared absorption spectroscopy is 4000 ~ 400 cm^{-1} because the absorption radiation of most organic compounds and inorganic ions is within this region. The infrared spectra were performed on a Perkin Elmer Spectrum 100 FT-IR system (Perkin Elmer, USA). The range of Infrared region is 12800 ~ 10 cm^{-1} and can be divided into near-infrared region (12800 ~ 400 cm^{-1}) mid-infrared region (4000 ~ 200 cm^{-1}) and far-infrared region (50 ~ 1000 cm^{-1}).

2.4 Raman Spectroscopy

Basic Principles.

Raman spectroscopy is a spectroscopic technique based on inelastic scattering of monochromatic light, usually from a laser source. Inelastic scattering means that the frequency of photons in the monochromatic light changes upon interaction with the sample. Photons of the laser light are absorbed by the sample and then re-emitted. Frequency of the re-emitted photons is shifted up or down in comparison to the original monochromatic frequency, which is known as the Raman shift. This shift provides information about vibrational, rotational and other low frequency transitions in molecules. Raman spectroscopy can be used to study solid, liquid and gaseous samples [3].

Typically, a sample is illuminated with a laser beam. Light from the illuminated spot is collected with a lens and sent through a monochromator.

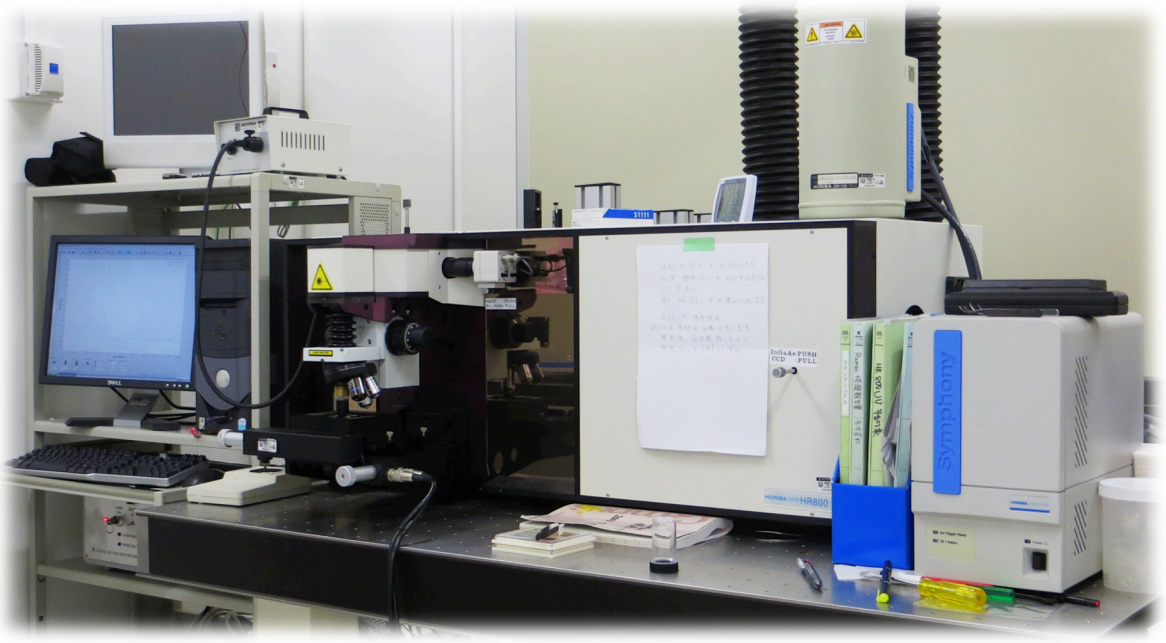

Figure 6. HORIBA JOBINYVON-HR800 UV Raman- PL spectrophotometer.

Wavelengths close to the laser line due to elastic Rayleigh scattering are filtered out while the rest of the collected light is dispersed onto a detector. The Raman effect occurs when light impinges upon a molecule and interacts with the electron cloud and the bonds of that molecule. For the spontaneous Raman effect, which is a form of light scattering, a photon excites the molecule from the ground state to a virtual energy state. When the molecule relaxes it emits a photon and it returns to a different rotational or vibrational state. The difference in energy between the original state and this new state leads to a shift in the emitted photon's frequency away from the excitation wavelength. Raman spectroscopy is commonly used in chemistry, since vibrational information is specific to the chemical bonds and symmetry of molecules. Here, we have used Raman spectroscopy to characterize reduced graphene oxide samples using HORIBA JOBINYVON-HR800 UV Raman-PL spectrophotometer with a 200 mW argon-ion laser at an excitation wavelength of 514 nm **(Figure 6**).

2.5 Zeta Potential Measurement

Basic Principles.

Zetasizer is an instrument that measures the size of particles and molecules of 1 nanometer to several microns using dynamic light scattering. It measures zeta potential as well as electrophoretic mobility using electrophoretic light scattering. Zetasizer performs the size measurements using a process called Dynamic Light Scattering (DLS). DLS is otherwise known as Photo Correlation Spectroscopy and it measures the Brownian motion and relates it to the size of the particles. It does this by illuminating the particles with a laser beam and analyzing the intensity fluctuations in the scattered light. Brownian motion is the property of the particles to move randomly in a medium resulting from collisions of molecules. Particles suspended in a liquid medium move continuously due to Brownian motion. An important feature of Brownian motion for DLS is that small particles move more quickly and large particles move more slowly. The relationship between the size of a particle and its speed due to Brownian motion is defined in the Stokes-Einstein equation. On the basis of this difference in the intensity fluctuations, size of the particles can be found out. DLS curve can be depicted or described using three ways: number, volume and intensity.

Transmitting a laser beam through the sample performs zeta potential measurement by splitting the beam into an incident and a reference beam. When an electric beam is applied to the cell containing the sample, any particles moving

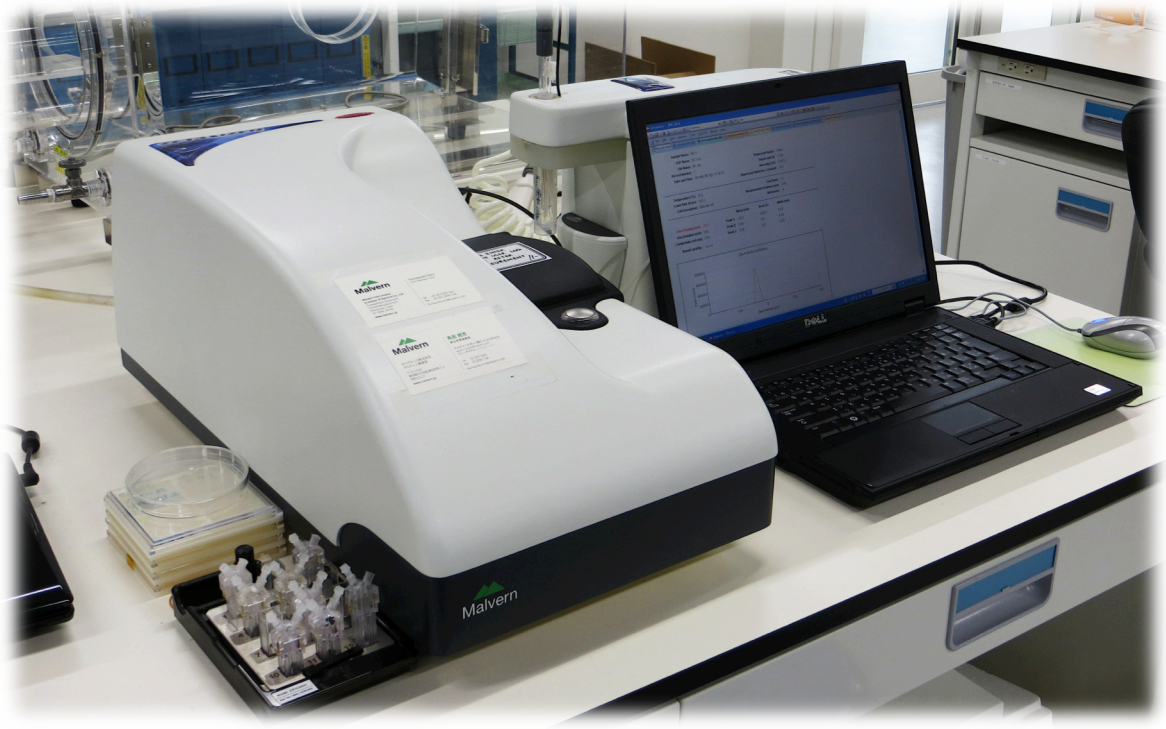

Figure 7. Zetasizer ZS90, Malvern, Japan.

through the measurement volume will cause the intensity of light detected to fluctuate with a frequency proportional to the particle speed. Detector receives the information and a frequency distribution spectrum is obtained from which electrophoretic mobility and hence the zeta potential is calculated [4]. Malvern Zetasizer Nano-ZS was used for the characterization of various types nanoparticles (**Figure 7**).

2.6 Scanning Electron Microscopy (SEM)

Basic Principles.

SEM is an extremely useful tool to study the surface properties of a material because it offers a very high resolution as compared to the optical microscope. It uses electrons emitted from tungsten or Lanthanum hexaboride (LaB_6) thermionic emitters for the visualization of surface of the material. The filament is resistively heated via specific current to achieve temperature between 2000-2700 K. This results in an emission of thermionic electrons from the tip over an area about 100 µm x 150 µm. The electron gun generates electrons and accelerates them to energy in the range 0.1 – 30 keV towards the sample [5]. A series of lenses focus the electron beam on to the sample where it interacts with the specimen to a depth of ~ 1 µm.

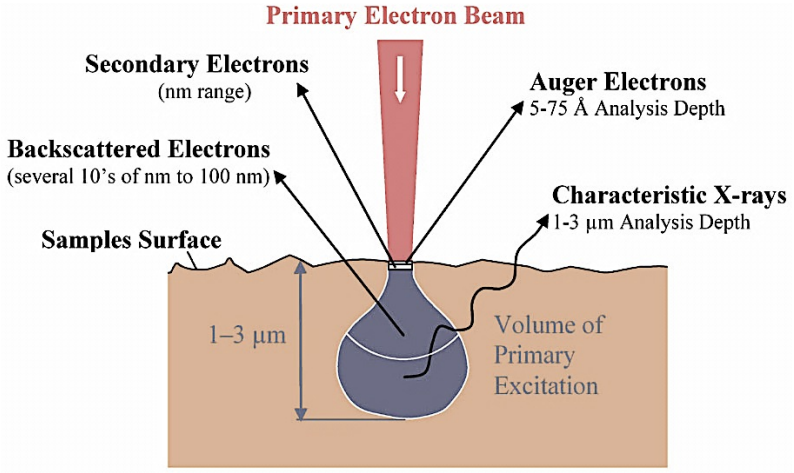

Figure 8. Schematic representation of the possible effects after specimen-electron beam interaction.

When the electron beam impinges on the specimen, many types of signals are generated and any of these can be displayed as an image (**Figure 8**). The two signals most often used to generate SEM images are *secondary electrons* (SE) and backscattered electrons (BSE). Most of the electrons are scattered at large angles (from 0° to 180°) when they interact with the positively charged nucleus. These elastically scattered electrons are usually called BSE. Some electrons are scattered in-elastically due to the loss in K.E. upon their interaction with orbital shell electrons. Incident electrons may knock-off loosely bound conduction electrons out of the sample called SE. These SEs along with BSEs are widely used for SEM topographical imaging.

Both SE and BSE signals are collected when a positive voltage is applied to the collector screen in front of the detector. When a negative voltage is applied on the collector screen only BSE signal is captured because the low energy SEs are repelled. Electrons captured by the scintillator/ photomultiplier are then amplified and used to form an image in the SEM.

When the electron beam knocks-off the inner shell electron, electron from higher energy levels drop to lower energy levels resulting in the emission of Auger electrons, which are used to draw information about the chemical composition of the sample. This technique is called as Auger Electron Spectroscopy (AES). The emission can also be in the form of photons known as X-ray photons and have high energy, which are used for the compositional analysis of the sample. This technique is known as energy dispersive analysis of X-ray (EDAX) and is used extensively to study the elemental composition of the sample. The morphology

Figure 9. Hitachi SEM, SU8030.

and size of GO were measured with Hitachi SEM, SU8030 at an accelerating voltage of 5 KV (**Figure 9**).

2.7 Atomic Force Microscopy (AFM)

Basic Principles.

AFM is a revolutionary sophisticated technique to study the topology of a sample in x, y as well as z-direction. It utilizes a sharp tip at the end of cantilever

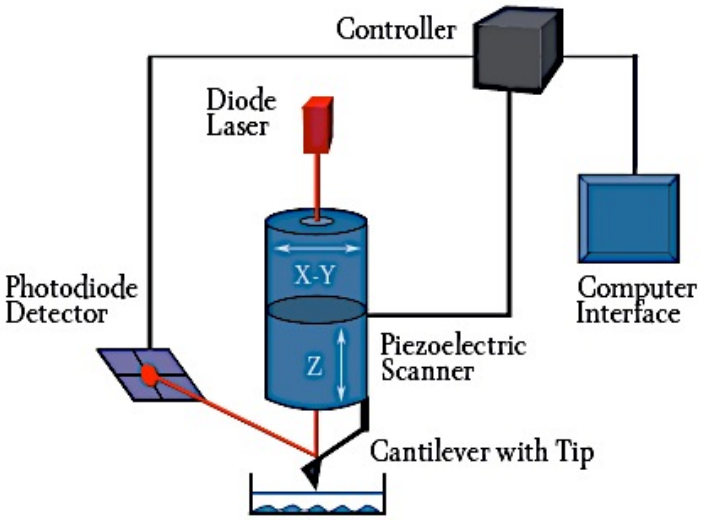

Figure 10. Schematic showing the basic principle behind AFM.

that moves over the sample in a raster scan and bends in response to the force between the tip and the sample. Initially, AFM was equipped with a scanning tunneling microscope at the end of the cantilever to monitor its bending, but now, an optical lever technique has been employed for this purpose. As the cantilever bends, light from the laser is reflected onto the split photo-diode. The difference in the signal is used as a measure of bending of the cantilever. The bending of the cantilever obeys the Hooke's law for small displacements and so the force between the tip and the sample can be calculated. A device made of piezo-electric ceramic in the form of a tube scanner is used to control the movement of the tip or the sample. The scanner is capable of sub-angstrom level resolution in the x, y or z direction, z being the direction perpendicular to the sample (**Figure 10**).

The AFM can be operated in two modes namely, with feedback control and without feedback control. The feedback control mode works at a constant force between the tip and the sample where the piezo which moves the sample (or the tip) responds to any change in the force between the sample and the tip and alters the separation between the two to restore the original value of the force. This measurement is known as height mode measurement and enables reliable topographical analysis of the sample. When the feedback control mode is off, the measurement is performed at constant height (deflection mode), which is useful for high-resolution analysis of the samples that are extremely flat. AFM incorporates several refinements such as sensitive detection, flexible cantilever,

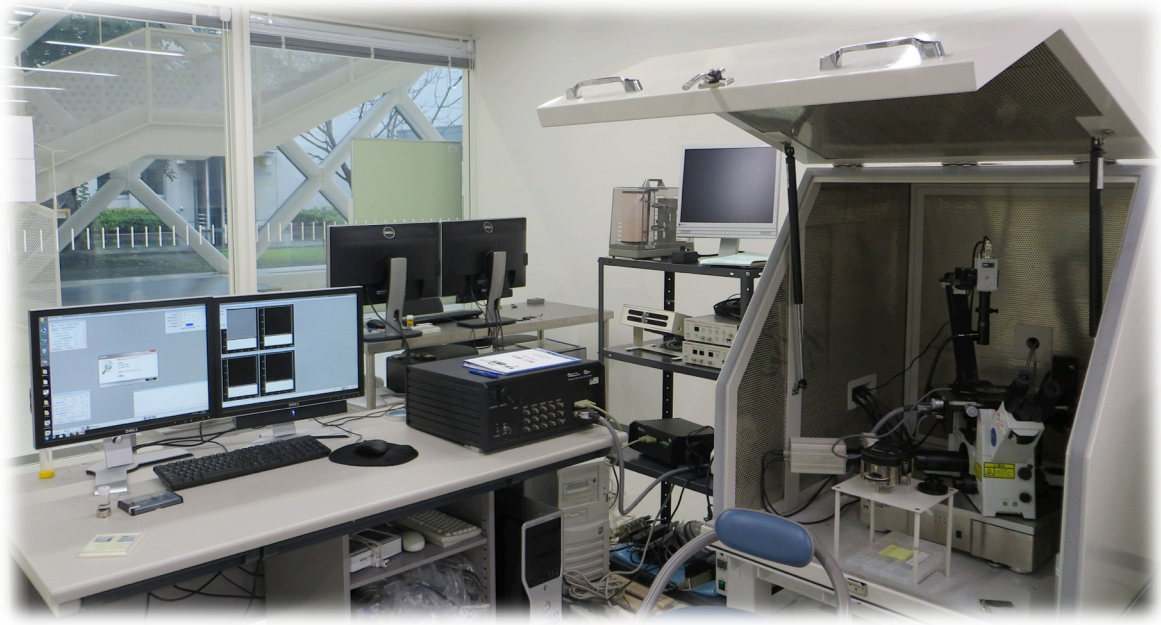

Figure 11. MFP-3D-CF, Asylum Research AFM.

sharp tips, high resolution precise tip-sample positioning and force feedback, which enables it to achieve atomic level resolution. Since, imaging process uses the force of interaction of the atoms on the tip to that of the sample, AFM is used for imaging even the non-conducting samples.

AFM measurements can be performed in contact, tapping or non-contact modes, the difference being the extent of tip-sample interaction during the measurement. Contact mode AFM is the most commonly used method where the tip remains in close contact with the sample during the process of scanning. The force of interaction between the tip and the sample lies in the repulsive regime in the intermolecular force curve. Contact mode AFM provides 3D information of the sample non-destructively with 1.5 nm lateral and 0.05 nm vertical resolution. Tapping mode is generally used for imaging soft and poorly immobilized samples. The tip is oscillated at its resonating frequency and positioned over the sample so that it contacts the sample for a short time interval during oscillation. In the non-contact mode, the tip is oscillated at a distance from the sample so that the two are no longer in contact. AFM image of GO sheets were recorded using Asylum Research Cypher Scanning Probe Microscope (SPM), AC mode imaging in air with OmegaLever OMCL-AC55TS-R3 micro cantilever (nominal resonant frequency of 1.6 MHz, a nominal spring constant of 85 N/m. However, the surface roughness of SiO_2/Si substrate was measured using MFP-3D-CF, Asylum Research AFM using non- contact AC-Air topographic mode with a scan rate of 1.0 Hz, using OLYMPUS (Model OMCL- AC240TS) cantilever (nominal resonant frequency of 70 kHz, a nominal spring constant of 2 N/m, and a typical tip radius of < 10 nm) (**Figure 11**).

2.8 Transmission Electron Microscopy (TEM)

Basic Principle.

In TEM analysis, a thin specimen is illuminated with electrons in which the electron intensity is uniform over the illuminated area. As the electrons travel through the specimen, they are either scattered by a variety of processes or they may remain unaffected by the specimen. The end result is that a non-uniform distribution of electrons emerges from the exit surface of the specimen that contains all the structural and chemical information about the specimen. Electron microscope displays this non-uniform distribution of electrons in two different ways.

Angular distribution of scattering can be viewed in the form of scattering

Figure 12. JEM 2200FS, JEOL

patterns, usually called diffraction patterns, and spatial distribution of scattering can be observed as contrast in images of the specimen. The advantage of this arrangement is the possibility of directly viewing the area from which the diffraction pattern arises. All the TEM images were acquired by JEM 2200FS, JEOL at 200KV. Highly diluted sample was dropped on 400 mesh copper grid. For selected area electron diffraction (SAED) a small spot size was used to increase beam coherence, spread into a parallel beam (**Figure 12**).

2.9 X-ray Photoelectron Spectroscopy (XPS)

XPS is a surface sensitive technique, which is used extensively for the compositions and oxidation state analysis of the sample. It is also know as Electron Spectroscopy for Chemical Analysis (ESCA) due to the fact that it gives accurate quantitative information of the surface of the sample. XPS uses X-ray of a characteristic energy to excite electrons from orbitals in atoms. It is based on the concept of photoelectric effect. In photoelectron spectroscopy, a monochromatic source of X-ray (i.e. fixed energy governed by the relation E = hν) to knock off inner core electrons from the atoms constituting the sample resulting in ionization. The kinetic energy of the emitted electrons can be calculated using a suitable electrostatic or electromagnetic analyzer and thus the spectrum of the sample

could be recorded as a function of number of electrons of a given energy emitted per unit time.

A simple way to understand it is equation 1 that shows the ionization process of an element A.

$$A + h\nu = A^{+} + e^{-} \quad \text{.....(1)}$$

According to the law of conservation of energy,

$$E(A) + h\nu = E(A^{+}) + E(e^{-}) \quad \text{.....(2)}$$

Since the entire energy of the emitted electron will be kinetic energy (KE), equation 2 can be rearranged as follows,

$$KE = h\nu - [E(A^{+}) - E(A)] \quad \text{.....(3)}$$

The term in the square bracket represents the energy difference between the ionized and the atomic state of an atom, known as the binding energy (BE), which is characteristic for an atom. The equation 3 is thus simplified to

$$KE = h\nu - BE \quad \text{.....(4)}$$

The BE is measured with respect to the fermi energy level in solids and therefore equation 4 is modified incorporating the work function (φ) term for the solids.

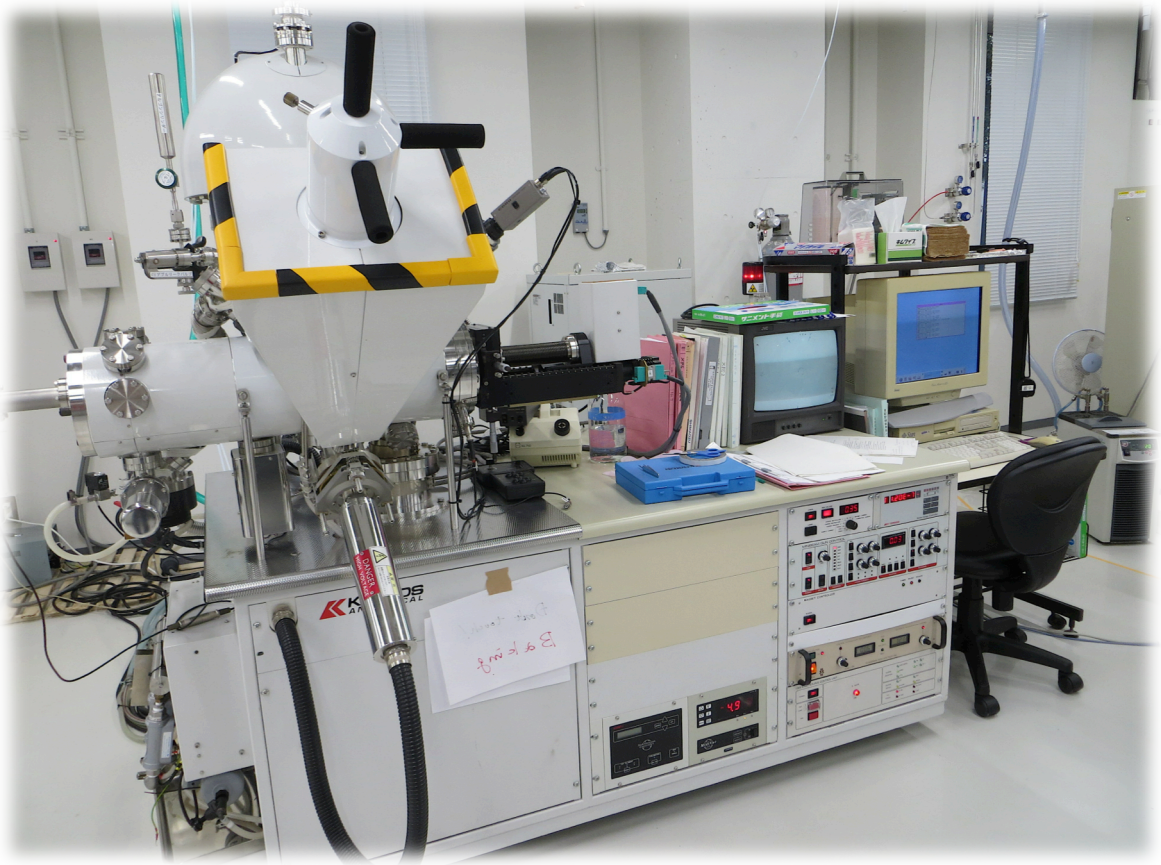

Figure 13. AXIS-Hi, Shimadzu/KRATOS.

$$KE = h\nu - BE - \varphi \quad \text{.....(5)}$$

Thus, from the equation 5, employing the photon of known energy hν and measuring the kinetic energy of the emitted electron and with known work function φ, it is possible to find the binding energy, a characteristic signature of an element. Electron traveling out through the material undergo inelastic collision with the bound electron in the material resulting into energy loss. This gives a strong background to the spectrum rather than a very sharp peak. It is due to this reason that the electrons, which come out from near the surface, give the true information about the chemical composition. Such electrons are emitted from a very short distance inside the material (< 100 nm) and thus XPS is known to be a surface sensitive technique where the emitted photoelectrons are detected for analysis [6].The BE of an electron does not only depend upon the energy level of emission but also upon the oxidation state of the concerned atom and the local surrounding to that atom. A change in either of the two factors results in a shift of the peak for that atom in the spectrum, which is known as *chemical shift*. Atoms of a higher positive oxidation state exhibit a higher binding energy due to the extra coulombic interaction between the photo-emitted electron and the ion core.

Similarly, the presence of an electronegative atom in the surrounding of the atom in question, will impart a net partial positive charge to that atom. Thus, emission of an electron from such an atom will require higher energy, which shifts the peak to higher binding energy. This ability to discriminate between different oxidation states and chemical environments is one of the major strengths of the XPS technique. XPS analysis of a selection of GO and rGO films was carried out using AXIS-Hi, Shimadzu/KRATOS under basic pressure of 5.6 x 10^{-9} Torr. And the X-ray source used was anode mono-Al with pass energy of 40 eV and 80 eV. To evaluate the functional groups present on the samples, curve fitting was performed using CasaXPS software (Version 2.3.16 Pre-rel 1.4) (**Figure 13**).

2.10 Plasma System

Basic Principle.

The plasma state is generated when a gas is subjected to sufficient energy to break down its molecular integrity and dissociate it into ions, electrons and

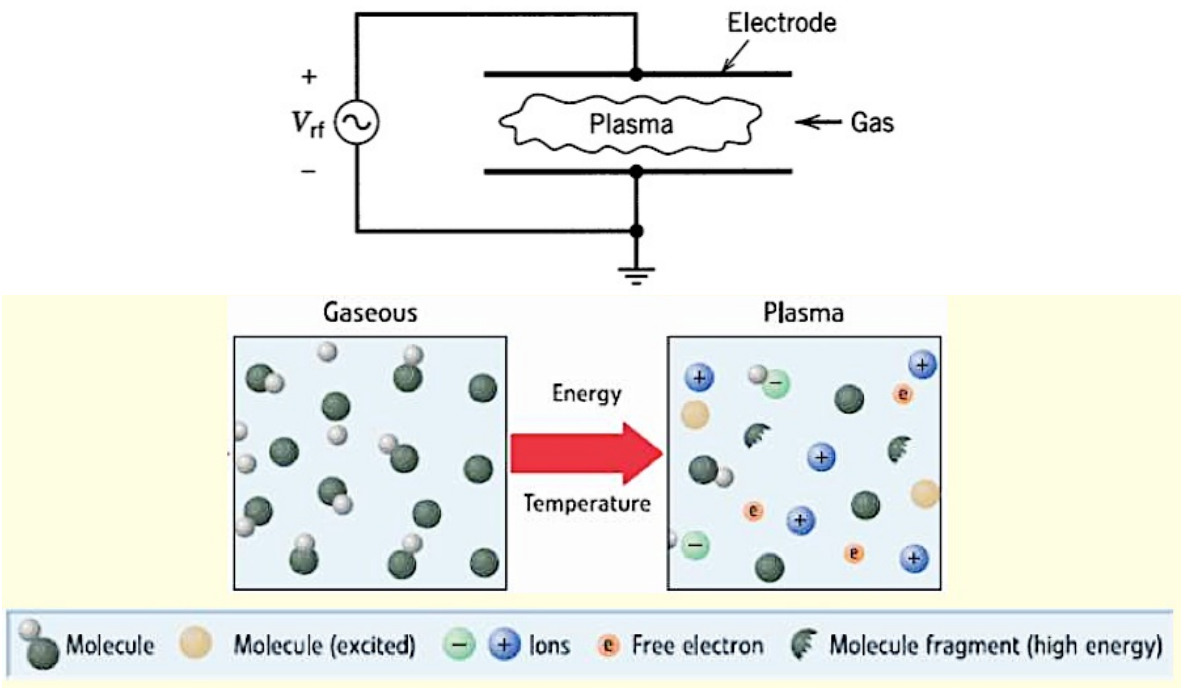

Figure 14. Schematic showing the basic principle behind plasma system.

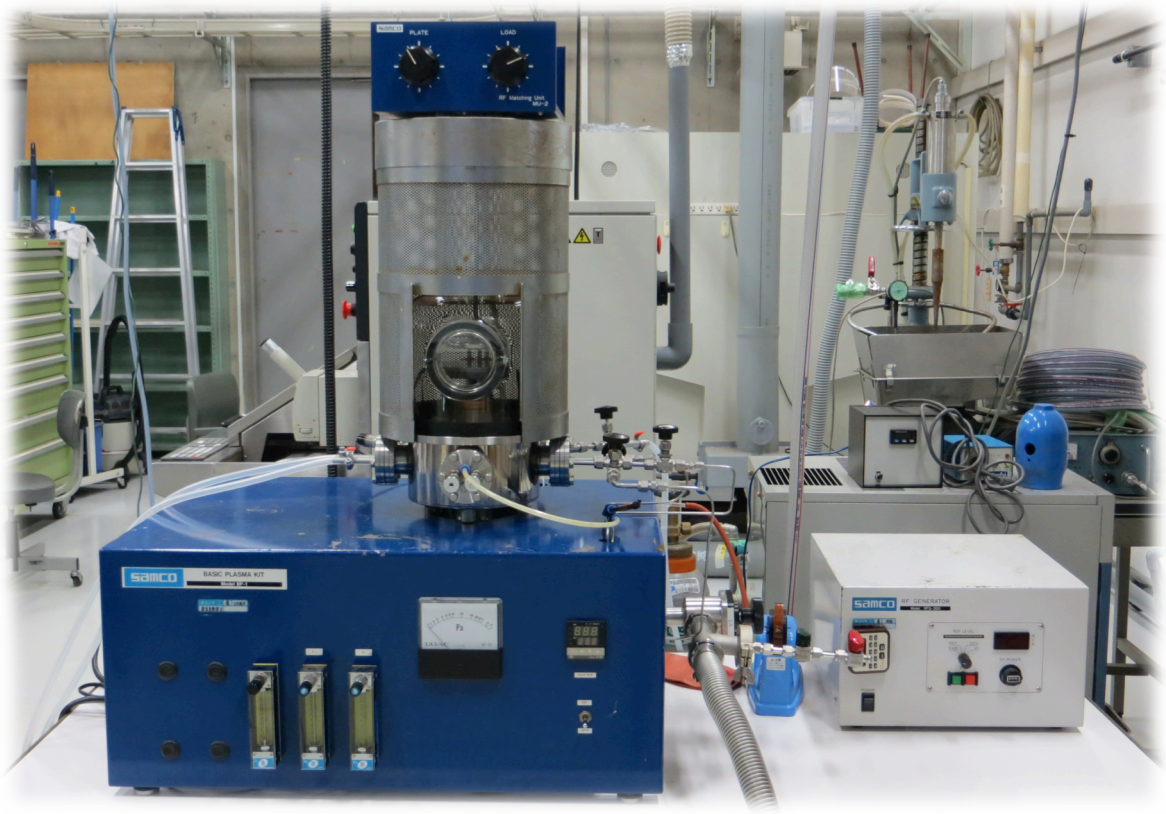

Figure 15. Basic Plasma Kit, Model BP-1) equipped with RF generator of 13.6 MHz, Model RFG-300 (Samco, Japan)

between two (or three) electrodes. Dependent on the polarities involved, the ions (+ polarity) that are formed are accelerated in one direction and electrons (- polarity) are accelerated in the opposite direction (**Figure 14**). Ideally, the surfaces to be cleaned (or modified) are positioned on a sample tray that is parallel to the electrode sets so that the plasma action is evenly distributed across the sample plane and all samples get the same degree of cleaning.

Everyday examples of plasma are fluorescent and neon lights, the aurora borealis and the surface of the sun.

The plasma treatment of SiO_2/Si substrate was carried out using Basic Plasma Kit, Model BP-1) equipped with RF generator of 13.6 MHz, Model RFG-300 (Samco, Japan). The gap between the two electrodes was fixed at 23 mm (**Figure 15**).

2.11 Optical Emission Spectroscopy (OES)

Plasmas can be used for a variety of applications. For example, it is one of the most efficient ways to clean, activate or coat surfaces. To create and utilize perfect plasma, it is necessary to know all processes that take place within the plasma system and its properties. One of the most important methods to analyze plasma characteristics is by OES. As it does not interfere with the plasma itself, information on the undisturbed plasma can be obtained.

Basic Principle.

OES involves applying electrical energy in the form of spark generated between an electrode and a metal sample, whereby the vaporized atoms are brought to a high-energy state within a so-called “discharge plasma”. These excited atoms and ions in the discharge plasma create a unique emission spectrum specific to each element. Thus, a single element generates numerous characteristic emission spectral lines. Therefore, the light generated by the discharge can be said to have a collection of the spectral lines generated by the elements in the sample. This light is split by a diffraction grating to extract the emission spectrum for the target elements (**Figure 16**). The intensity of each emission spectrum depends on the concentration of the element in the sample. Detectors (photomultiplier tubes) measure the presence or absence or presence of the spectrum extracted for each element and the intensity of the spectrum to perform qualitative and quantitative analysis of the elements. [7]. Ocean Optics (USB2000+) optical emission spectrophotometer was employed to monitor the optical emission spectrum of N_2-plasma from 200-900 nm region.

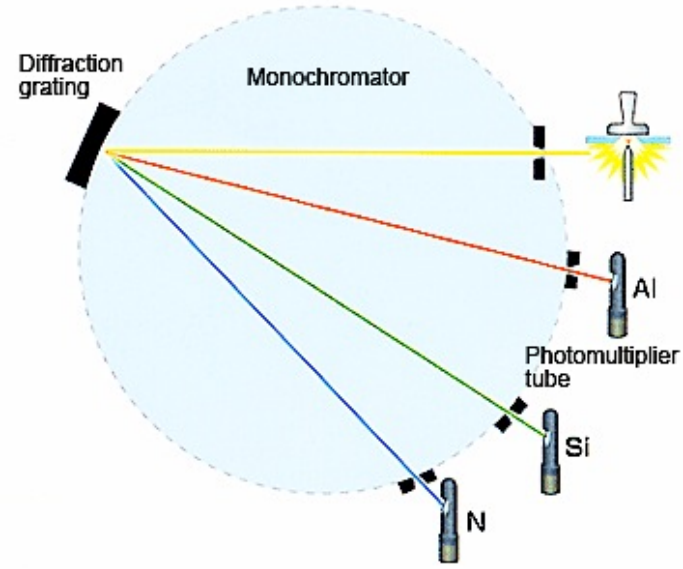

Figure 16. Schematic showing the basic working principle of OES.

2.12 Contact Angle Measurements

What is Contact Angle?

Contact angle, θ, is a quantitative measure of the wetting of a solid by a liquid. It is defined geometrically as the angle formed by a liquid at the three-phase boundary where a liquid, gas and solid intersect as shown in **Figure 17**. It can be seen from this figure that low values of θ indicate that the liquid spreads, or wets well, while high values indicate poor wetting. If the angle θ is less than 90° the liquid is said to wet the solid. If it is greater than 90° it is said to be non-wetting. A zero contact angle represents complete wetting.

How is Contact Angle Measured?

Two different approaches are commonly adapted to measure contact angles of non-porous solids- goniometry and tensiometry. Goniometry involves the observation of a sessile drop of test liquid on a solid substrate. Tensiometry involves measuring the forces of interaction as a solid is contacted with a test liquid. *Goniometry*: Analysis of the shape of a drop of test liquid placed on a solid is the basis for goniometry. The basic elements of a goniometer include a light source, sample stage, lens and image capture. Contact angle can be assessed directly by measuring the angle formed between the solid and the tangent to the drop surface. Goniometry can be used in many situations where tensiometry cannot. One can use a great variety of solid substrates provided they have a relatively flat portion for testing and can fit on the stage of the instrument. Substrates with regular curvature, such as contact lenses are also easily analyzed.

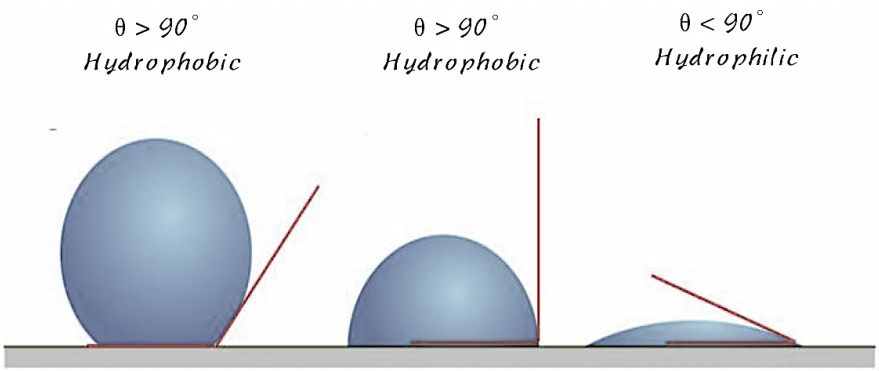

Figure 17. Schematic showing the different contact angles of a liquid drops on solid substrate.

Figure 18. Kyowa Interface Science Co., Ltd. (Tokyo, Japan), equipped with FAMAS interface Measurement & Analysis System software.

Testing can be done using very small quantities of liquid. It is also easy to test high temperature liquids such as polymer melts.

The contact angle measurements of a sessile water drop (1 μL) were carried out on the SiO_2/Si before and after N_2-plasma treatment. The digital images and contact angle formed by sessile water drop on the solid substrates were measured using Kyowa Interface Science Co., Ltd. (Tokyo, Japan), equipped with FAMAS interface Measurement & Analysis System software (**Figure 18**).

2.13 Electron Beam Lithography (EBL)

Basic Principle.

EBL is a fabrication tool, which helps us to create nanoscale patterns. The fundamental idea originates from the fact that electron has wave particle duality where the wavelength can be easily controlled by its energy. As an example, for

100 keV electrons, the corresponding wavelength can be calculated from the following equation,

$$\lambda = h\frac{c}{E} = 0.012\ nm$$

which is significantly smaller than typical visible light or UV light (on the order of 100 nm). This simply means that by using a high-energy electron beam, the diffraction limit, which consequently "smears out" the edge of a pattern, does not exist. Therefore, we can easily reach nanometer scale by EBL to explore the nanoscale world.

EBL is the practice of emitting a beam of electron in a patterned fashion across a surface covered with a film (called the resist) ("exposing" the resist) and of selectively removing either exposed or non-exposed regions of the resist ("developing"). It was developed for manufacturing integrated circuits, and is also used for creating nanotechnology architectures. The primary advantage of EBL is that it is one of the ways to beat the diffraction limit of light and make features on the nanometer scale.

Patterning of Electron Sensitive Resists.

EBL is carried out on electron-sensitive resist materials such as the polymer. Solutions of the resist are spin-coated onto a sample and baked to leave a hardened thin-film on the surface of sample. The EBL system is then used to move a focused electron beam across the sample to selectively expose a pattern in the resist previously designed with the system s in-built CAD tools.

Exposure of a positive tone resist to electrons causes fragmentation of the polymer chain into smaller molecular units in a process known as *chain-scission*. A suitable developer solution can then be used to selectively dissolve the fragmented polymer chains in the exposed areas of resist, whereas the unexposed resist remains insoluble in the developer solution. The process therefore leaves a patterned resist mask on the sample that can be used for further processing (**Figure 19**).

Elionix ELS-7700, Electron Beam Lithography System and Elionix ELS-G-125, Ultra High Precision Electron Beam Lithography System (**Figure 20**) were used for making patterns. Formation of pattern and alignment is precise and accurate as the electron beam is computer controlled. The electron beam is generated from the top

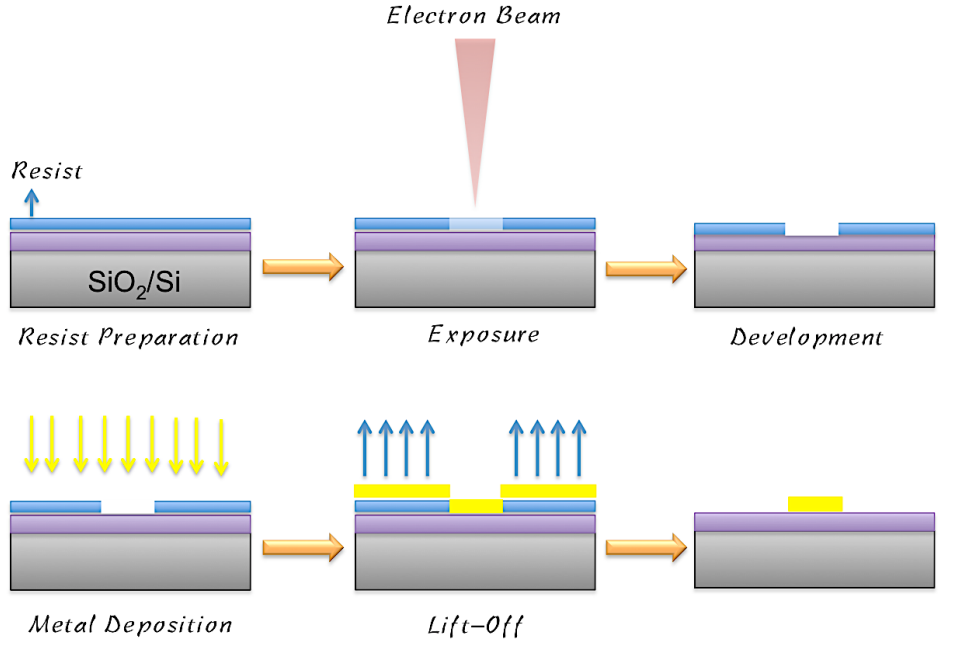

Figure 19. Typical EBL Process.

that the beam remains collimated; whereas the blanking aperture serves to prevent the beam from writing at those areas that are not meant for writing. The deflection system allows the scanning of beam across the sample. This whole process involves,

1. Resist Preparation for Exposure

SiO_2/Si substrates were coated with a thin layer of ZEP520A, a positive EB resist which shows high resolution (Mw 57000) using spin coater at 500 rpm × 5 sec → 3000 rpm × 60 sec. At this spinning rate, the resist thickness was found to be ~ 400 nm.

The samples were then baked at 180 °C for 3 min. The exposure pattern for each layer is created using the AutoCad Software.

2. Exposure

The samples are loaded into the electron beam column and the column is pumped down until the vacuum reaches < 1 x 10^{-4} Pa. The acceleration voltage used was 75 kV while the emission current was 117 μA and the beam current used was 50 pA and 1000 pA to draw small and large electrodes. The electron beam is then focused and the stage height is adjusted for exposure. Subsequently, the patterns are written on the sample. The samples are then unloaded and were kept for the development process.

3. Development

The exposed samples were developed with O-xylene developer solution for

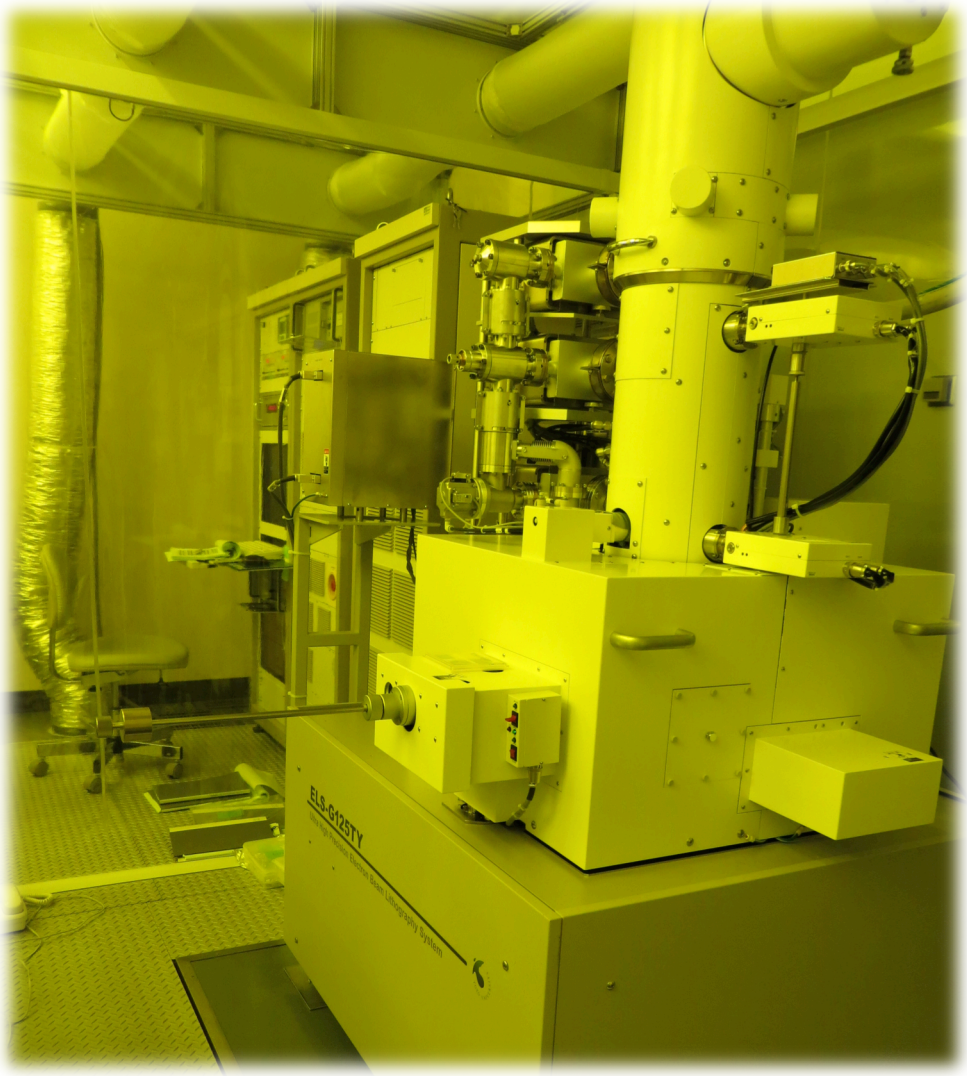

Figure 20. ELS-G125TY, Ultra High Precision Electron Beam Lithography System.

3 min to remove the resist areas exposed by electron-beam and then rinsed in IPA solution for another 1 min. The sample was dried by N_2 gas blow and then checked under high-power optical microscope to ensure complete development.

4. Metal Deposition

Vacuum evaporation system was used for the deposition of metal such as Aluminum (Al) or Titanium (Ti) or Nickel (Ni) or Gold (Au). Vacuum evaporation occurs when metal is heated to a liquid state allowing the molecules to escape into the chamber resulting in some of them being deposited on the substrate.

5. Lift-off Process

By dissolving the resist with a solvent such as THF, the excess film deposited on top of the resist layer and the resist itself were removed, leaving the designed pattern on the surface. The sample was then dried by N_2 gas blow and then

checked under optical microscope to ensure complete lift-off process.

2.14 Photolithography (UVL)

Basic Principle.

The basic principle of UVL is very similar with conventional EBL. A schematic of UVL fabrication process is shown in **Figure 21**. It is a process used in microfabrication to pattern parts of a thin film or the bulk of a substrate.

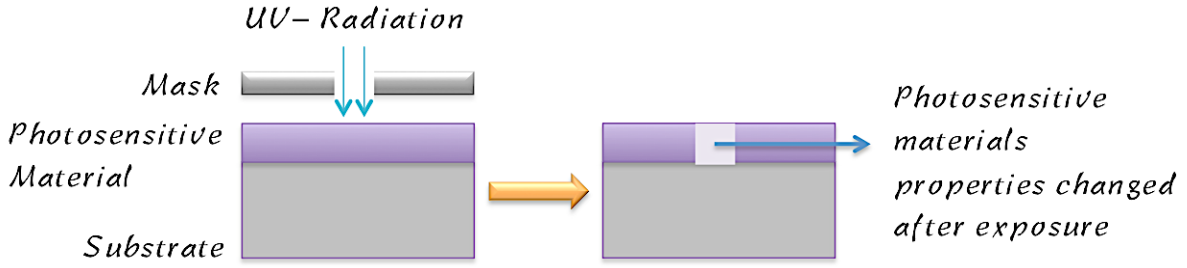

Figure 21. Typical Photolithography Process.

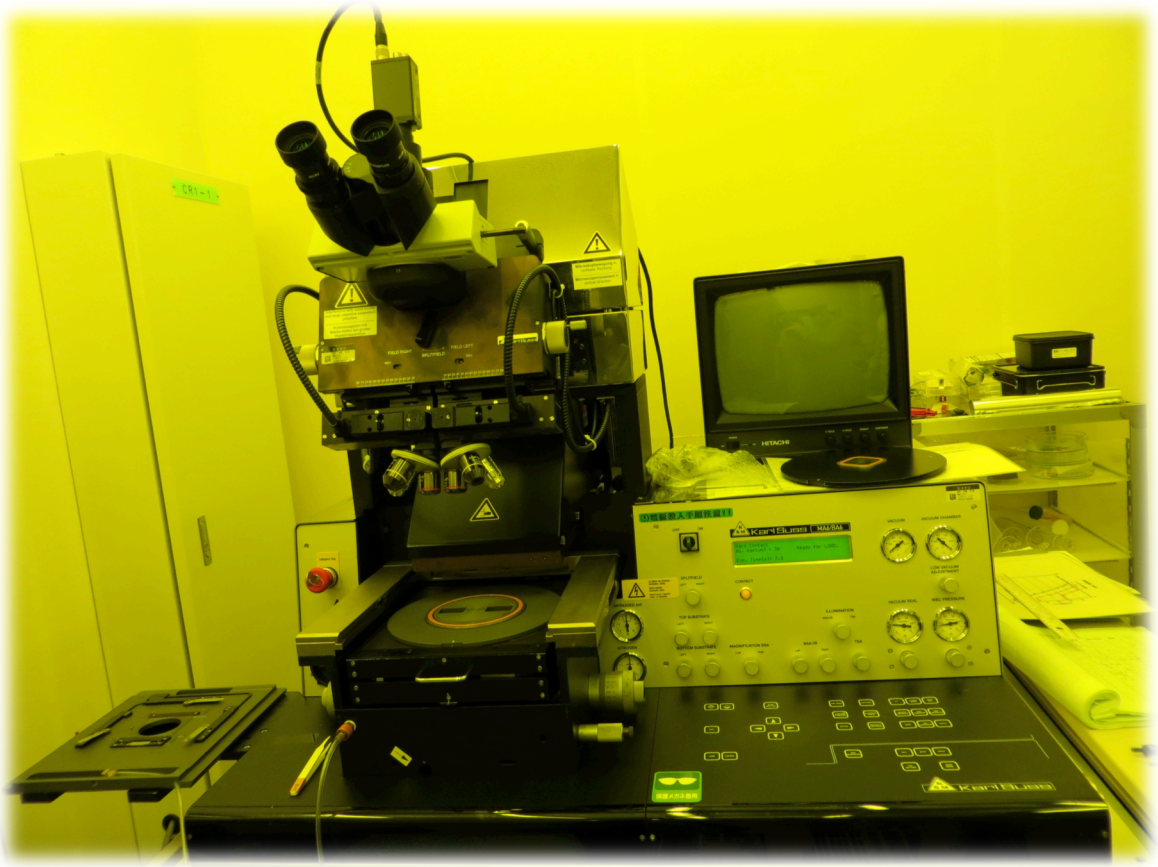

Figure 22. Karl Suss MA6/BA6, UVL system.

It uses light to transfer a geometric pattern from a photomask (Cr/glass) to a light-sensitive chemical "photoresist", or simply "resist," on the substrate. A series of chemical treatments then either engraves the exposure pattern into, or enables deposition of a new material in the desired pattern upon, the material underneath the photoresist.

2.15 Thermal Resistive and Electron Beam (EB) Evaporator System

Evaporation is a common method for thin-film deposition where the source material (metal) is evaporated in a vacuum chamber. The high vacuum creates mean free path and allows vapor particles to travel directly to the target object (substrate), where they condense back to a solid state (**Figure 23**).

Resistive Evaporation. A thermal resistive evaporator uses an electric resistance heater to melt the material and raise its vapor pressure to a useful range. This is done in a high vacuum chamber, both to allow the vapor to reach the substrate without reacting with or scattering against other gas-phase atoms in the chamber, and reduce the incorporation of impurities from the residual gas in the vacuum chamber. Thermal evaporation is the simplest way of depositing material onto a substrate. One major disadvantage of this is that a lot of material is lost in the process.

EB Evaporation. A much 'higher tech' approach to thermal evaporation is to heat the evaporant directly using a focused beam of high-energy electrons. The evaporant sits in a heavy, water-cooled copper hearth and a beam of electrons is

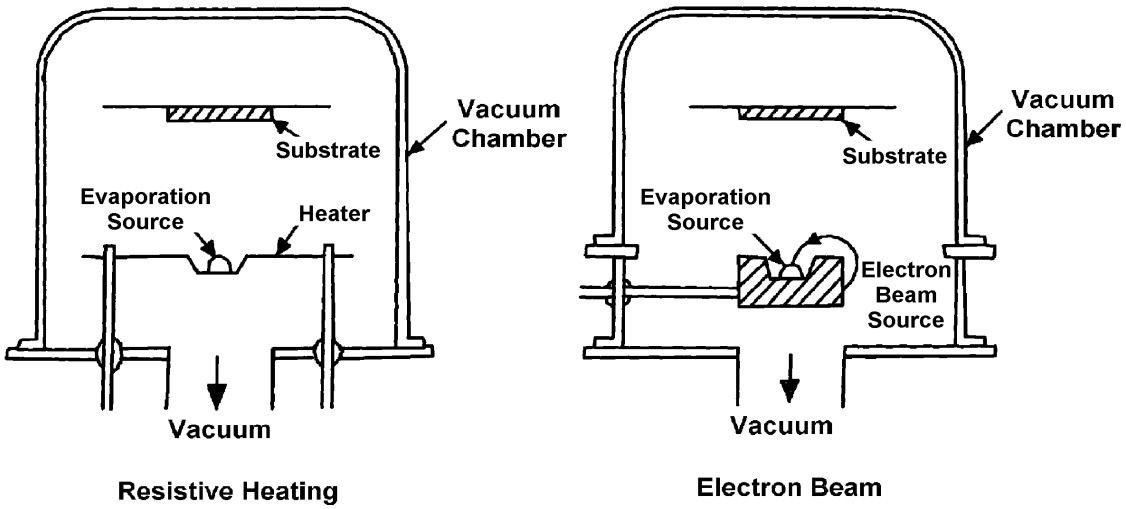

Figure 23. Schematic representation of Resistive and EB Evaporation system.

Figure 24. ULVAC EBV-6DA, Thermal Resistive Evaporator System.

Figure 25. ULVAC EX-550-D10, Electron Beam Evaporator System.

emitted from a filament, usually set below the hearth, is accelerated through an extraction grid and bent through 270° before striking the melt. Heating can be very localized and is not limited by the melting point of a heater element, so even the highest temperature materials such as refractory metals can be evaporated.

2.16 Electrical Conductivity Measurement Protocol

To study the semiconducting behavior of a material, one of the most common nano-device structures studied is the FET. The channel for the nano-FET can be made up of graphene, a carbon nanotube, or nano-wire. Charge transfer from metal to graphene leads to a p-p, n-n or p-n junction [8, 9] depending on the polarity of carriers in the bulk of graphene sheet. The electrical properties of GO and rGO were characterized at room temperature by fabricating the FETs to confirm the extent of GO reduction to graphene. The GO, *H. eurihalina* reduced GO (ERGO) and *H. maura* reduced GO (MRGO)-FETs with source (S), drain (D) and back gate (BG) electrodes were fabricated on 300 nm SiO_2/Si (p-type) wafers using typical EBL technique followed by evaporation and a lift-off process [10]. Briefly, the SiO_2/Si wafers were backside-metalized with 100 nm thick Al using a thermal evaporator system after oxide removal in buffered hydrofluoric acid (BHF) to form BG. The wafers were annealed at 450 °C for 10 min under 90 % N_2 and 10 % H_2 environment to form an ohmic contact between Si and Al. For making large Au electrodes, 50 nm thick Ni was deposited as an adhesive prior to Au deposition. Thermally evaporated Au/Ni (100 nm/50 nm) electrodes followed by the lift-off process in tetrahydrofuran (THF) solution were fabricated to reinforce the contacts. GO, MRGO and ERGO dispersed in DMF (polarity index 6.4) were deposited selectively using spin coating technique on the SiO_2/Si substrate having pre-deposited large Au/Ni electrodes. After identifying suitable samples using an optical microscope and a Raman microscope, EBL was utilized in order to pattern small electrodes (S and D) on the sample. The S and D were fabricated using EBL followed by thermal evaporation of Au/Ti (50/10 nm) and a lift-off process. In order to measure the channel width (w) and length (l) SEM characterizations were performed whereas the thickness (t) was estimated using AFM.

References

1. A. Ulman. *An introduction to Ultrathin Organic Films: from Langmuir-Blodgett to Self-Assembly*, Academic Press, San Diego, CA, **1991**.

2. R.C. Denney, R. Sinclair. *Visible and Ultraviolet Spectroscopy*. *Analytical Chemistry by open learning series*, John Wiley and Sons, USA.
3. Raman Spectroscopy Basics, Princeton instruments, USA.
4. Malvern Instruments Ltd., Zetasizer Nano series user manual-MANO317 issue 2.1, July **2004**.
5. G. Lawes. *Scanning electron microscopy and X-ray microanalysis: Analytical chemistry by open learning*, John Wiley & sons, **1987**.
6. E.N. Kaufmann. *Characterization of materials*, John Wiley & sons, **2003**.
7. A. Meiners, M. Leck and B. Abel, Multiparametr optimization and spectroscopic characterization of a dielectric barrier discharge in N2, Plasma sources Sci. Technol. 18 (2009) 045015.
8. V. V Cheianov, and V. I. Fal'ko. *Phys. Rev. B,* **2006**, *74*, 041403.
9. V. V. Cheianov, V. I . Fal'ko, and B. L. Altshiler. *Science,* **2007** *315*, 1252.
10. K. Nagashio, T. Nishimura, K. Kita, Toriumi. *App. Phy. Lett.* **2010**, *97*, 143514.

3

Green Reduction of GO for Electronics and Bioscience

"There are no such things as applied sciences, only applications of sciences"

- Louis Pasteur

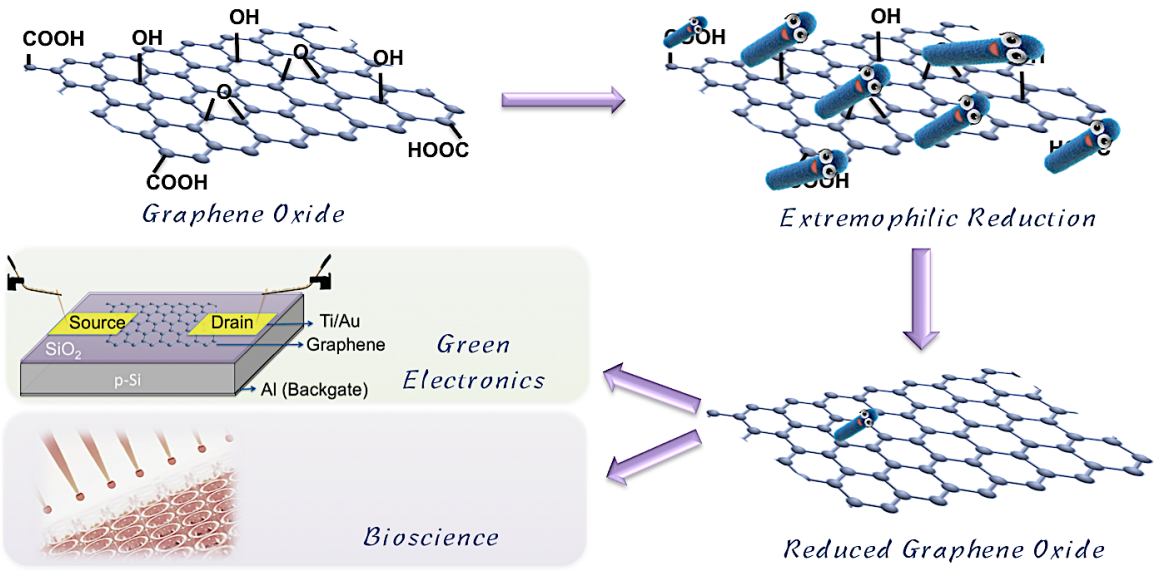

Halophilic bacteria, salt loving extremophiles that can withstand harsh environmental conditions, were demonstrated to be appropriate candidates to effectively replace various toxic chemicals and organic compounds used to reduce GO. We have grown moderately halophilic bacteria *Halomonas eurihalina* and *Halomonas maura* in a medium incorporated with GO. Microbial reduction experiment was performed under two different conditions – aerobic and anaerobic. Biologically reduced GO was characterized using TEM, AFM, XPS and Raman spectroscopy. The electrical properties of GO and reduced GO were characterized at room temperature using three-probe electrical measurement setup by fabricating the FETs to confirm the reduction of GO after interaction with the bacteria.

3.1 Introduction

Graphene has taken the center stage since its discovery in the field of material science due to its outstanding prospects. It is the thinnest known material in the universe and the strongest ever measured. These features have made graphene and graphene derivatives ideal for many potential applications. GO as a precursor for the synthesis of 2D honeycomb structured sp^2 hybridized graphene sheets have gained tremendous attention due to its superior mechanical, thermal, electrical and optical properties [1]. Graphene—the reduced version of GO—is being actively investigated for applications in areas including drug delivery and cellular imaging [2–4] as well as nanoelectronics [5–7], molecular sensors, composite materials, and energy storage [5–11]. In spite of many methods reported for producing graphene sheets, such as mechanical exfoliation of reduced GO (rGO), thermal expansion of graphitic oxide [8–14], and de-oxygenation of GO via chemical reduction [15], a stable, cost-effective and ecofriendly process for producing highly conductive graphene is proving to be elusive.

Conventional methods for the preparation of graphene from dispersions from graphite oxide [16, 17] involve either high temperatures or toxic and unstable gases. Industrial applications necessitate the replacement of these methods by safe and non-toxic means to reduce GO using for example, living biological systems to produce graphene with the appropriate electronic properties. The implementation of such greener, more sustainable alternatives for the synthesis of graphene in large quantities via biological reduction of GO would thus be highly beneficial for a variety of industrial applications. Many green approaches have been reported for ecofriendly reduction of GO using strong alkaline media, [18] tea polyphenol, [19] and so on. In most of these cases, the resultant graphene showed either agglomerated morphology without any stabilizer [20, 21] or poor electrical conduction because of incomplete reduction [22, 23]. Thus, employing a biological system that can produce highly stable, conductive, large-areas of graphene sheets for biomedical and microelectronic applications is of prime motivation for this research.

Recently, there have been several reports on the microbial reduction of GO to produce graphene. Many heterotrophic metal reducing–bacteria both facultative anaerobes and aerobic strains are capable of utilizing various organic compounds as terminal electron acceptors [24–26].

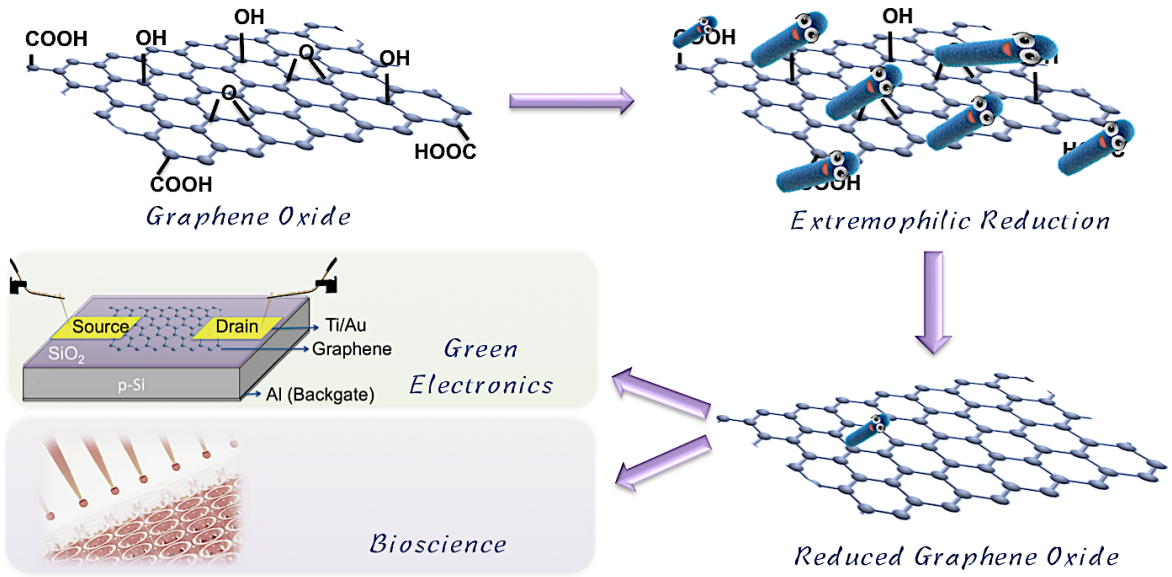

Scheme 1. Schematic representation of extremophilic reduction of GO and its applications.

Extremophiles are microorganisms that can withstand harsh environmental conditions and are capable of effectively degrading toxic chemicals and organic compounds. Here, we have successfully employed two strains of extremophilic bacteria to convert GO to graphene in a growth medium supplemented with two different concentrations of GO via a single step process **(Scheme 1).**

3.2 Synthesis and Bacterial Reduction of GO

GO was prepared by modified Hummer's method using natural graphite powder (Ito Kokuen Co., Ltd, Japan). Briefly, graphite powder was cleaned using $K_2S_2O_8$, P_2O_5 and H_2SO_4 and oxidized in $KMnO_4$ and H_2SO_4. It was washed using 3% HCl aq. and MilliQ water, after overnight sedimentation and the resulting graphite oxide was exfoliated into GO without ultra-sonication [27]. An aqueous dispersion of GO was produced after centrifugation and roughly purified using dialysis to remove residual acids and metal ions. Thus, obtained GO flakes where brownish in color and showed a uniform suspension in water. Two different dilutions of GO were analyzed for the microbial reduction by supplementing it in the bacterial growth medium to show the effect of concentration.

Moderately halophilic bacteria *Halomonas eurihalina* ATCC 49336 and *Halomonas maura* ATCC 700995 were purchased and propagated as per the ATCC product information norms. Inoculums were prepared in MY medium as mentioned elsewhere [28]. Briefly, the medium consist of NaCl, 51.3 g; $MgCl_2.6H_2O$, 9 g;

$MgSO_4.7H_2O$, 13 g; $CaCl_2.2H_2O$, 0.2 g; KCl, 1.3 g; $NaHCO_3$, 0.05 g; NaBr, 0.15 g; $FeCl_3.6H_2O$, traces; Glucose, 10 g; Yeast extract, 3 g; Malt extract, 3 g; Proteose peptone, 5 g; Trace salt solution. Medium was prepared, sterilized and added with GO. First set of serum bottles where supplemented with GO (1 mg/ml) and second set of bottles with ten times diluted GO. Prior to inoculation, serum bottles with medium and GO, were gassed with ultrapure N_2 to remove traces of oxygen. Medium was then inoculated with 1 ml of 48 h cultures of *Halomonas eurihalina* and *Halomonas maura* (OD_{520}=2.5) respectively and incubated at 32 °C in dark conditions. Samples were prepared in duplicates and observed for change in color. Black precipitate was formed in both the set of concentrations, irrespective of the strains inoculated. It was observed that the first set of bottles with 1 mg/ml concentration of GO took comparatively longer time to show graphene precipitation with change in color. Whereas the ten times diluted GO concentrations formed black precipitate within three days of incubation; however, incubation was allowed to continue for 7 days. Also, it was evident that *Halomonas eurihalina* could undergo extensive reduction of GO to graphene within a short span (3-5 days) than *Halomonas maura*, which took much longer (3-7 days). *Halomonas eurihalina* reduced GO (ERGO) and *Halomonas maura* reduced GO (MRGO) were retrieved from the medium by ultracentrifugation (Himac, CF12RX) at 6000 rpm for 20 min. Pellets were washed 2-3 times with ultrapure water, followed by 80% ethanol, ultrapure water, 5 min wash in 1N HCl, ultrapure water and then finally dispersed in 1 ml of ultra pure water [29]. So obtained graphene suspension was used for the characterization studies.

3.3 Electrical and Cytotoxicity Studies

Electrical Conductivity Measurements of GO, ERGO and MRGO.

The electrical properties of GO and rGO were characterized at room temperature by fabricating the field-effect transistors (FETs) to confirm the extent of GO reduction to graphene. The GO, ERGO and MRGO-FETs with source (S), drain (D) and back gate (BG) electrodes were fabricated on 300 nm SiO_2/Si (p-type) wafers using typical electron beam lithography (EBL) technique followed by evaporation and a lift-off process [30]. Briefly, the SiO_2/Si wafers were backside-metalized with 100 nm thick Al using a thermal evaporator system after oxide removal in buffered hydrofluoric acid (BHF) to form BG. The wafers were annealed at 450 °C for 10 min under 90 % N_2 and 10 % H_2 environment to form an ohmic contact between Si and

Al. For making large Au electrodes, 50 nm thick Ni was deposited as an adhesive prior to Au deposition. Thermally evaporated Au/Ni (100 nm/50 nm) electrodes followed by the lift-off process in tetrahydrofuran (THF) solution were fabricated to reinforce the contacts. GO, MRGO and ERGO dispersed in DMF (polarity index 6.4) were deposited selectively using spin coating technique on the SiO_2/Si substrate having pre-deposited large Au/Ni electrodes. After identifying suitable samples using an optical microscope and a Raman spectroscopy, EBL was utilized in order to pattern small electrodes (S and D) electrical contacts on the sample through registration process. The S and D were fabricated using EBL followed by thermal evaporation of Au/Ti (50/10 nm) and a lift-off process. In order to measure the channel width (w) and length (l), SEM characterizations were performed whereas the thickness (t) was estimated using AFM.

In vitro cytotoxicity studies.

Cell Culture. L929, mouse fibroblast cell line was used for testing the *in vitro* cytotoxicity of GO, ERGO and MRGO. L929 cells were cultured and maintained using DMEM, supplemented with 10 % of fetal bovine serum (FBS) at 37 °C in a 5 % CO_2 atmosphere. Cells were sub-cultured after attaining confluent growth and seeded into 96 well plates in the order of 5,000- 8,000 cells/well for testing cytotoxicity [31].

Alamar Blue Assay. Alamar blue assay was performed to detect the percentage of cell viability on the basis of the natural reducing power of the healthy cells, to convert resazurin to a fluorescent molecule, resorufin. Quantification of the cell viability in the presence of GO and rGO will indirectly measure the cytotoxicity caused by the graphene samples. Alamar blue assay was performed as per the standard protocol. L929 cells were grown in 96 well plates for 24 h and treated with varying concentrations (50, 100, 250, 500 and 1000 µg/ml) of GO, ERGO and MRGO to check its biocompatibility towards mammalian cells. Plates were incubated for 24 h and 10 % of alamar blue dye was added to each wells. At the end of incubation, fluorescence was measured at 580-610 nm, using a multi detection microplate reader (Dainippon Sumitomo Pharma, Power scan HT).

Experiment was conducted in triplicates and percentage of cell viability was evaluated using statistical analysis by deducing the mean values and standard error.

3.4 Results and Discussion

The present study offers a green-route for the reduction of GO with extremophiles called Halophiles that are found in salty environments. *Halomonas eurihalina* (ATCC 49336) and *Halomonas maura* (ATCC 700995) are two halophilic bacteria that can grow under controlled salt conditions [32, 33]. Both strains of bacterium were obtained from ATCC and were grown in MY medium. Microbial reduction experiment was performed under both aerobic and anaerobic conditions. For aerobic reduction, the bacteria were grown in a shaking incubator at 32 °C with an agitation speed of 110 rpm for a maximum of 5 days.

However, in the case of anaerobic reduction the bottles were flushed with N_2 gas to remove residual O_2 and create an anaerobic environment before inoculating the bacteria. Then the bottles were incubated in the dark without agitation at 32 °C for 5 days. At the end of incubation GO reduction was clearly seen from the change in the color of the GO in the medium, which changed from brown to a black precipitate settled at the bottom of the bottles (**Figure 1, inset**). It was observed that the anaerobic reduction by *H. eurihalina* is much greater compared to that by the *H. maura* (**Figure 3(a)**). Two different concentrations of GO dispersion were

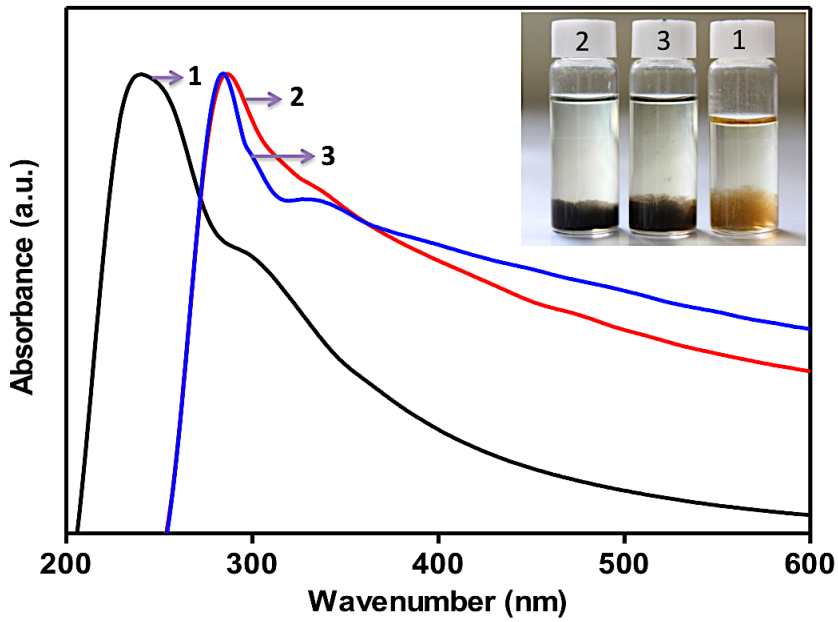

Figure 1. UV-vis spectrum of extremophilic reduction of 10 times diluted concentration of GO, *Curve 1:* GO spectrum; *Curve 2*: ERGO spectrum; *Curve 3*: MRGO spectrum, *inset* shows the (1) GO control, (2) *H. eurihalina* reduced GO and (3) *H. maura* reduced GO.

used to analyze the effect of the concentration in the reduction process. Initially, a concentration of 1 mg/ml and then a ten times diluted concentration were separately inoculated with both the strains of *Halomonas*, respectively. A non-homogeneous brown- black suspension (**Figure 3(b)**) was obtained at the concentration of 1 mg/ml, whereas a ten times diluted concentration showed a uniform black precipitate at the bottom as shown in **Figure 1, inset**. Also, the precipitate formed in the case of *H. maura* was slightly turbid due to the accumulation of the exo-polysaccharides called mauran produced by the strain [34, 35]. The rGO was recovered from the medium and characterized using UV-vis spectroscopy, XPS, TEM, AFM, SEM, Raman spectroscopy, and electrical conductivity measurement.

The reduction of GO was first monitored by UV-visible spectroscopy. **Figure 1 (curve 1)** shows that the optical absorption of GO is characterized using a strong absorption peak at ~ 240 nm corresponding to π −> π* transition of the aromatic C−C bond and a shoulder at ~300 nm is attributed to n −> π* transitions of C=O bonds [36]. While after the reduction of GO by *H. eurihalina* and *H. maura*, the peak is red-shifted to 286 nm and 284 nm respectively (**Figure 1, curve 2 and 3**), which can be assigned to the partial restoration of the π-network between the sheets due to the removal of oxygen containing bonds resulting in electronic conjugations within the graphene sheets [37, 38]. As suggested by Merino *et al*, [18] the maximum red-shift value can be used as a yardstick to estimate the performance of the reducing agent using which the efficiency of various reducing agents can be estimated.

UV-vis spectroscopy gives an average reflection about the degree of reduction. To further explore the details, XPS was employed to analyze the level of reduction. Purified rGO on XPS analysis revealed the amount of the de-oxygenation taken place during bacterial reduction (**Figure 2**). C 1s spectra obtained from ERGO and MRGO exhibit three different characteristic bonds: C−C (284 eV), carboxyl bond (O=C−O)(288 eV), and epoxide/hydroxyl bond (C−O)(285 eV) [24, 39]. C−C peak intensity increased from GO to rGO, which confirms the successful anaerobic reduction of GO by *Halomonas*. Aerobically rGO also showed a considerable rate of de-oxygenation (**Figure 3 (c and d)**), however, the intensity of C−O bond was remain high even after reduction. This can be attributed to the lower degree of reduction occurred in an atmosphere supplied with O_2. Structural characterization of the rGO was subsequently performed using TEM and AFM studies.

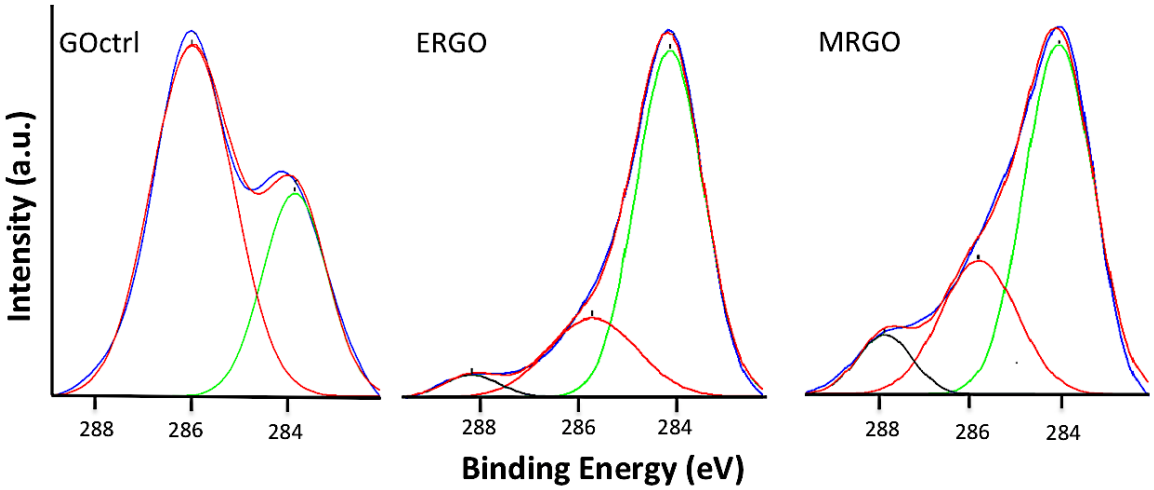

Figure 2. XPS analysis spectrum for C 1s- After anaerobic GO reduction.

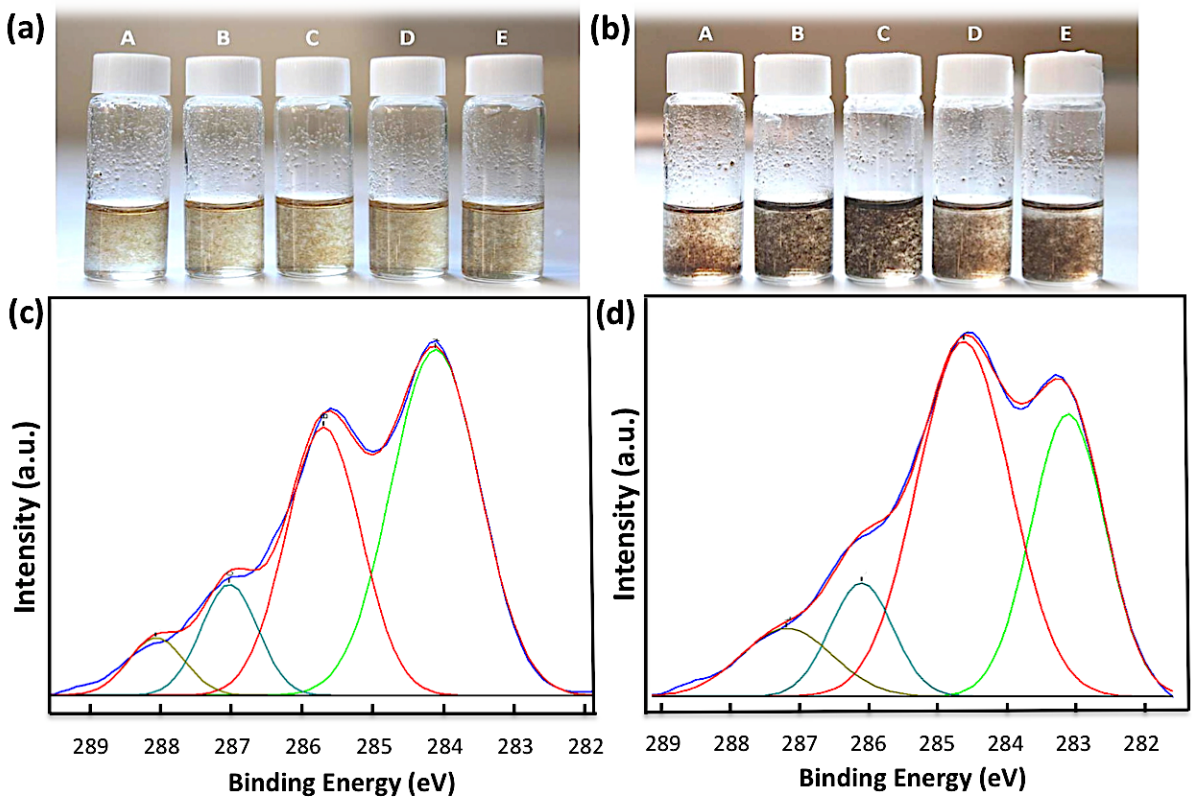

Figure 3. GO reduction at 1 mg/ml concentration- **(a)** Image taken immediately after bacterial inoculation (0 hr); **(b)** Image taken after 10 days of incubation. (A- GO- Control; B & C- ERGO; D & E- MRGO). **(c and d)** XPS analysis spectrum for C 1s- after aerobic GO reduction of ERGO and MRGO respectively.

TEM images obtained for rGO shows uniform graphene sheets with single to few layer thicknesses. **Figure 4(a)** shows the TEM image of ERGO with its selected area electron diffraction (SAED) pattern in the inset. The diffraction pattern of the rGO clearly shows the crystalline order of the 6 membered ring of graphene. It is also evident that the striated appearance of the individual spots may be due to the folding of the monolayer graphene sheet.

Further analysis using Raman spectroscopy confirmed that a significant amount of reduction had occurred during bacterial growth and metabolism. A uniform layer of rGO or GO was analyzed using a 514 nm laser line. Herein, the Raman spectrum of GO (**Figure 4b-(a))** shows the G band broadened due to the presence of isolated double bonds [40], whereas the D band becomes prominent, indicating the reduction in size of the in-plane sp^2 domains due to the extensive oxidation. Raman spectra of the rGO sheets (**Figure 4b (b and c))** also exhibits an upward shift in G band and downward shift in D band (**Table 1**) with similar intensities indicating that the film consists of sp^2 carbon with a number of defects. It is known that the position of the G-band increases with decreasing in number of layers [41]. However, the appearance of 2D peaks at ~ 2652 cm^{-1} and ~ 2685 cm^{-1} (**Figure 4b-(b & c)),** respectively, suggesting the presence of single and double layer graphene [42]**.** Band D+G which is due to the combination of an optical

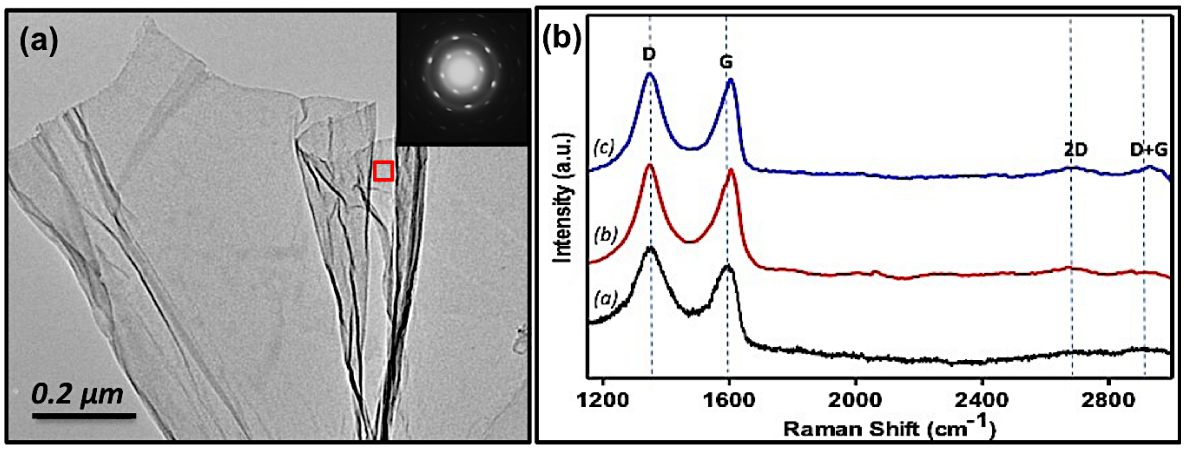

Sample Code	Peak D (cm^{-1})	Peak G (cm^{-1})	I(D)/I(G)
GOctrl	1356.58	1585.92	1.24
ERGO	1347.90	1605.45	1.04
MRGO	1348.30	1604.46	1.05

Figure 4. (a) TEM image of ERGO with diffraction pattern (*inset*) and **(b)** Raman spectra: a) GO control, b) ERGO, and c) MRGO. Table 1.

and acoustical mode at ~ 2920 cm^{-1} indicates the presence of single layer, disordered and randomly arranged graphene sheets. This result is consistent with the work reported previously by Liu *et al* [37]. The intensity ratio of the D band to the G band (gives an indication regarding the number of defects present in the samples) decreases as we go from GO to ERGO and MRGO suggesting a partial restoration of the basal planes and an improvement in the graphitized structure of the graphene due to the reduction process. This is also supported by the shift in the positions of the D and G bands, as indicated in the **Figure 4, Table 1. Figure 5** shows the TEM images of MRGO and ERGO with single to multi-layer thickness. AFM images of the homogenous suspension of ERGO and MRGO on a SiO_2/Si wafer were recorded. Uniformly spread rGO on SiO_2/Si was dried under vacuum at room temperature and viewed under non-contact AFM mode. The cross-sectional view of the ERGO (**Figure. 6(a)**) and MRGO (**Figure. 6(b)**) images shown demonstrates that the average thickness of the RGO sheets are ~ 2.7 nm and ~ 1.7 nm respectively. Thus, suggesting a double to triple layered graphene sheet [43, 44].

To measure the electrical properties of ERGO and MRGO, we developed FETs with these materials. Charge transfer from metal to graphene leads to p-p, n-n or p-n junction [45, 46] in graphene depending on the polarity of carriers in the bulk of graphene sheets. The schematic representation of three-probe electrical measurement setup for the as-fabricated device is illustrated in **Figure 7**.

Figure 8(a-c) shows the SEM images of selected areas used for the electrical measurements. The conductivity of graphene mainly relies on the long-range conjugated network of the graphitic lattice [47, 48]. Oxidation breaks the conjugated structure and localizes π-electrons, which results in a decrease of both

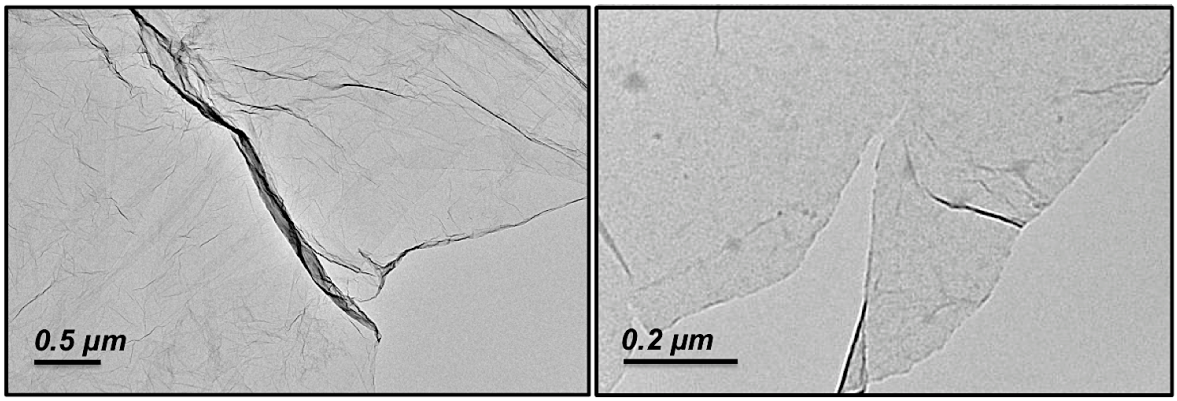

Figure 5. TEM micrographs of RGO **(a)** MRGO, **(b)** ERGO.

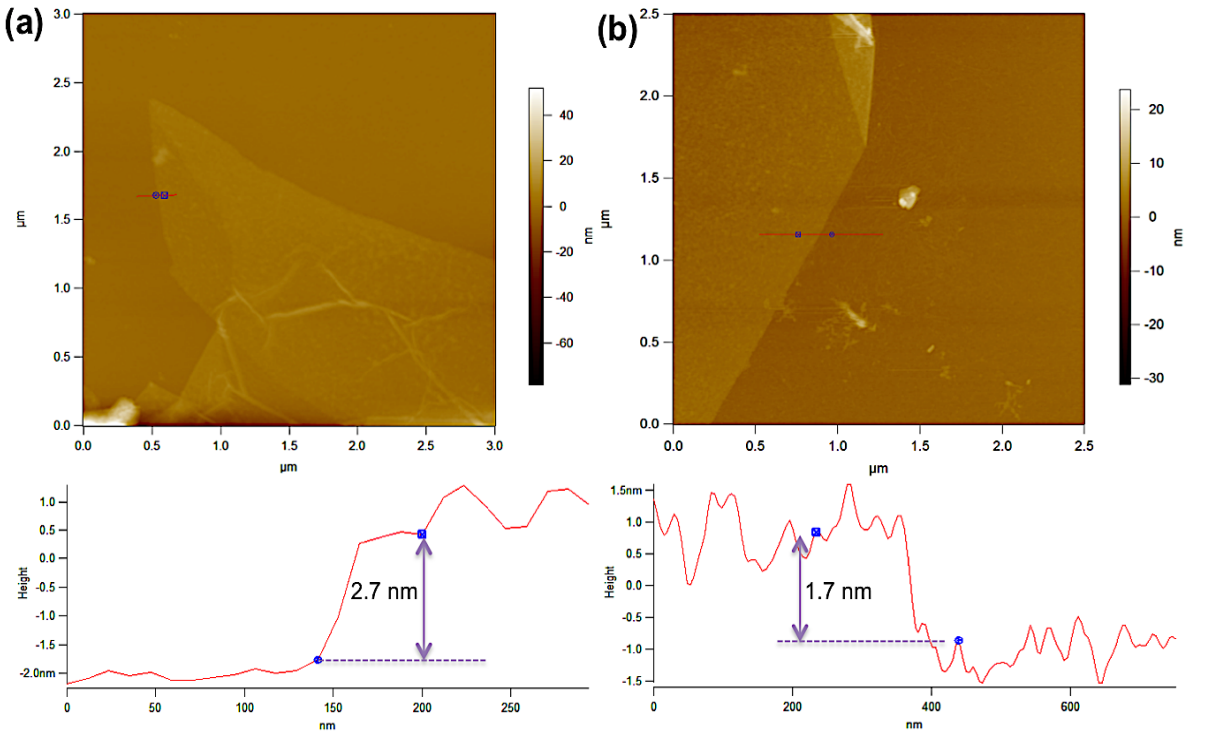

Figure 6. (a) AFM image of ERGO showing average height and **(b)** AFM image of MRGO showing average height.

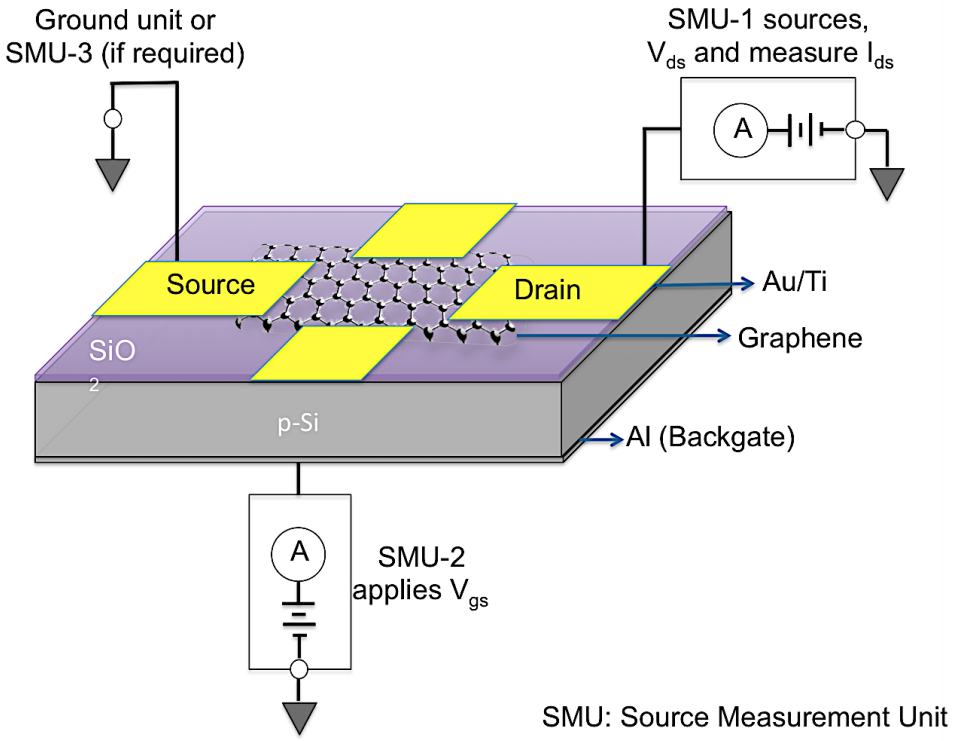

Figure 7. Schematic representation of *I–V* measurement configuration setup for a graphene-based FET.

carrier mobility and carrier concentration. Though there are conjugated areas in GO, long-range (> l μm) conductivity is blocked by the absence of percolating pathways between sp^2 carbon clusters to allow classical carrier transport to occur. To determine the electrical behavior of the samples, V_g was swept in nominal increments (-20, -10, 0, 10 and 20 V) and held constant while the V_{ds} was swept and I_{ds} was measured, resulting in a set of characteristic dc I-V curves for the transistor. **Figure 8(d)** compares the normalized drain current (I_{ds} (l/(w.t)) as a function of V_g that depends on two dimensionless transistor parameters, which are the characteristics 'l' and 'w' of the channel. The current shown was normalizedwith respect to the total channel thickness. The I-V curves were

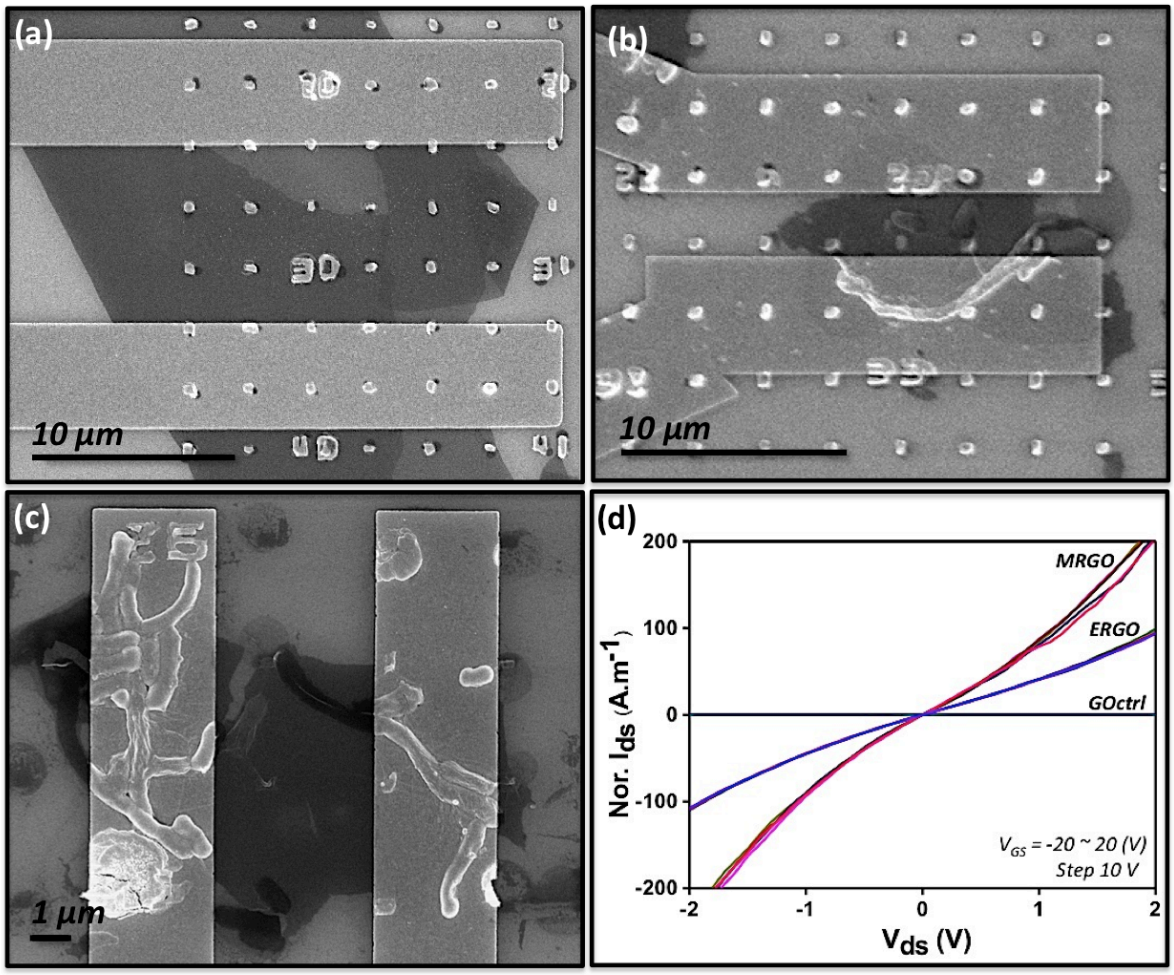

Figure 8. SEM image of FETs with channels as A) GOctrl, B) MRGO, and C) ERGO. D) The normalized I_{ds} versus V_{gs} for GOctrl, MRGO, and ERGO measured at room temperature for various gate biases (V_{gs} = −20 V, –10, 0 V, +10 V, and +20).

approximately linear when varied the range of -0.5 to 0.5 V, and the contact resistance between the sheets and the electrode were negligible enough to discuss the electrical properties of samples. In contrast to this, the as-synthesized GO sheets behaved like an insulator. Using the slope of the lines in I–V graph, resistivity of GO was estimated to be 3 × 103 Ω-m. However, after reduction the resistivity value remarkably decreased to 1.3×10^{-2} Ω-m and 2.5×10^{-2} Ω-m for MRGO and ERGO respectively. This is due to as the partial restoration of graphitic structure. An increase of 10^4-10^5 fold in the conductivity of rGO from GO attributes the removal of oxygen-related functional groups and creation of conducting pathways. These observations agree well with the chemically converted graphene sheets [1]. It was observed that the bacterial cells as such could not impart any significant enhancement in the value of conductivity.

Biocompatibility of ERGO and MRGO was demonstrated using alamar blue assay. **Figure 9** represents the viability of L929, mouse fibroblast cells under various concentrations of GO and rGO. It is evident from the graph that the cell viability increases as the concentration of ERGO and MRGO goes up from 50 µg to 1000 µg. Where as in the

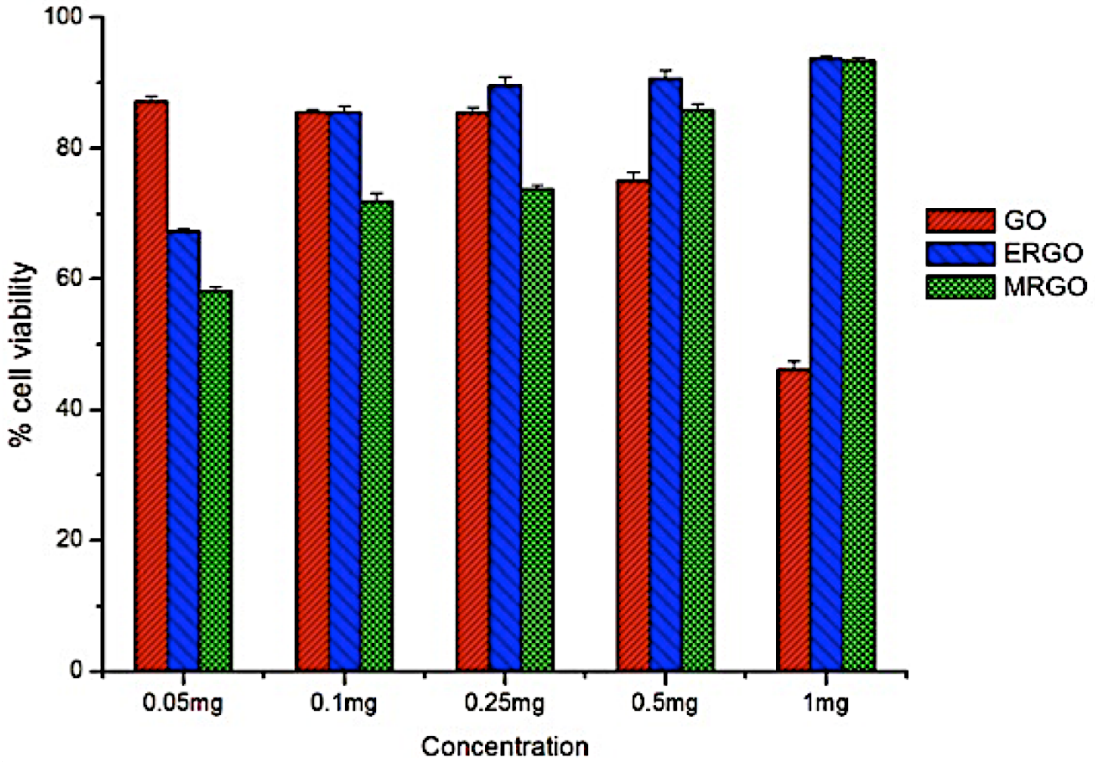

Figure 9. Cytotoxicity assay results showing the viability of L929 cells under various concentrations of GO, ERGO and MRGO.

GO the cell viability decreases as the concentration increases with a maximum observed viability of 46%. Furthermore, it was observed that the presence of ERGO and MRGO is enhancing the cell growth; this may be due to the presence of bacterial exo-polysaccharides bound to rGO [32].

3.5 Conclusion

In conclusion, we have demonstrated a feasible, cost-effective ecofriendly approach for the bulk reduction of GO to produce graphene with high electrical conductivity and large surface area. A key aspect in extremophilic reduction of GO is to enhance the reduction rate under controlled conditions like absence of oxygen and to make it a viable candidate for use in graphene based hybrid biomaterials. This prototype not only avoids the use of toxic reagents but also offer a great deal of flexibility for various potential applications. Bacterial mediated method requires only a loop full of inoculum to carryout a significant level of reduction in comparison to other chemical modes, where a bulk concentration of reducing agent is required. Ecofriendly reduction of GO gives an insight of its tolerance and acceptance by a biological system since it doesn't hamper the growth of fibroblast cell lines under *in vitro* conditions. Hence it could definitely be used for several green electronics and bioscience applications. Moreover, the low cost and large production scale of RGO is unmatched with any other mode of ecofriendly reduction. We believe that the present strategy would greatly contribute to the graphene electronics as well as the biological applications, the most promising areas of graphene.

References

1. S. Gilje, S. Han, M. Wang, K. L. Wang, R. B. Kaner, , *Nano Letters* **2007,** *7*, 3394.
2. X. Sun, Z. Liu, K. Welsher, J. T. Robison, A. Goodwin, S. Zaric, H. Dai, *Nano Res.* **2008**, *1*, 203.
3. Z. Liu, J. T. Robinson, X. Sun, H. Dai, *J. Am. Chem. Soc.* **2008**, *130*, 10876.
4. J. Peng, W. Gao, B. K. Gupta, Z. Liu, R. Romero- Aburto, L. H. Ge, L. Song, L. B. Alemany, X. B. Zhan, G. H. Gao, S. A. Vithayathil, B. A. Kaipparettu, A. A. Marti, T. Hayashi, J. J. Zhu, P. M. Ajayan, *Nano Lett.* **2012**, *12*, 844.

5. W. H. Lee, J. Park, Y. Kim, K. S. Kim, B. H. Hong, K. Cho, *Adv. Mater.* **2011**, *23*, 3460.
6. W. H. Lee, J. Park, S. H. Sim, S. B. Jo, K. S. Kim, B. H. Hong, K. Cho, *Adv. Mater.* **2011**, *23*, 1752.
7. J. Park, S. B. Jo, Y.-J. Yu, Y. Kim, J. W. Yang, W. H. Lee, H. H. Kim, B. H. Hong, P. Kim, K. Cho, K. S. Kim. *Adv. Mater.* **2012**, *24*, 407.
8. A. K. Geim, K. S. Novoselov, *Nat. Mater.* **2007**, *6*, 183.
9. A. K. Geim, *Science* **2009**, *324*, 1530.
10. C. N. R. Rao, K. Biswas, K. S. Subrahmanyam, A. Govindaraj, *J. Mater. Chem.* **2009**, *19*, 2457.
11. C. N. R. Rao, A. K. Sood, K. S. Subrahmanyam, A. Govindaraj, *Angew. Chem.* **2009**, *48*, 7752.
12. M. J. Allen, V. C. Tung, R. B. Kaner, *Chem. Rev.* **2010**, *110*, 132.
13. K. P. Loh, Q. Bao, P. K. Ang, J. Yang, *J. Mater. Chem.* **2010**, *20*, 2277.
14. G. Eda, M. Chhowalla, *Adv. Mater.* **2010**, *22*, 2392.
15. S. Stankovich, D. A. Dikin, R. D. Piner, K. A. Kohlhaas, A. Kleinhammes, Y. Jia, Y. Wu, S. T. Nguyen, R. S. Ruoff, *Carbon* **2007**, *45*, 1558.
16. S. Park, R. S. Ruoff, *Nat. Nanotechnol.* **2009**, *4*, 217.
17. S. Park, J. An, I. Jung, R. D. Piner, S. J. An, X. Li, A. Velamakanni, R. S. Ruoff, *Nano Lett.* **2009**, *9*, 1593.
18. M. J. Fernandez-Merino, L. Guardia, J. I. Paredes, S. Villar-Rodil, P. Solís-Fernandez, A. Martínez-Alonso, J. M. D. Tascon, *J. Phys. Chem. C* **2010**, *114*, 6426.
19. Y. Wang, Z. X. Shi, J. Yin, *ACS Appl. Mater. Interfaces* **2011**, *3*, 1127.
20. V. Dua, S. P. Surwade, S. Ammu, S. R. Agnihotra, S. Jain, K. E. Roberts, S. Park, R. S. Ruo, S. K. Manohar, *Angew. Chem.* **2010**, *49*, 2154.
21. M. Fang, J. Long, W. Zhao, L. Wang, G. Chen, *Langmuir* **2010**, *26*, 16771.
22. C. Zhu, S. Guo, Y. Fang, S. Dong, *ACS Nano* **2010**, *4*, 2429.
23. J. Liu, S. Fu, B. Yuan, Y. Li, Z. Deng, *J. Am. Chem. Soc.* **2010**, *132*, 7279.
24. E. C. Salas, Z. Sun, A. Luttage, J. M. Tour, *ACS Nano* **2010**, *4*, 4852.
25. G. Wang, F. Qian, C. W. Saltikov, Y. Jiao, Y. Li, *Nano Res.* **2011**, *4*, 563.
26. O. Akhavan, E. Ghaderi, *Carbon* **2012**, *50*, 1853.
27. W. S. Hummers and R. E. Offeman, *J. Am. Chem. Soc.* **1958**, *80*, 1339

28. S. Arias, A. Del Moral, M. R. Ferrer, R. Tallon, E. Quesada, V. Bejar, *Extremophiles* **2003**, *7*, 319.
29. E. C. Salas, Z. Sun, A. Luttage, J. M. Tour, *ACS Nano* **2010**, *4*, 4852.
30. K. Nagashio, T. Nishimura, K. Kita, Toriumi. *App. Phy. Lett.* **2010**, *97*, 143514.
31. S. Raveendran, A. C. Poulose, Y. Yoshida, T. Maekawa, S. Kumar, *Carbohydr. Polym.* http://dx.doi.org/10.1016/j.bbr.2011.03.031.
32. S. Raveendran, A. C. Poulose, Y. Yoshida, T. Maekawa, S. Kumar, *Carbohydr. Polym.* **2013**, *91*, 22.
33. S. Raveendran, B. Dhandatuthapani, Y. Nagaoka, Y. Yoshida, T. Maekawa, S. Kumar, *Carbohydr. Polym.* **2013**, *92*, 1225.
34. S. Arias, A. D. Moral, M. R. Ferrer, R. Tallon, E. Quesada, V. Bejar, *Extremophiles* **2003**, *7*, 319.
35. S. Raveendran, Y. Yoshida, T. Maekawa, S. Kumar, *Nanomedicine: NBM.* **2013**, DOI: 10.1016/j.nano.2012.12.006.
36. D. A. Skoog, F. J. Holler, T. A. Nieman, *Principles of Instrumental Analysis*, Hartcourt Brace & Company, Philadelphia **1998**, Ch. *13*.
37. K. Liu, J.-J. Zhang, F.-F. Cheng, T.-T. Zheng, C. Wang, J.-J. Zhu, *J. Mater. Chem.* **2011**, *21*, 12034.
38. X. Fan, W. Peng, Y. Li, X. Li, S. Wang, G. Zhang, F. Zhang, *Adv. Mater.* **2008**, *20*, 4490.
39. H. Wang, J. T. Robinson, X. Li, H. Dai, *J. Am. Chem. Soc.* **2009**, *131*, 9910.
40. A. C. Ferrari, *Solid State Commun.* **2007**, *143*, 47.
41. L.-H. Liu, G. Zorn, D. G. Castner, R. Solanki, M. M. Lerner, M. Yan, *J. Mater. Chem.* **2010**, *20*, 5041.
42. K. Nagashio, T. Nishimura, K. Kita, A. Toriumi, *Appl. Phys. Let.* **2010**, *97*, 143514.
43. Y. Xu. H. Bai, Lu. Gewu, C. Li, G. Shi, *J. Am. Chem. Soc.* **2008**, *130*, 5856.
44. K. N. Kudin, B. Ozbas, H. C. Schniepp, R. K. Prud'homme, I. A. Aksay, R. Car, *Nano Lett.* **2007**, *8*, 36.
45. V. V. Cheianov, V. I. Fal'ko, *Phys. Rev. B* **2006**, *74*, 041403.
46. V. V. Cheianov, V. I. Fal'ko, B. L. Altshiler, *Science* **2007**, *315*, 1252.
47. A. B. Kaiser, *Rep. Prog. Phys.* **2001**, *64*, 49.
48. Y. Kopelevich, P. Esquinazi, *Adv. Mater* **2007**, *19*, 4559.

4

Synthesis of Large Area GO and its Organization at Air-Water Interface using LB Technique

"Imagination is more important than knowledge "
- Albert Einstein

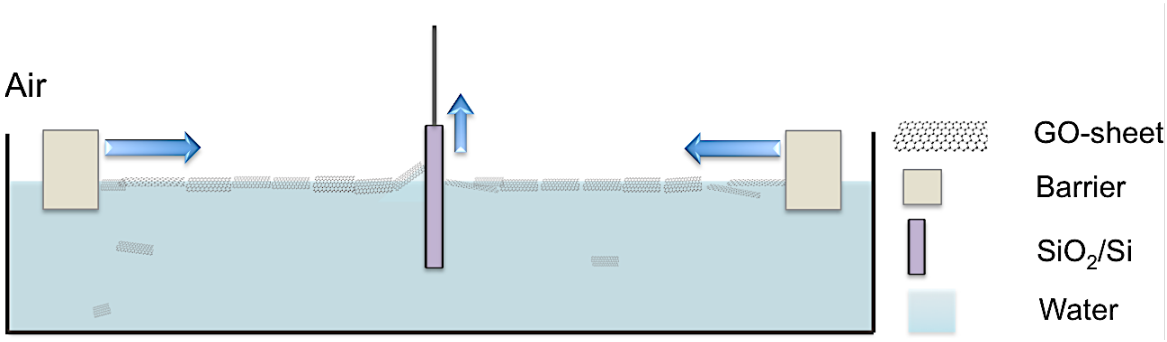

The work presented in this chapter focuses on the synthesis of large-area GO in aqueous medium using modified Hummer's Method with minor modifications. Several parameters like GO solution concentration, its volume and LB parameters were optimized to assemble monolayer GO at air-water interface using the LB technique which could considerably simplify the patterning process.

4.1 Introduction

Graphene has captivated the imagination of millions of researchers since its discovery due to its multifarious nature as it exhibits impressive electronic, mechanical, optical and chemical properties associated with its unique one atomic thick 2D structure [1], which could be utilized for various Bio-Nano-Electronics related applications [2]. Its flexibility makes it an ideal building block for the next generation microscale as well as nanoscale electronic devices. A significant progress has been made in the area of its synthesis to applications [3]. The most widely method used for the preparation of graphene on large scale and at low cost is the reduction of GO. It is normally prepared in the solution form since chemically synthesized GO is simple, inexpensive and exceptionally stable with high-yield. However, from the industrial point of view, a grand challenge still exists to synthesize it as a large area monolayer and its self-assembly for application in diverse areas including electronics, photonics, optoelectronic devices, biological and chemical sensing, energy conversation etc.

Due to the highly anisotropic morphology of GO, properties of the final product are determined not only by the quality of the individual sheets but also how they are assembled. The precise control over the alignment and positioning of graphene-sheets from its stock solution to the substrate is one of the vital steps in the processing of graphene-based devices especially for the large-scale fabrication of parallel device arrays [4]. In order to build nanodevices for practical applications the individual nanoparticles need to be assembled in a desired fashion and much current research interest lies in ordered 2D assembly of nanoparticles. Therefore, controlled assembly of these 2D building blocks is important for both fundamental scientific curiosity and technical applications.

Recently, extensive efforts have been made to achieve continuous films of GO using numerous methods and techniques such as drying of a suspension droplet i.e., via drop casting, spin-coating by means of functionalization [5], vacuum filtration [6], electrophoretic deposition [7], dip-coating [8], layer by layer assembly [9] and LB [10] for transparent electronics and bio-electronics applications. However, general thin-film preparation methods such as drop-casting, spraying, or spin-coating usually results in multilayer aggregates and crumpled sheets due to uncontrolled capillary flow and de-wetting due to solvent evaporation, which forces the soft sheets to fold and wrinkle. Among numerous methods reported to prepare the 2D assembly of graphene and GO as discussed in *Chapter 1*, LB assembly is the

only technique to realize controllable, wrinkle free, high density, close-packed monolayers of GO in layer-by-layer manner with large-scale deposition and without the need of any stabilizing agent [11]. The thickness of GO film can accurately be controlled upon repeated deposition, leading to optimized optical and electrical properties of the final product. It is important to mention that the substrate size is virtually unlimited since the dimension of the LB trough is the only restricting factor for large-scale film deposition. In this method, film comprises of a monolayer of amphiphilic molecules supported on a water subphase and molecular density of monolayer can readily be tuned based on the initial concentration of GO solution and finally aligned by mechanically compressing or expanding the barriers. The thin film performed in such a way can then be transferred onto a substrate either by vertical dipping or horizontal dipping. This simple and general process has led to various applications based on mono and multilayer films of graphene [12]. The degree of control over the molecular level organization of amphiphiles and ions that can be exercised at the air-water interface, makes LB a versatile technique.

The large area synthesis and 2D ordered assemblies of GO is a technologically imperative problem that has not received sufficient attention. Here, we introduce a modified protocol for the synthesis and assembly of large area GO to control the edge density of GO sheets that can significantly affect the conductivity of rGO as the in-plane conductivity of rGO films is higher than that in the vertical direction. The synthesis of large area GO sheets as the initial step could be an efficient approach that can result in reduced intersheet tunneling barriers and therefore lower overall resistance. Usually, the sonication process performed during exfoliation process leads to insignificant reduction in the size of GO. To avoid such problems, we have employed several centrifugation steps to delaminate graphite oxide. Our approach thus offers a great deal of flexibility in the creation of GO and rGO films. This facile and inexpensive procedure is of great significance not only for the future of large area electronics but also for bioengineering applications.

4.2 Synthesis of Large-Area GO

Material Preparation.

Natural graphite (NG) flakes were a kind gift from Ito Kokuen Co., Ltd, Japan. Sulfuric acid (H_2SO_4), sodium nitrate ($NaNO_3$), potassium permanganate ($KMnO_4$), 30% hydrogen peroxide (H_2O_2), Hydrochloric acid (HCl) were procured from

Kanto Chemical Co., Inc. All chemical were used as received unless otherwise stated.

Preparation of Large-Area GO sheets.

GO sheets were prepared by modified hummer's method from ~ 600 µm NG flakes [13] with slight modifications. No pretreatment of graphite was applied. Briefly, NG flake (1 g) and $NaNO_3$ (0.5 g) were dispersed in concentrated H_2SO_4 (24 mL). The dispersion was cooled by ice to about ~5 °C. After that, over a period of three hours $KMnO_4$ (3.0 g) was added in small portions and the dispersion was stirred for additional three hours at 35 °C. The reaction mixture was then poured on ice (500 mL) and H_2O_2 (10 mL, 30%) was added drop-wise until gas evolution was completed. The obtained graphite oxide was purified by repeated centrifugation with 5% HCl. The product is washed by centrifugation with Millipore water extensively until the pH stabilizes at ~ 5.5. No sonication was applied throughout the process to eliminate formation of pinholes and breakage of the GO sheets [14]. During washing, a significant viscosity change was observed, indicating the occurrence of exfoliation. Finally, the GO suspension was purified by dialysis for at least 2-3 week to remove heavy metal ions and adjust the pH. To determine the final concentration of GO in aqueous solution, 5 ml of GO suspension was freeze-dried and dry content was weighed. The final concentration of GO was found to be 1.45 mg/ml.

4.3 Assembly of GO at Air-Water Interface

Preparation of LB Films.

For the preparation of LB films, 0.1 mg/ml concentration of GO solution was prepared in stock and all the suspension were centrifuged @ 2500 rpm for 20 min in order to remove few or multilayer graphene-oxide, if any. Methanol was used to form a stable GO solution with a final ratio of 1:5 (water/methanol) to enable rapid spreading on the surface of de-ionized (DI) water subphase [15, 16]. Before performing each experiment, LB trough and barriers were cleaned with ethanol and thoroughly rinsed with DI water in order to avoid any contamination.

Initially, isotherm for GO solution was taken by dropping various solution volumes (1 ml, 2 ml, 3 ml, 4 ml and 5 ml @ ~ 100 µl/min) using a glass micro-syringe at the water surface. After stabilizing it for ~ 30 min the film was compressed by the barriers at a speed of 5 mm/min and the surface pressure (SP) was recorded using tensiometer attached to the Wilhelmy's plate.

Once the solution volume was optimized based on the desired value of trough area with respect to SP, vertical dipping was performed to transfer monolayer GO-film on N_2-plasma treated SiO_2/Si substrates at various SP to monitor change in the assembly of GO-sheets. It is worth noting that for the dipping of N_2-plasma treated SiO_2/Si substrate; the first cycle was executed beneath the subphase because of its hydrophilic nature. At least 20 minutes were allowed for solvent evaporation and the monolayer was compressed at different values of SP to yield tightly packed monolayer film of GO while pulling it upward out of the solution at the rate of 0.5 mm/min. Once the deposition was achieved, the samples were air-dried and used for further characterization.

4.4 Results and Discussion

One of the fastest and easiest ways to characterize GO sample is to observe the optical properties by UV-vis spectroscopy and optical microscopy (**Figure 1**). A well-dispersed GO aqueous solution (**Figure 1(a)**, **inset**) was further diluted to take the absorption spectra, **Figure 1(a)** shows a sharp and a strong absorption band centered at ~ 229 nm which is ascribed to the $\pi \rightarrow \pi^*$ transition of aromatic C=C (conjugation) with a shoulder at 300 nm, which attributed to the $n \rightarrow \pi^*$ transitions of the C=O bond [17].

We have synthesized large-area GO to reduce the intersheet tunneling barriers and thus the resistance while maintaining the sp^2 conjugated carbon network at same transmittance which is highly desirable for fundamental research and technological applications of graphene [18]. The surface morphology of GO

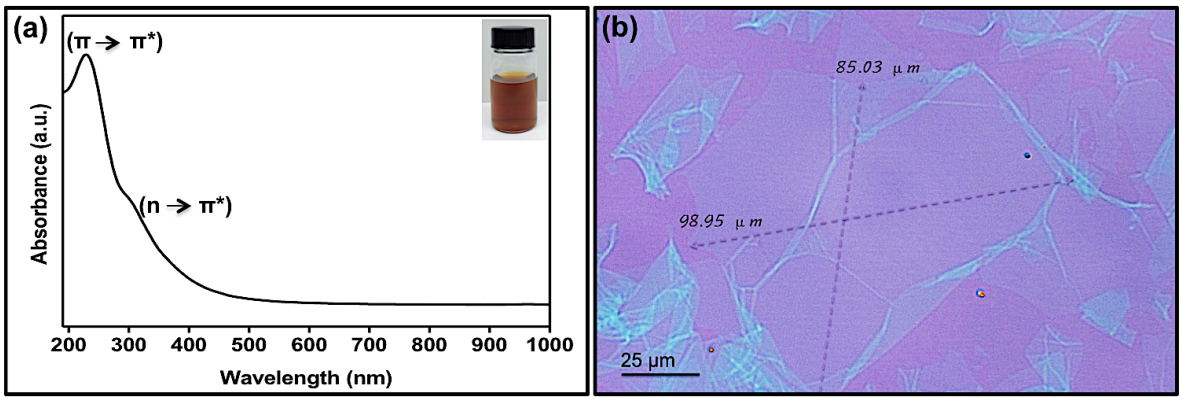

Figure 1. (a) UV-Vis absorption spectra of aqueous GO solution, *inset* shows the as prepared GO solution of 1.45 mg/ml concentration and **(b)** Optical image of GO.

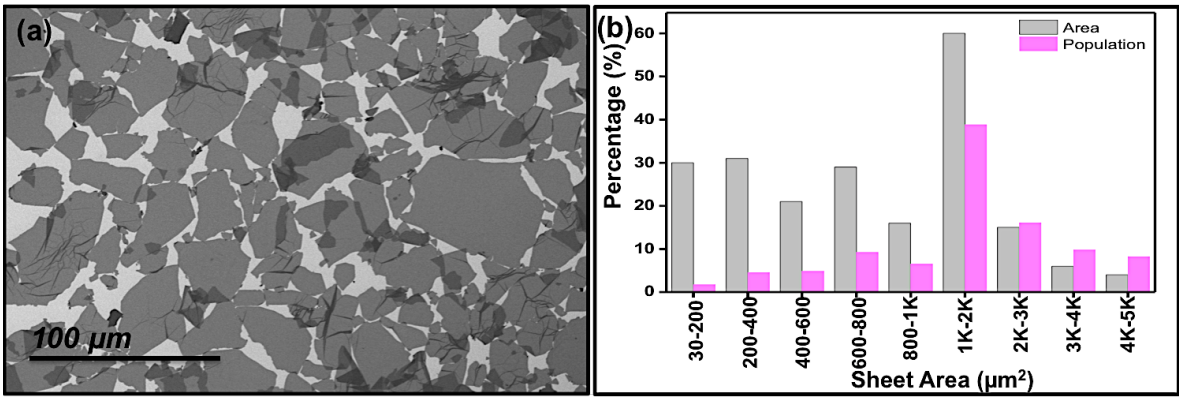

Figure 2. (a) SEM image of as synthesized monolayer GO sheets and **(b)** size distribution of GO sheets deduced from the SEM images.

sheets was studied by SEM analysis and a representative image is shown in **Figure 2(a)**. Most of the ultra large GO sheets appear to be single layer, which can be further affirmed by the AFM and TEM analysis. It is worth noting that the size of GO sheets can simply be reduced through ultra-sonication technique, if required.

By analyzing various SEM images the size distribution of GO sheets along with their population was estimated and shown in **Figure 2(b)**. The size distribution of the GO sheets ranges from ~ 30 to 5000 μm^2 with a mode of area as 1016 μm^2.

In order to study the surface properties of GO and to determine the nature functional groups on it, an FTIR-ATR spectrum was recorded (**Figure 3 (a)**). The broad peak around 3400-3200 cm^{-1} regions is assigned to the O−H stretching vibrations of free water, associated hydroxyl groups in GO and adsorbed water molecules. The peak at ~ 1728 cm^{-1} represents the stretching mode of carbonyl (C=O) bonds in both ketone and carboxylic acid groups. The intense peak at

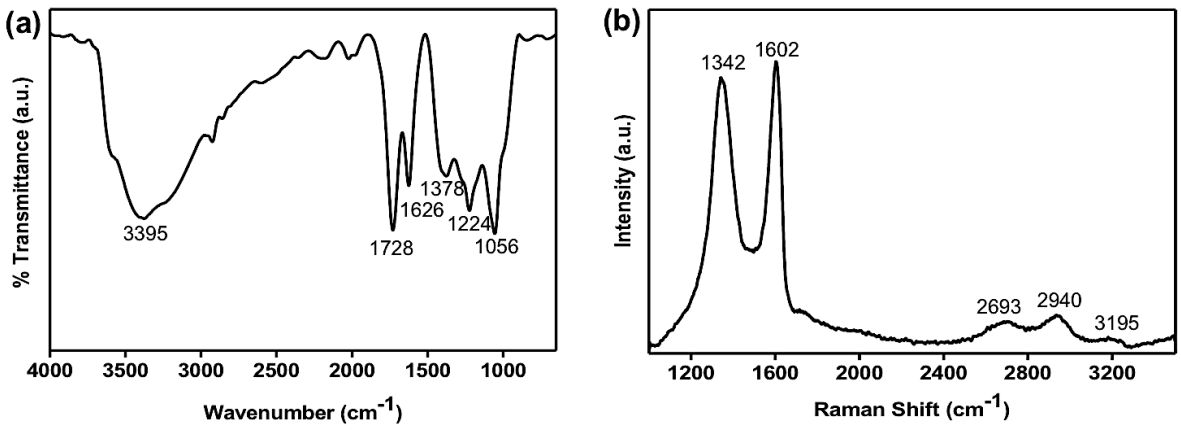

Figure 3. (a) ATR-FTIR spectra and **(b)** Raman spectra of GO at an excitation wavelength of 514 nm.

~ 1626 cm^{-1} is attributed to the bending mode of water molecules while the broad peak embedded at ~ 1378 cm^{-1} corresponding to tertiary alcohol bending. The peak at ~ 1224 cm^{-1} represents an asymmetric stretching mode of the epoxy (C-O-C) group. Lastly, the peak at ~ 1056 cm^{-1} is characteristic of alkoxy (C-O) vibrations [19].

The structure of GO is characterized using Raman Spectroscopy. A Raman spectrum is an effective fingerprint of carbon materials featuring a number of peaks that shows the intensity and wavelength of the raman scattered light. These phonons are the characteristics of a given material and enable its chemical and structural properties to be investigated.

Raman spectroscopy can provide a wide range of information on the material properties of graphene and its derivatives, from its identification to the number of layers and level of disorders on standard SiO_2/Si substrate [20]. The G-band mainly occurs at all sp^2 sites in GO. As depicted in **Figure 3(b)** it appears at ~ 1602 cm^{-1} and is caused due to distortion of honeycomb lattice of graphene by oxygen functionalities as a result of an in-plane bond stretching of sp^2-hybridised carbon bond pairs [21]. The peak at ~ 1342 cm^{-1} corresponds to the D-band [22]. The integrated intensity ratio I(D)/I(G) for the D-band and G-band is extensively used for measuring sp^2 cluster sizes within a network of sp^3 and sp^2 bonded carbon, which is found to be < 1 for GO. A weak 2D peak at ~ 2693 cm^{-1} is ascribed to an out-of-plane vibration mode and a combination of the D and G peaks gives rise to a resultant scattering peak, D+G, at ~ 2940 cm^{-1} and the 2G band at 3195 cm^{-1} is induced by disorder [23]. The D and 2D peak positions are dispersive (dependent on the laser excitation energy).

It is noteworthy that the gap between GO sheets and its density can be finely

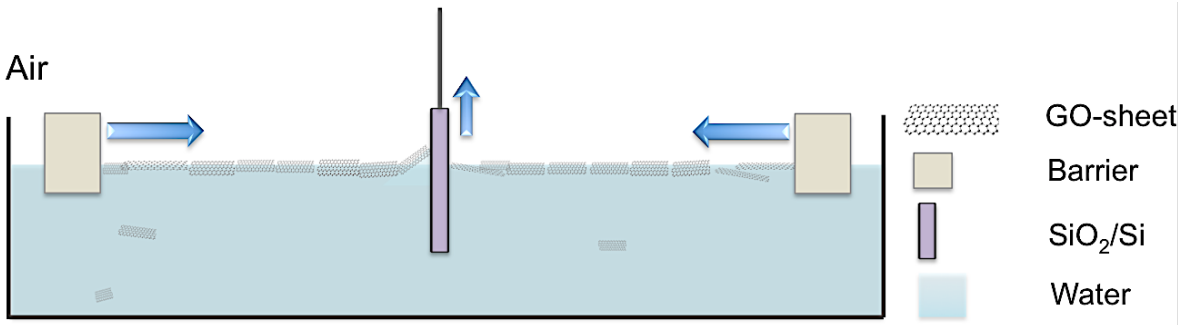

Figure 4. SiO_2/Si substrate dipped in LB trough while the barriers are compressed to reach optimized surface pressure.

through LB deposition technique, where the sheets can be spread on the water surface using a 1:5 water-methanol suspension that leaves behind 2D monolayer GOs floating at the interface due to its amphiphilic nature [24]. **Figure 4** depicts the schematic representation of LB trough where GO can be spread at air-water interface, leaving the sheets trapped between the barriers.

The isotherm for GO solution was taken by dropping various solution volumes (1 ml, 2 ml, 3 ml, 4 ml and 5 ml @ ~ 100 µl/min) and the SP was recorded using tensiometer attached to the Wilhelmy's plate (**Figure 5**). The optimized GO solution volume of 5 ml was utilized throughout the experiment based on the desired value of trough area with respect to SP. The SEM images of GO sheets on N_2-plasma treated SiO_2/Si were collected at various SPs, which shows different packing behaviors.

Figure 6(a) shows the monolayer of isolated flat sheets at a SP of 0.1 mN/m, once the SP reaches to 2.0 mN/m, monolayer of closely-packed GO with a slight overlapping were formed that could have occurred due to the large area of sheets (**Figure 6(b)**). However, on further compression of the barriers, SP increases to 3.5 mN/m and over-packed monolayer with folded, wrinkled and partially overlapped sheets interlocking with each other were observed as shown in **Figure 6(c)**.

To measure the actual topology and thickness of GO sheets deposited on a SiO_2/Si substrate, AFM analysis was performed. The AFM image and height profile

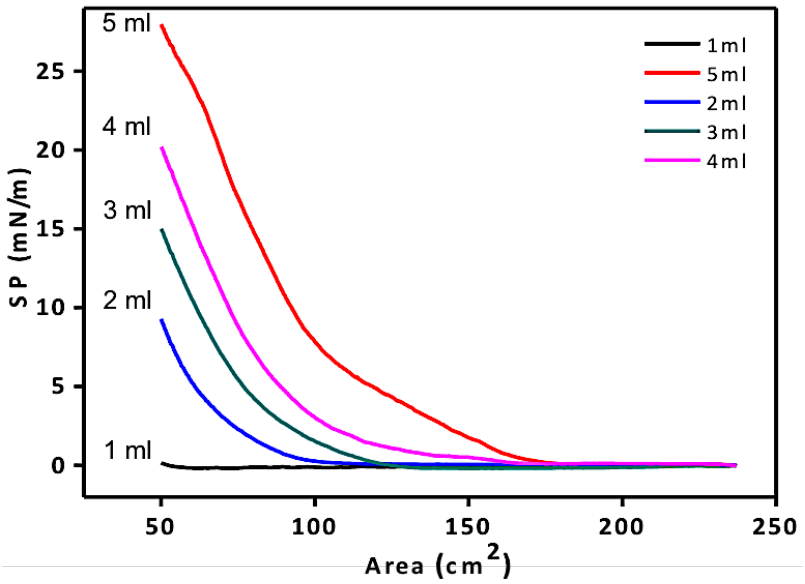

Figure 5. Isothermal SP Vs area plot with increasing solution volume of GO from 1-5 ml.

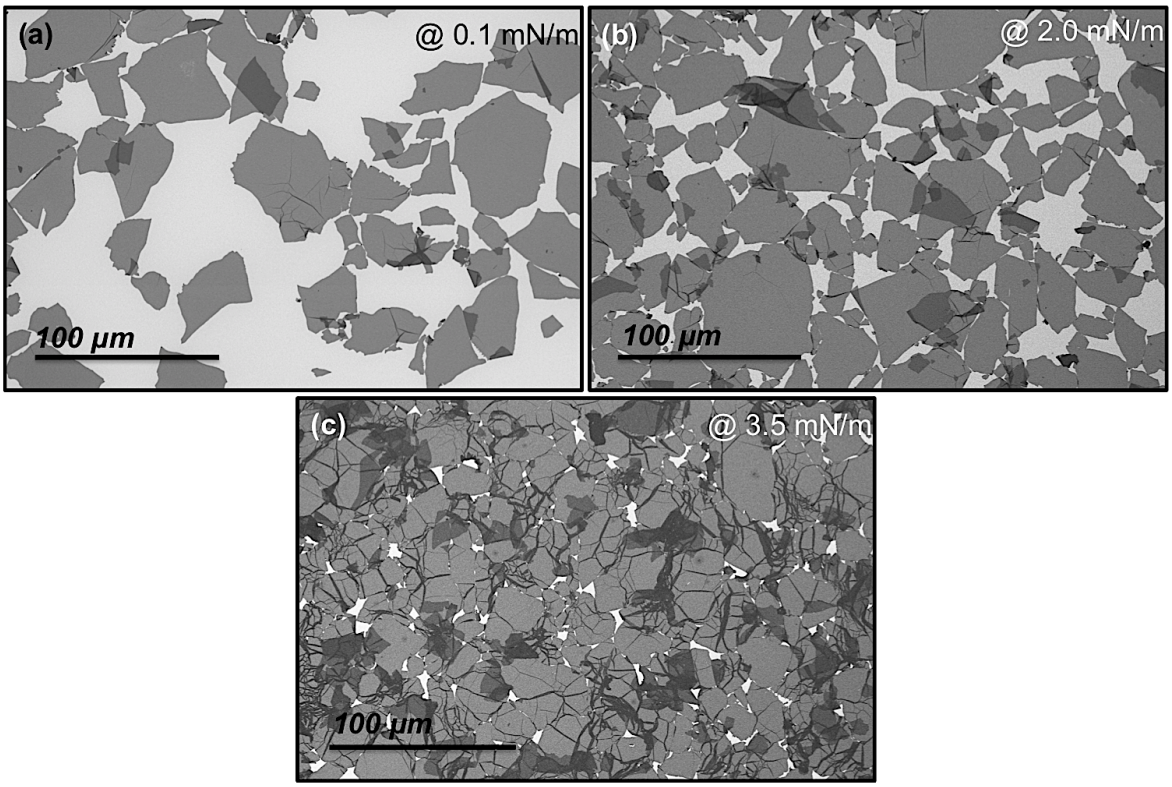

Figure 6. The SEM images collected with 5 ml solution volume of GO on SiO_2/Si at various SPs regions: **(a)** 0.1 mN/m, **(b)** 2.0 mN/m and **(c)** 3.5 mN/m.

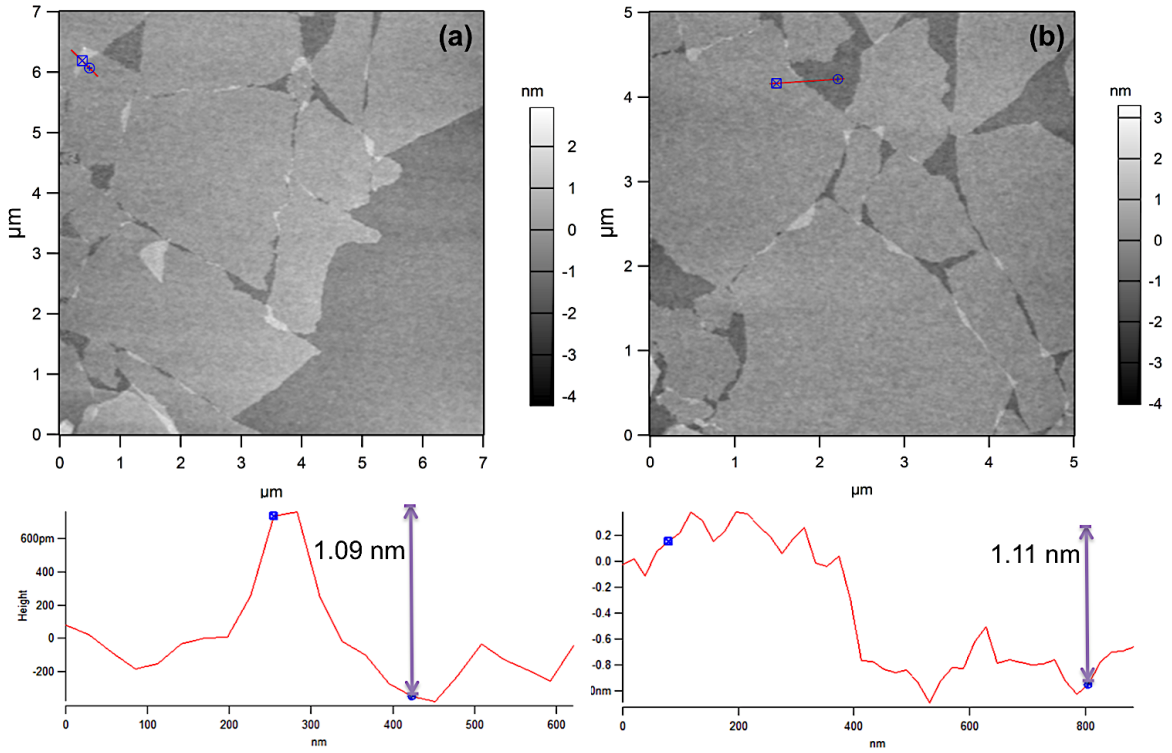

Figure 7. AFM images and corresponding height profile of GO sheets.

indicate the average thickness of GO sheet to be 1.22 ± 0.14 nm (**Figure 7(a and b).** The measurements agree well with other reports [25], confirming their monolayer character.

The LB film was finely lifted on TEM grid from the subphase containing monolayer GO sheets using horizontal dipping technique and TEM images were acquired at low and high magnification as depicted in **Figure 8**. GO sheets appear to be highly transparent with some folded edges, which might have occurred mainly due to the large area of GO sheet (**Figure 8(a and c)**). To affirm the crystalline nature of GO, the selected area electron diffraction (SAED) pattern was performed (**Figure 8(b)**) that is quite similar to the typical six-fold symmetry obtained for graphite oxide [26], which suggests that the obtained GO sheets were not completely amorphous in nature. Importantly, it should be noticed from the SAED pattern of GO that the inner hexagonal spots {1-100} were more intense than the outer hexagonal spots {11-20}, suggesting the presence of monolayer GO-sheets rather than multilayer sheets that agrees very well with the previous reports [27,

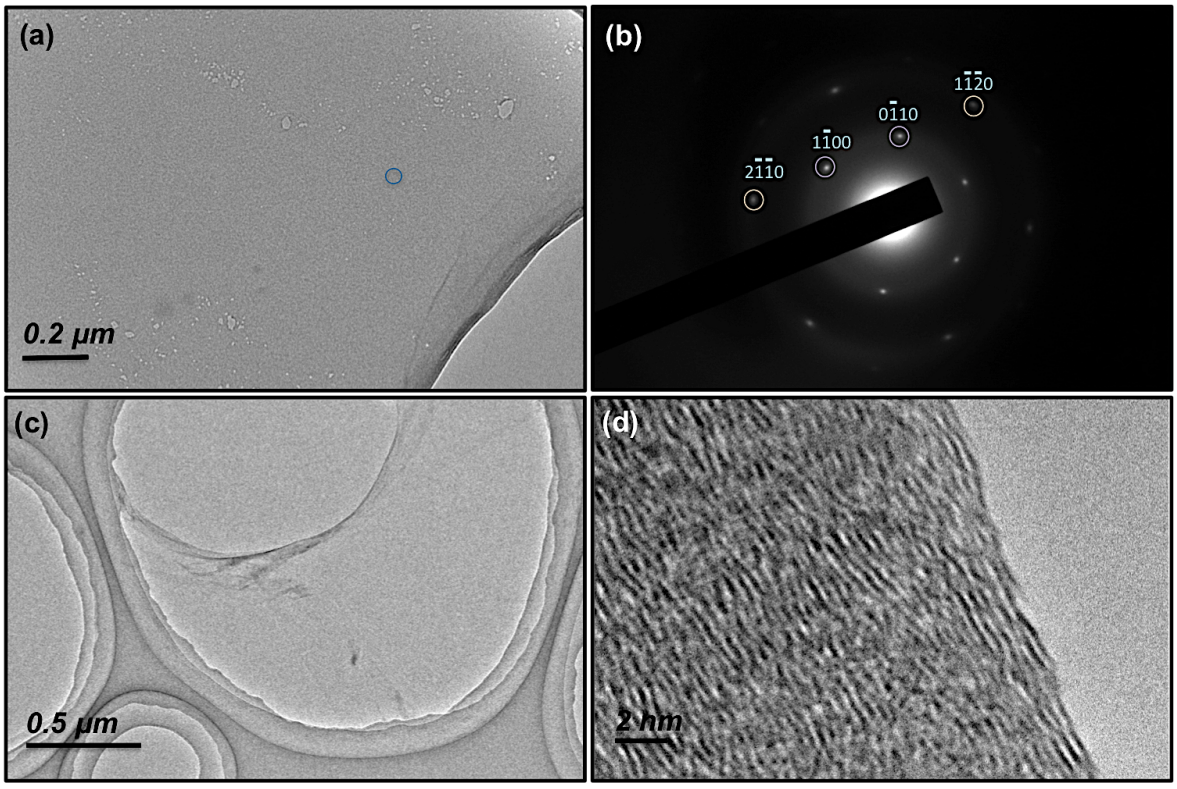

Figure 8. The structural and crystalline analysis of GO sheets. **(a)** TEM image of individually stacked GO-sheet lifted by LB technique, **(b)** SAED pattern performed on spotted area in (a), **(c)** GO at low magnification and **(d)** high magnification image of GO.

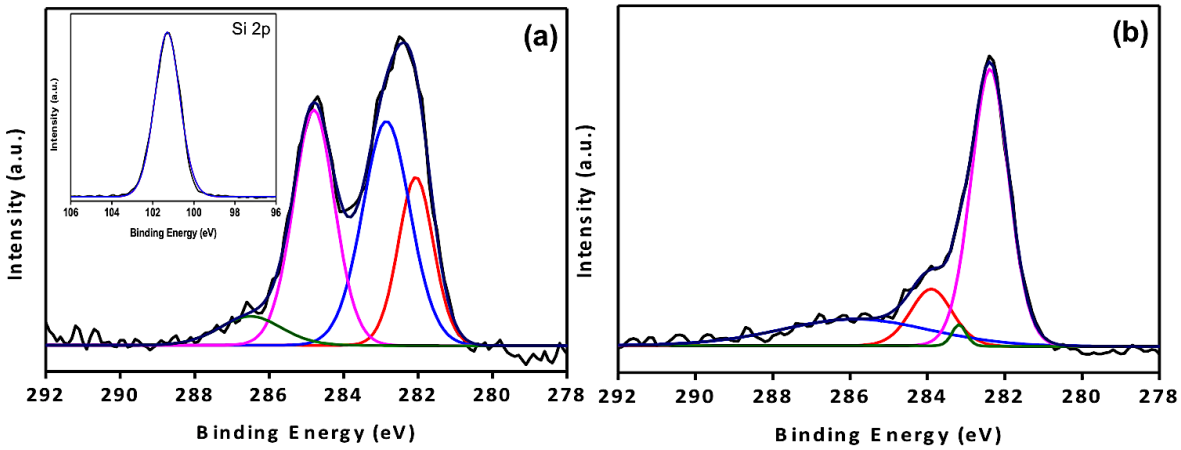

Figure 9. (a) C 1s XPS spectra of GO before annealing, *inset* showing Si 2p XPS spectra of GO on SiO_2/Si, indicating a charge-up shift of 2.1 eV and **(b)** after annealing at 300 °C for 2 hr under N_2 environment.

28] and thus explaining our AFM results. **Figure 8(d)** shows the edge image of monolayer GO at high magnification. TEM images have confirmed the deposition of monolayer GO over large area using LB deposition technique, thus can also effectively be employed as a support film for the study of nanoparticles and macromolecules by TEM as they are highly electron transparent and stable in the electron beam [27].

The XPS analysis was aimed to evaluate the elemental compositions and functionalities present on the GO film and thus help us understand its surface chemistry that greatly affects its optical and electrical properties. **Figure 9** shows the C 1s XPS and the curve fitting spectrum of GO film on SiO_2/Si substrate before and after thermal annealing at 300 °C for 2 hrs under N_2 environment (200 ml/min).

All XPS binding energies were normalized to Si 2p (oxide) peak (**Figure 9(a), inset**) to eliminate build up charging that might have been introduced due to the insulating behavior of SiO_2. At least four components C=C (sp^2) (at ~ 284.2 eV), C−C (sp^3) (at ~ 284.9 eV), C−OH (at ~ 286.9 eV) and C=O (at ~ 288.6 eV) resulting from the carboxylic group, were observed in GO sheets (**Figure 9(a)**) [29, 30]. However, after thermal annealing the peak intensities of C−O and C=O peaks reduced drastically and the peak intensity for C-C bond increased significantly (**Figure 9(b)**), thus proving considerable de-oxygenation and restoration of sp^2 carbon sites that agree well with the previous reports [29].

4.5 Conclusion

We have successfully prepared large area monolayer GO sheets with high reaction yield to control the edge density, evaluate its viability and practicality. Most importantly, we found that the size of the starting material (NG), the oxidation temperature, the washing steps, the solution pH, etc. all highly affects the final size of GO. Various characterization techniques have been employed to understand the properties of as-synthesized GO sheets. Controlled large area films of monolayer GO on SiO_2/Si substrate were obtained using LB technique. We believe that our findings can help create better products for wide range of real-world applications that will be discussed in the upcoming chapters.

References

1. K.S. Novoselov, A.K. Geim, S.V. Morozov, D. Jiang, Y. Zhang, S.V. Dubonos, I.V. Grigorieva, A.A. Firsov. *Science* **2004**, *306*, 666.
2. a) P. Pasanen, M. Voutilainen, M. Helle, X. Song and P. J Hakonen. *Phys. Scr.* **2012,** *T146*, 014025 (10pp); b) H. Shen, L. Zhang, M. Liu, Z Zhang. *Theranostics* **2012,** *2(3)*, 283.
3. a) R.S. Edwards, K.S. Coleman. *Nanoscale* **2013,** *5*, 38; b) J. Liu, Z. Yin, X. Cao, F. Zhao, L. Wang, W. Huang, H Zhang. *Adv. Mater.* **2013** *25*, 233; c) L. Liao, J. Bai, R. Cheng, H. Zhou, L. Liu, Y. Liu, Y. Huang, X. Duan. *Nano Lett.*, **2012,** *12 (6)*,2653.
4. a) T. Kraus, D. Brodoceanu, N P-Perez, A. Fery. *Adv. Funct. Mater.* **2013**, *23*, 4529; b) D. Whang, S. Jin, C. M. Lieber. *Jpn. J. Appl. Phys.* **2004**, 43(7B), 4465; c) J. Huang, R. Fan, S. Connor, P. Yang. *Angew. Chem. Int. Ed.* **2007**, *46*, 2414.
5. a) H. A. Becerril, J. Mao, Z. Liu, R. M. Stoltenberg, Z. Bao, Y. Chen. *ACS Nano* **2008**, *2*, 463; b) X. Wang, L. Zhi, N. Tsao, Z. Tomovic, J. Li, K. Müllen. *Angew. Chem.,* Int. Ed. **2008**, *47 (16)*, 2990.
6. a) D. Li, M. B. Muller, S. Gilje, R. B. Kaner, G. G. Wallace. *Nat. Nanotechnol.* **2008**, *3*, 101; b) Y. Xu, H. Bai, G. Lu, C. Li,; Shi, G. *J. Am. Chem. Soc.* **2008**, *130*, 5856.
7. X. Luan, L. Chen, J. Zhang, G. Qu, J. C. Flake, Y. Wang. *Electrochimica Acta* **2013**, *111*, 216.
8. Y. Zhu, W. Cai,; R. D. Piner, A. Velamakanni, R. S. Ruoff, *Appl. Phys. Lett.* **2009**, *95*, 103104.

9. N. I. Kovtyukhova, P. J. Ollivier, B. R. Martin, T. E. Mallouk, S. A. Chizhik, E. V. Buzaneva, and A. D. Gorchinskiy. *Chem. Mater.* **1999**, *11,* 771.
10. X. Li, G. Zhang, X. Bai, X. Sun, X. Wang, E. Wang, H. Dai, *Nat. Nanotechnol.* **2008**, *3*, 538.
11. L. J. Cote, J. Kim, Z. Zhang, C. Sun, J. Huang. *Soft Matter* **2010**, *6*, 6096.
12. Q. Zheng, B. Zhang, X. Lin, X. Shen, N. Yousefi, Z-D Huang, Z. Li, J-K Kim. ***J. Mater. Chem.*** **2012**, ***22***, 25072.
13. S. Eigler, M. E-Heim, S. Grimm, P. Hofmann, W. Kroener, A. Geworski, C. Dotzer, M. Röckert, J. Xiao, ChPapp, O Lytken, H-P Steinrück, P. Müller, A. Hirsch. *Adv. Mater.* **2013**, *25*, 3583.
14. I. Jung, D. A. Dikin, R. D. Piner, R. S. Ruoff. *Nano Lett.* **2008,** *8,* 4283.
15. L. J. Cote, F. Kim, J. Huang. *J. Am. Chem. Soc.* **2009**, *131*, 1043.
16. X. Lin, J. Jia, N. Yousefi, X. Shen, J-K Kim. *J. Mater. Chem. C* **2013**, *1*, 6869.
17. a) B. J. Clark, T. Frost, M. A. Russell. UV Spectroscopy: Techniques, Instrumentation, Data Handling/UV Spectrometry Group; Chapman & Hall: London, New York; Vol. 4, **1993**; b) S. Raveendran, N. Chauhan, Y. Nakajima, H. Toshiaki, S. Kurosu, Y. Tanizawa, R. Tero, Y. Yoshida, T. Hanajiri, T. Maekawa, P. M. Ajayan, A. Sandhu, D. S. Kumar. *Particle and Particle System Characterization* **2013,** *30 (7)*, 573.
18. a) Z Q-bin, S. Li-fang, Y. Jun-he. *Trans. Nonferrous Met. Soc. China,* **2012**, *22*, 2504; b) J. Zhao, S. Pei, W. Ren, L. Gao, H-M Cheng. *ACS Nano* **2010**, *4(9)*, 5245.
19. a) N. B. Colthup, L. H. Daly, S. E. Wiberley. *Introduction to Infrared and Raman Spectroscopy*, 3rd ed., Academic Press: London; **1990**; b) A. Mathkar, D. Tozier, P. Cox, P. Ong, C. Galande, K. Balakrishnan, A. L. M. Reddy, P. M. Ajayan. *J. Phys. Chem. Lett.* **2012**, *3*, 986.
20. A. C. Ferrari, D. M. Basko. *Nature Nanotechnol.* **2013**, *8(4),* 235.
21. a) S. Stankovich, D. A. Dikin, R. D. Piner, K. A. Kohlhaas, A. Kleinhammes, Y. Jia, Y. Wu, R. S. Ruoff, S. T. Nguyen. *Carbon*, **2007**, *45*, 1558; b) C-Y Su, Y. Xu, W. Zhang, J. Zhao, X. Tang, C-H Tsai, L-J Li. *Chem. Mater.* **2009**, *21*, 5674; c) S. Stankovich, D. A. Dikin, R. D. Piner, K. A. Kohlhaas, A. Kleinhammes, Y. Jia, Y. Wu, R. S. Ruoff, S. T. Nguyen. *Carbon* **2007**, *45*, 1558.
22. J. R. Lomeda, C. D. Doyle, D. V. Kosynkin, W-F Hwang, J. M. Tour. *J Am Chem Soc* **2008**, *130*, 16201.

23. J. Lim, K. Choi, J. R. Rani, J-S Kim, C. Lee, J. H. Kim, S. C. Jun. *J. Appl. Phys.* **2013**, *113*, 183502.
24. J. Kim, L. J. Cote, F. Kim, W. Yuan, K. R. Shull, J. X. Huang. *J. Am. Chem. Soc.* **2010**, *132*, 8180.
25. a) Y. Si, E. T. Samulski. *Nano Lett.* **2008**, *8 (6)*, 1679; b) B. Jia, L. Zou. *Carbon* **2012**, *50*, 2315.
26. H-K Jeong, Y. P. Lee, R. J. W. E. Lahaye, M-H Park, K. H. An, I. J. Kim, C.-W. Yang, C. Y. Park, R. S. Ruoff, Y. H. Le*e. J. Am. Chem. Soc.* **2008**, *130 (4)*, 1362.
27. N.R. Wilson, P.A. Pandey, R. Beanland, R.J. Young, I.A. Kinloch, L. Gong, Z. Lui, K. Suenaga, J.P. Rourke, S.J. York, J. Sloan. *ACS Nano* **2009**, *3(9)*, 2547.
28. S. R. Dhakate, N. Chauhan, S. Sharma, J. Tawale, S. Singh, P. D. Sahare, R. B. Mathur. C*arbon* **2011**, *49*, 1946.
29. K. Haubner, J. Morawski, P. Olk, L. M. Eng, C. Ziegler, B. Adolphi, E. Jaehne. *Chemphyschem.* **2010**, *11(10)*, 2131.
30. G. Singh, A. Choudhary, D. Haranath, A. G. Joshi, N. Singh, S. Singh, R. Pasricha. *Carbon* **2012**, *50(2)*, 385.